8-29-2018

Techniques for Improved Space Object Detection Performance from Ground-Based Telescope Systems Using Long and Short Exposure Images

David J. Becker

Techniques for Improved Space Object Detection Performance from Ground-Based Telescope Systems Using Long and Short Exposure Images

DISSERTATION

David J. Becker, Major, USAF

AFIT-ENG-DS-18-S-006

DEPARTMENT OF THE AIR FORCE
AIR UNIVERSITY

AIR FORCE INSTITUTE OF TECHNOLOGY

Wright-Patterson Air Force Base, Ohio

AFIT-ENG-DS-18-S-006

TECHNIQUES FOR IMPROVED SPACE OBJECT DETECTION PERFORMANCE FROM GROUND-BASED TELESCOPE SYSTEMS USING LONG AND SHORT EXPOSURE IMAGES

DISSERTATION

Presented to the Faculty

Graduate School of Engineering and Management

Air Force Institute of Technology

Air University

Air Education and Training Command

in Partial Fulfillment of the Requirements for the

Degree of Doctor of Philosophy

David J. Becker, B.S.E.E., M.S.E.E.

Major, USAF

September 2018

AFIT-ENG-DS-18-S-006

TECHNIQUES FOR IMPROVED SPACE OBJECT DETECTION PERFORMANCE FROM GROUND-BASED TELESCOPE SYSTEMS USING LONG AND SHORT EXPOSURE IMAGES

DISSERTATION

David J. Becker, B.S.E.E., M.S.E.E.
Major, USAF

Committee Membership:

Stephen C. Cain, PhD
Chairman

Maj. Scott Pierce, PhD
Member

Christine Schubert Kabban, PhD
Member

ADEDEJI B. BADIRU, PhD
Dean, Graduate School of Engineering and Management

Abstract

Space object detection is of great importance in the highly dependent yet competitive and congested space domain. Detection algorithms employed play a crucial role in fulfilling the detection component in the space situational awareness mission to detect, track, characterize and catalog unknown space objects. Many current space detection algorithms use a matched filter or a spatial correlator on long exposure data to make a detection decision at a single pixel point of a spatial image based on the assumption that the data follows a Gaussian distribution. This research focuses on improving current space object detection algorithms and developing new algorithms that provide a greater detection performance, specifically with dim and small objects which are inherently difficult to detect. With a greater detection rate, a great number of unknown objects will be detected, tracked and cataloged to deliver safer space operations. Three novel approaches to object detection using long and short exposure images obtained from ground-based telescopes are examined in this dissertation.

Two of the approaches examined in this dissertation involved detection algorithms designed from the probability distribution of the real component of the Fourier transform of the intensity of the object. Models for the object and its statistics were calculated to build a likelihood ratio test. Additionally, spatial frequency correlation was examined to build a joint probability distribution function likelihood ratio test. Both the Fourier point detector and Fourier correlation algorithm demonstrated a significant increase in the probability of detection over their commonly used spatial counterpart algorithms.

Long exposure imaging is critical to detection performance in these algorithms, however if imaging under daylight conditions it becomes necessary to create a long

exposure image as the sum of many short exposure images. The third approach in this research explores the potential to increase detection capabilities of small and dim space objects in a stack of short exposure images dominated with a bright background. The algorithm proposed in this paper improves the traditional stack and average method of forming a long exposure image by selectively removing short exposure frames of data that do not positively contribute to the overall signal to noise ratio of the averaged image. The performance of the algorithm is compared to a traditional matched filter and lucky imaging algorithm using data generated in MATLAB as well as experimentally collected data. The results are illustrated on a receiver operating characteristic curve to highlight the significant increase in probability of detection associated with the frame selection algorithm.

The long exposure algorithms developed in this research obtained a 40% increase in detection probability over a point detector and a 11-23% increase over spatial correlator at a false alarm rate of 10^{-9}. Using frame selection on short exposure daylight images, the developed algorithm achieved a 10-25% increase in detection probability over a traditional average and correlate method.

Table of Contents

Page

List of Figures

List of Tables

List of Acronyms

AFIT Air Force Institute of Technology

AMOS Air Force Maui Optical Station

BHT binary hypothesis test

CCD charge-coupled device

DoD Department of Defense

FOV field of view

GEO geostationary Earth orbit

JSpOC Joint Space Operations Center

LINEAR Lincoln Near Earth Asteroid Research

LRT Likelihood Ratio Test

MHT multi-hypothesis test

MIT Massachusetts Institute of Technology

NASA National Aeronautics and Space Administration

NEA near earth asteroids

NEO Near Earth Object

OTF optical transfer function

P_D probability of detection

P_{FA} probability of false alarm

PDF probability density function

PSF point spread function

SNR signal-to-noise ratio

SSA Space Situational Awareness

SSN Space Surveillance Network

SST Space Surveillance Telescope

TECHNIQUES FOR IMPROVED SPACE OBJECT DETECTION PERFORMANCE FROM GROUND-BASED TELESCOPE SYSTEMS USING LONG AND SHORT EXPOSURE IMAGES

I. Introduction

1.1 Motivation

Safe and dependable operations in the space domain are vital to the national security interests of the United States (U.S.). According to the 2011 U.S. National Security Space Strategy, "space is vital to U.S. national security and our ability to understand emerging threats, project power globally, conduct operations, support diplomatic efforts, and enable global economic viability" [1]. In order to preserve continued space operations, the 2010 U.S. National Space Policy called out the need to fund and develop technologies to "detect, identify, and attribute actions in space that are contrary to responsible use and the long-term sustainability of the space environment" [2]. Additionally, the National Space Policy stated the need to "pursue capabilities to detect, track, catalog, and characterize near-Earth objects to reduce the risk of harm to humans from an unexpected impact on our planet and to identify potentially resource-rich planetary objects".

To continue safe and reliable space operations, the ability to detect and track space objects is of great importance to the Department of Defense (DoD), United States Air Force (USAF), National Aeronautics and Space Administration (NASA) as well as other space organizations around the world. Through the NASA Authorization Act of 2005, the U.S. Congress mandated NASA to coordinate with the DoD and other

organizations to catalog by the year 2020, 90 percent of all asteroids and comets larger than 140 m that are within close trajectory of Earth [3]. NASA predicts that there are nearly 1,000 near earth asteroids (NEA) larger than 1 km and approximately 15,000 larger than 140 m. Additionally, there are approximately 500,000 pieces of debris that are larger than 1 cm and that the number of objects smaller than 1 cm exceeds 100 million [4, 5]. The latest data on the number of NEA cataloged from the NASA Near Earth Object (NEO) program office is shown in Figure 1.

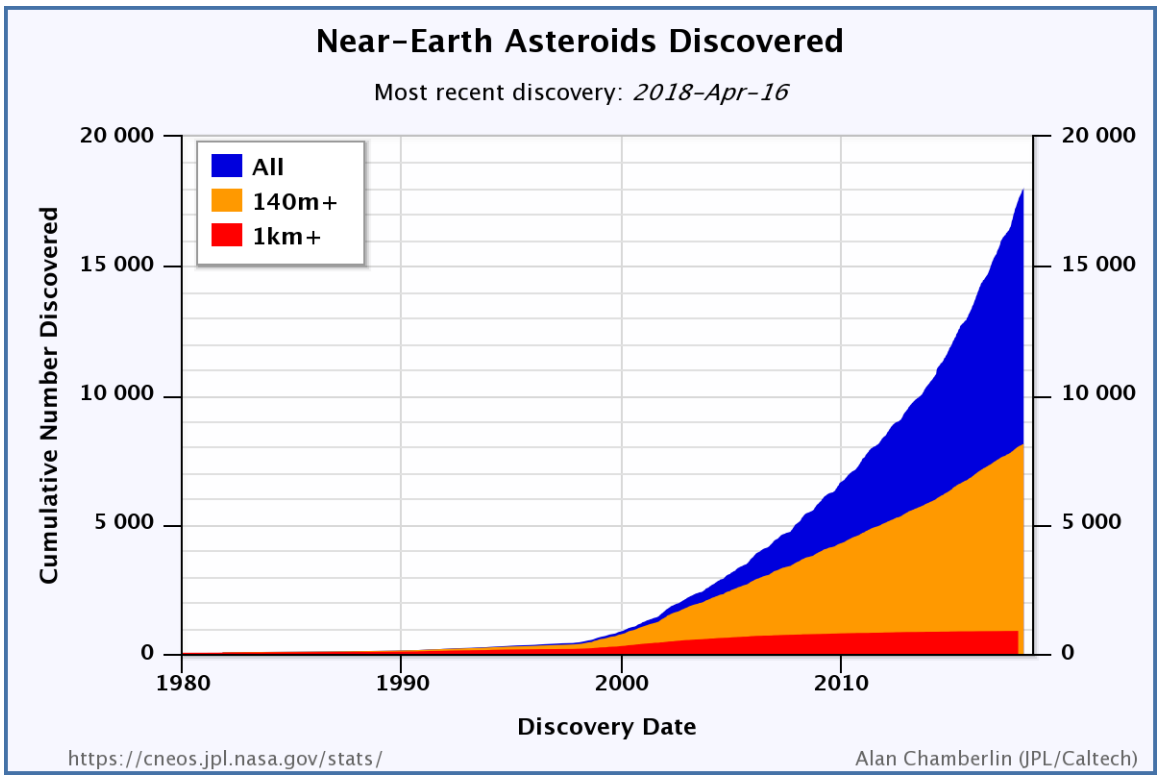

Figure 1. Number of near Earth asteroids detected and cataloged each year by NASA [4].

Within the DoD, the ability to detect and track space objects such as nanosatellites and space debris is of particular importance due to the great risk they pose to critical space assets, especially in the geostationary Earth orbit (GEO) [6]. The Joint Space Operations Center (JSpOC) currently manages the process of tracking nearly 20,000 known man-made objects in space. Many of these objects were detected by assets

within the Space Surveillance Network (SSN) and a track was developed using follow-up taskings [7]. The composition of these objects and the increase in their prevalence is shown in Figure 2. At the end of 2017, there were 1,459 operational satellites being tracked by JSpOC [8]. This represented a 47% increase over the last 5 years. Many commercial companies are proposing to greatly increase their number of operating satellites. Making headlines recently include Boeing with a proposed 1,400-3,000 satellites, SpaceX with up to 7,500 satellites and OneWeb with 2,000 satellites [9]. There is a clear trend towards greater commercial use of satellites in the future. As the space domain becomes more populated, there will likely be malfunctions, collisions and breakup that result in man-made debris that will further populate the region and raise the risk for critical damage to the operations of space assets.

The SSN is composed of a worldwide network of 30 civilian and military sensors dedicated to detect and provide tracking information on known and newly discovered space objects to the JSpOC. The sensor sites within the SSN include phased-array and conventional radar systems along with a network of ground-based electro-optic telescopes. The Air Force Space Command (AFSPACECOM) manages the Ground-Based Electro-Optical Deep Space Surveillance (GEODSS) sites which include the Space Surveillance Telescope (SST) currently located at White Sands Missile Range in Socorro, New Mexico along with the Air Force Maui Optical Station (AMOS) in Maui, Hawaii and a site at Diego Garcia in the Indian Ocean [10]. It is the mission of these assets to gather and process data to improve the Space Situational Awareness (SSA) mission.

1.2 Research Goals & Objectives

The underlying goal of this research is to improve the ability to detect small or dim space objects using traditional images obtained from existing ground-based tele-

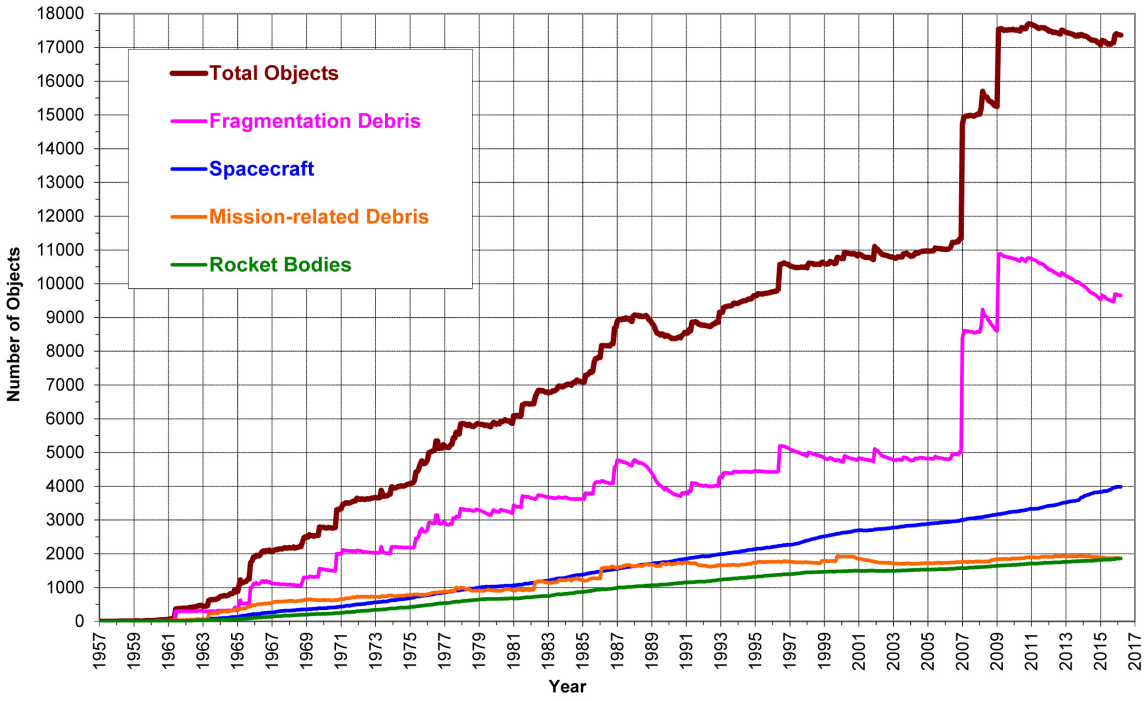

Figure 2. Number of objects tracked in Earth's orbit by object type [11].

scopes. The detection of both asteroid and man-made objects or debris represents a similar challenge to those looking to detect, track and catalog unknown space objects. Due to their small size when viewed from a ground-based telescope, both objects are essentially an unresolvable point source on the image captured by the charge-coupled device (CCD). Additionally, when looking for smaller asteroids or objects, the intensity received by the telescope from the object is likely to be low and could approach the level of background noise. As will be described in Chapter II, current detection algorithms employed by ground-based telescopes tasked to the SSA mission are based on a matched filter approach of the spatial image captured by the CCD of the optical system. The research in this dissertation seeks to improve the detection capabilities by addressing the following three research questions.

1. Will converting a spatial image to the Fourier domain improve the detection

performance of a point source detector?

2. Is there correlation between spatial frequencies when an object is present? If so, can a covariance matrix between spatial frequencies in a Fourier domain image be used to improve object detection?

3. Under daylight imaging where short exposure images are necessary, will frame selection increase the ability of detecting objects over simply combining multiple frames?

Research question one and two examine detection algorithms in the Fourier domain as opposed to a traditional spatial domain image. Research question three addresses the utility in building a frame selection approach utilizing short exposure spatial images to improve detection.

1.3 Assumptions and Limitations

The following assumptions are made to scope this research.

- Any unknown space object within the scene is unresolvable and can be considered a point source to the imaging system. This does not limit intensity from the object to a single pixel since blurring due to the atmosphere and optics will likely spread the intensity across multiple pixels.

- Background noise in the image follows a Poisson distribution and is known or can be measured from the image.

- Only a single frame of long exposure data or multiple short exposure images taken in the same time frame as a single long exposure image are used to make the decision on an object being present or not. There are algorithms that utilize

multiple long exposure frames of data to reduce the number of false alarms, but that technique is not investigated in this research.

- Under daylight imaging, the camera's CCD pixel wells are limited in depth and necessitate short exposure imaging to avoid saturation.

1.4 Document Outline

This dissertation is organized into six chapters that contain the necessary background information to achieve the goal of this research and address the questions in Section 1.2. Background information, relevant publications and current object detection techniques are contained in Chapter 2. This chapter includes a discussion on atmospheric turbulence, noise sources and optical models. All are needed to understand the task, develop statistical models for the data and build detection algorithms.

Chapter 3 builds a Fourier point detection algorithm based on the Fourier domain representation of the spatial image obtained from a ground-based optical system. The algorithm utilizes a statistical model of the data to build a Likelihood Ratio Test (LRT) which is then compared to two traditional space detection algorithms, a spatial matched filter or correlator and a spatial point detector.

Chapter 4 develops a Likelihood Ratio Test (LRT) based on research that revealed there is correlation between spatial frequencies of the real component of the Fourier transformed background removed spatial image when an object is present. Utilizing a conditional joint Gaussian probability density function (PDF) along with a statistical model for the data and a theoretically derived covariance matrix, the LRT can be used to detect dim space objects in the Fourier domain. The Fourier correlation algorithm developed in this chapter is compared to a spatial correlation algorithm utilizing simulated data on a Semi-log Receiver Operating Characteristic (LROC) curve to highlight detection performance differences between the two algorithms.

Chapter 5 explores detection utilizing short exposure images obtained under daylight imaging conditions. Current detection techniques are focused on building a long exposure image by combining a set of short exposure images and in some cases, registering and then combining these frames. The research in this chapter develops a detection algorithm that selects the best short exposure frames based on a correlation technique that does not require registering any frames. The performance of the algorithm is compared to a spatial correlator and a short exposure imaging technique called "lucky imaging" using both simulated and experimentally collected data on a Semi-log Receiver Operating Characteristic (LROC) curve.

Chapter 6 is a conclusion to this dissertation that summarizes each of the research efforts, the impact and relevancy of this research, and future follow-on work that can be investigated. The conclusion also cites publications that resulted from this research.

II. Background & Literature Review

2.1 Chapter Overview

This chapter outlines background information related to the research completed in this dissertation. First, this chapter provides a space object detection overview and a discussion on the relevance of improving object detection algorithms. This section includes a review of current and historical object detection techniques utilized by astronomers and those within the SSA community. The second half of this chapter includes a review of the imaging system, atmospheric turbulence and the effects it has on the imaging system and the detection process along with additional noise sources in the image that effect the probability of detection and false alarms.

2.2 Space Object Detection Overview

Space objects can be broken down into two major classes, defined as either naturally occurring objects or man-made objects. These two distinct classes of objects clearly have different physical properties such as shape, size and composition. Each of these characteristics will greatly affect the ability to image, and thus detect, the object. An object with a surface material of higher reflectivity will appear brighter. Additionally, the orientation of the object relative to the sun and the ground position of the telescope will impact the imaging and detection performance. The assumption is made and usually holds true for SSA detection systems, that all objects in the field of view (FOV) would appear optically similar to an observer using a ground-based telescope designed for detecting unknown objects. A detection system with a wide FOV is utilized to image large sections of the sky. The FOV is on the order of 3-6 degrees of the sky per image [12, 13]. This is contrary to an imaging system designed to obtain a high resolution image of a known object which has an extremely narrow

FOV. Due to the similarity of detecting unknown objects, this dissertation has possible impacts in the academic, scientific and defense focused space object detection and astronomical communities.

Asteroids and comets are naturally occurring NEOs for which astronomers have for centuries searched the skies for. The first detection of an asteroid is credited to Giuseppe Piazzi who in 1801 discovered Ceres [14]. This relatively large asteroid, with a radius of 476 km, resides in what is now known as the asteroid belt between Mars and Jupiter. These first object detections were discovered using early observatories along with the human eye to detect new or missing objects between temporally spaced observations. Astronomers have continued to search for planets, asteroids and comets, and more recently, objects that pose an existential threat to human life on Earth. Recent advancements in optics, sensor hardware such as low-noise and curved CCDs, along with improvements to detection algorithms fueled by cheaper and move complex computing power have led to orders of magnitude improvement in the ability to detect NEOs.

The mission to discover smaller and less frequently orbiting natural objects near Earth has been assigned to NASA by the U.S. Congress through the NASA Authorization Act of 2005 [3]. The U.S. Congress mandated NASA to coordinate with the DoD and other organizations to catalog by the year 2020, 90 percent of all asteroids and comets larger than 140 m that are within close trajectory of Earth. NASA predicts that there are nearly 1,000 NEA larger than 1 km and approximately 15,000 larger than 140 m. The NASA NEO program office predicts that over 90% of asteroids larger than 1 km have been discovered and is focused on detecting those objects between 140 m and 1 km. Nearly all of the NEO discoveries have occurred within the last 20 years when this mandate was put in place. The latest data on the number of NEAs cataloged by NASA's NEO program office was shown in Chapter 1, Figure

1. A breakout of the size of the asteroids is also given in Figure 3. The number of larger objects discovered has remained relatively flat over the last 20 years since these objects are much easier to observe, were among the first to be detected and tracked and NASA predicts most have already been discovered. However, due to the vastness of space, new objects larger than 1 km are located every year. In many cases, new objects are not detected until they are astronomically very close to Earth. Recent examples include the near Earth asteroids, 2018 CB which was detected just days before passing near Earth and Asteroid 2018 GE3 which was detected hours before. Both were first detected by NASA's Catalina Sky Survey [15, 16].

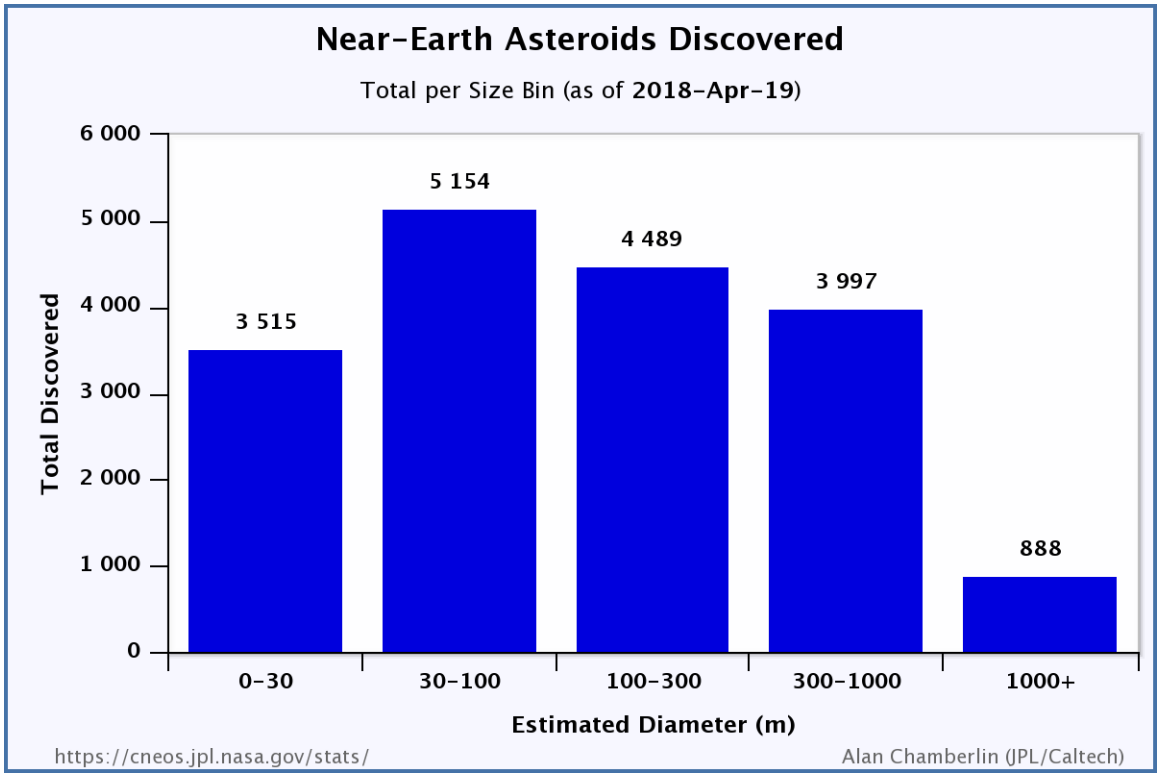

Figure 3. Number of near Earth objects detected and cataloged each year by size of object [4].

Aside from naturally occurring space objects, man-made objects account for the vast majority of NEOs that pose a risk to assets in space. Man-made debris in space is the result of decades of human space exploration and activities. These objects include

dysfunctional or abandoned satellites, spent space launch vehicles, mission related debris and debris created from a handful of documented explosions and collisions of space objects [6]. Little thought was given to limiting or accounting for space debris during early space exploration and utilization. As the number of assets in space grew, the need to track space debris and implement methods to limit creating new debris became apparent. The density of man-made space debris in the heavily space asset populated GEO region around 35,785 km is illustrated in Figure 4. The threat is not limited to physical collision between satellites and objects but also damage from small piece of debris to critical components of the satellite such as the solar panels which could render a satellite dysfunctional or uncontrollable.

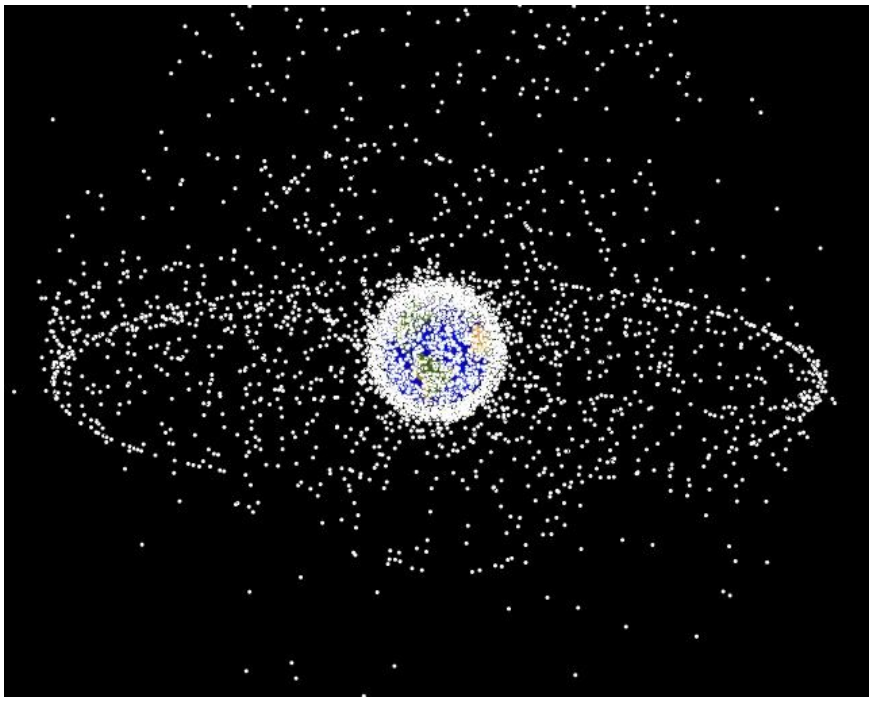

Figure 4. Debris population in the geosynchronous region [5].

Utilizing the SSN sensors, the JSpOC currently tracks approximately 20,000 man-made objects in orbit around Earth that are the size of a baseball or larger [7]. They are tasked with maintaining the space catalog used by nearly all space operators

to track objects and provide collision avoidance guidance in the case of a potential impact. The first known collision of man-made space objects occurred in 1991 between two retired Russian satellites, Cosmos 1934 and Cosmos 926 [17]. Nearly one-third of the cataloged orbital debris in the GEO region is a result of the intentional destruction of the Fengyun-1C weather satellite by China in 2007 and the accidental collision of American and Russian communication satellites in 2009 [5]. NASA estimated that approximately 35,000 pieces of debris larger than 1 cm were created as a result of the destruction of Fengyun-1C. It is likely that the debris created by this event impacted and destroyed a Russian satellite in 2013 [18]. NASA predicts there are approximately 500,000 pieces of debris that are larger than 1 cm and that the number smaller than 1 cm exceeds 100 million [4, 5]. The number of objects currently tracked by JSpOC was shown in Chapter 1, Figure 2. If the estimates from NASA are correct then there are many unaccounted for and potentially hazardous objects in Earth's orbit.

The pursuit to catalog a greater number of space objects involves multiple areas of research. Imaging, processing, detecting, tracking and characterizing are all components needed to successfully catalog an object. The work in this dissertation focuses on processing images and detecting space objects. The processing and detection of space objects from images obtained from ground-based optical telescopes will allow SSN sensors to conduct follow-up observations to establish a track, resolve the object and characterize it for addition to the space catalog.

Daylight Imaging.

One of the factors seriously limiting space object detection assets is the inadequate telescope time available for the detection mission. Factors such as hardware upgrades, weather and maintenance all affect the amount of time available for astronomers and operators to collect data. Possibly, the greatest hindrance is the amount of prime

night sky available when conditions are favorable. Conventional space object imaging operations is limited to only dark sky imaging during twilight and at night. This is not only due to the brighter background associated with daylight conditions but typically the atmospheric turbulence is significantly greater and less constant during daylight [19, 20]. Limitations in the CCD sensors physically limit the number of photons that can be collected before saturation is reached. This prohibits typical long exposure imaging, limiting sensor integration time down to the short exposure time frame of much less than 100 milliseconds [24].

One of the benefits of being able to image under daylight conditions is the additional operating time. Under traditional night imaging, an object in a near Earth orbit is only going to be detectable under terminator conditions[20]. Terminator describes the short time frame when an object is illuminated by the sun while it is dark at the ground telescope site. Terminator conditions are limited to several hours after sunset and several hours before sunrise. The ability to image and detect objects under daylight imaging conditions would greatly increase the number of hours a telescope could maintain operations.

Imaging during twilight and daylight conditions is possible with smaller aperture telescopes, but the detection algorithms are not optimized for high background, low signal-to-noise ratio (SNR) data. Currently, daylight imaging is mostly limited to high resolution speckle imaging on smaller diameter telescopes. This technique captures hundreds of short exposure images, averages them together and performs a deconvolution algorithm to improve the resolution [21, 22]. These daylight imaging methods are utilized for higher resolution space imaging and not detection as they are utilized on telescopes with an extremely limited FOV on a known object.

2.3 Detection Algorithms & Techniques

Established in 1984 by the University of Arizona, Spacewatch was the first program dedicated to improving the detection, tracking and cataloging of space objects. Spacewatch has been a scientific success to the astronomical community as it was the first to use a CCD to actively scan and survey the sky in search of unknown space objects. Prior to this program, astronomers and those working in the space community were using photographic plates to image and detect objects. The use of CCDs led the program to develop the first software algorithms designed to improve space object detection in 1990 [23]. Since then, CCDs and image processing techniques have greatly improved the number of smaller and fainter space objects detected, tracked and cataloged due to significant advances in computing power, memory and storage. These advances have resulted in further research programs to develop advanced algorithms to detect faint space objects. The latest information from NASA, displayed in Figure 5, shows the number of NEA detected each year and the sensor platform that first detected the object.

The detection method utilized by each platform is tailored to take advantage of the unique capabilities of the sensor. Typically, space object detection algorithms utilize single and multiple spatial images obtained from ground-based telescopes. The different types of techniques can be broken down as shown in Figure 6. Each are broken down by short or long exposure imaging. The most common detectors currently used with the SSA community are described in this section.

The assumptions taken in the research presented in this dissertation were given in Section 1.3. These assumptions are further explained below.

- Space objects imaged by the optical system are unresolvable point sources to the optical system. This implies that no matter the object being imaged, the system cannot distinguish a satellite from an asteroid or debris. It is the responsibility

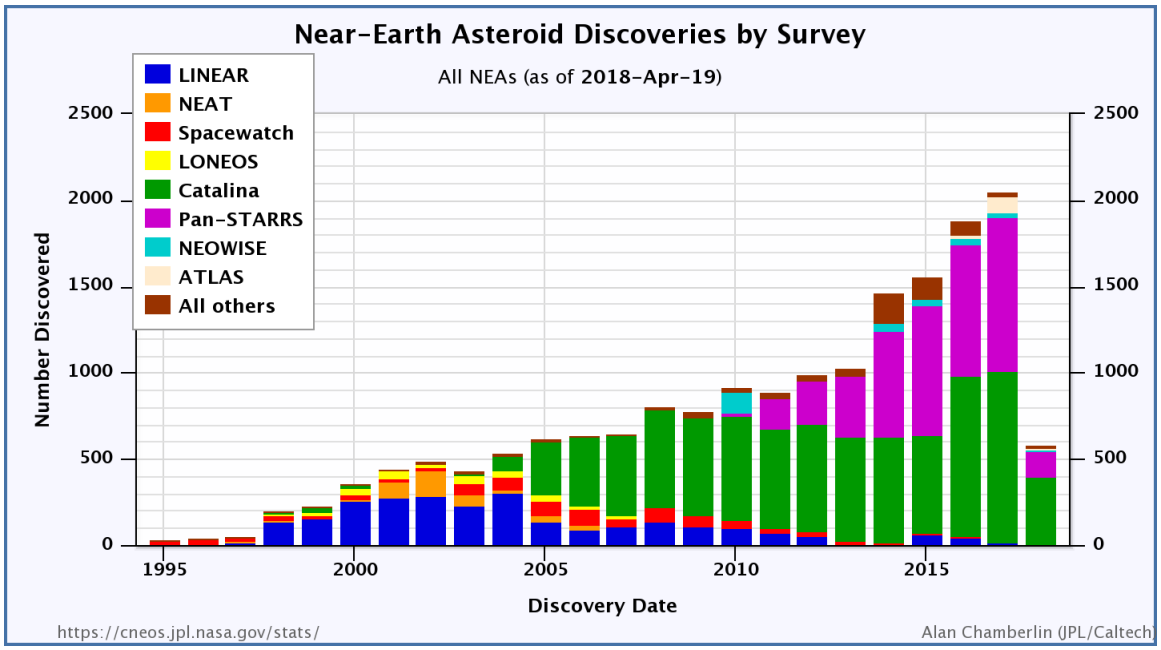

Figure 5. Number of detected near earth asteroids by survey instrument as of 19 Apr 2018 [4].

of dedicated sensors to conduct further observations to characterize a detection.

- Background noise is the result of outside stray light rays entering the optical system and captured in the image. Photons follow a Poisson distribution and the average arrival rate can be measured and is considered a known value.

- A detection decision is made based on the data that can be captured in the time from of a single long exposure frame of data. Many of the SSN platforms use multiple frames in their processing chain, however they start with being able to detect on a single frame and use the multiple frames of follow-up data to confirm or reject a detection. This dissertation is focused on improving the ability to detect a dim space object from a single frame of long exposure data so that detection can be passed on for further multi-frame analysis techniques and further sensor observations. The frame selection research in Chapter 5 utilizes multiple frames of short exposure data which are combined to create a single

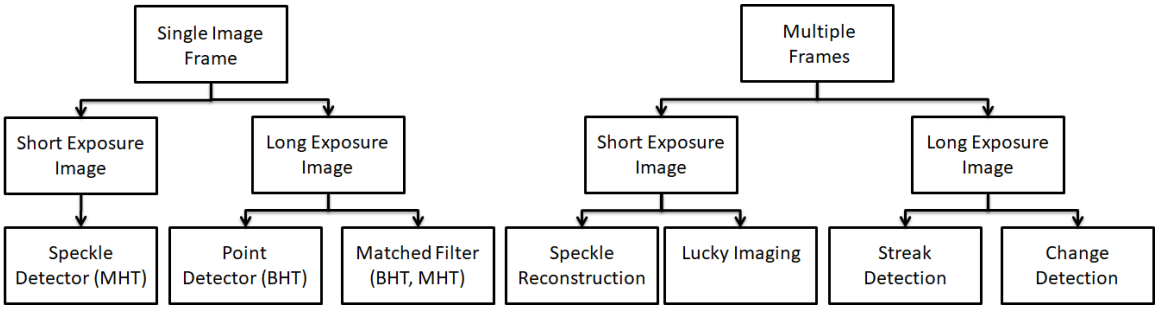

Figure 6. Generalized space object detection techniques depending on number of frames captured and integration times.

long exposure frame of data.

Data is collected using long exposure data in Chapters 3 and 4. This is defined as greater than 100 ms by Goodman [24]. The frame selection research in Chapter 5 is based on short exposure data with an integration time between 10-25 ms. The short integration time is needed due to the high background conditions present in daylight imaging. The integration time in both scenarios is not sufficiently long enough such that the object will create streaks, and thus the algorithms are optimized for point source detection.

- A CCD is made up of thousands of independent "buckets" that count the number of photons that arrive. There is a physical limit to the number of photons that can be counted during each integration cycle that produces an image. Any count over that upper truncated limit results in saturation. To avoid saturation, shorter integration times are needed when imaging a bright target or imaging during a bright background.

With long exposure images, there are two common detection methods discussed in literature and utilized by the various optical telescopes within the SSN, a point detector and a matched filter or correlator. Each of these are techniques are further described in Section 2.3 and Section 2.3. Both detection methods typically starts with

preprocessing of the data to measure background, sometimes perform registration, and potentially remove known objects using a celestial map or similar technique. Due to the large size of a typical image taken, the data is windowed down to a smaller N x N pixel subset of the larger image. For example, the SST data is 6144 x 4096 pixels but processed in windows as small as 15 x 15 [25, 26]. Windowing of the data allows for detection within a much smaller subset of a wide field image limiting interference from other optical sources. The windowing of the larger image decreases the number of pixels in the image being processed which significantly reduces computation time while also decreasing the likelihood that another object is in the image that must be removed prior to processing.

Likelihood Ratio Test (LRT).

The foundation of each space object detection algorithm examined in this dissertation is the use of a LRT to make a decision as to whether an unknown object is present or not in the data [26, 27, 25]. The LRT is used to build a binary mask which indicates pixels where an object is detected. This process was explained by the developers of the SST and Lincoln Near Earth Asteroid Research (LINEAR) algorithm identified in Figure 7 [6].

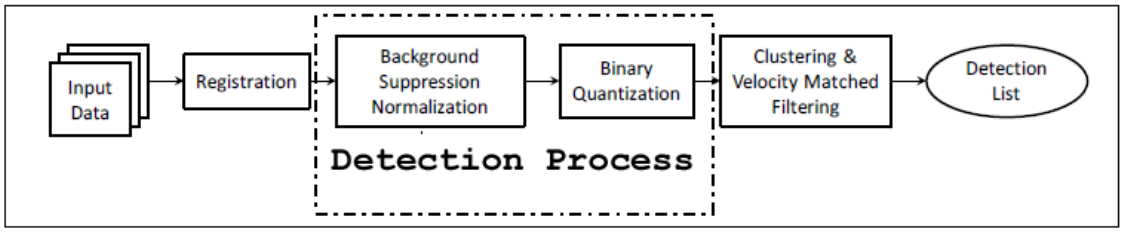

Figure 7. Linear & SST system detection block diagram [25].

Using an equal cost, equal prior model, a generic LRT, Λ, is defined as a ratio of joint conditional probabilities on the received data, $d(x, y)$, given each hypothesis,

H_1 and H_0 [28].

$$\Lambda = \frac{P\big(d(x-x_0, y-y_0)\big)\forall(x,y) \in [1,N]|H_1}{P\big(d(x-x_0, y-y_0)\big)\forall(x,y) \in [1,N]|H_0} \underset{H_0}{\overset{H_1}{\gtrless}} 1. \tag{2.1}$$

Where x and y are the integer pixel coordinates, x_0 and y_0 are the pixel point being tested, and N is the number of pixels in each dimension of the windowed image. The two joint probabilities of the data in the LRT are conditioned on the H_1 hypothesis, that the data contains an object at that specific pixel coordinate, and H_0, that an object is not present at the pixel coordinate x_0, y_0. If the ratio of the conditional probabilities in Equation (2.1) is greater than 1 then the H_1 hypothesis is concluded and triggers an object detection flag. Conversely, a ratio less than 1 makes the determination that an object is not present at the tested pixel coordinate.

Space object detection techniques have historically used a LRT along with a binary hypothesis test (BHT). In a BHT approach, there are only two possible outcomes, either an object is present or not present at a given pixel. Recent research at the Air Force Institute of Technology (AFIT) by Zingarelli and Hardy has shown that a multi-hypothesis test (MHT) approach can significantly increase performance under certain SSA detection scenarios [25, 26]. Their research into the MHT approach examined not only whether an object is in the pixel, but continued research into the effects of sub-pixel shifts in the point spread function (PSF) on detection performance [29]. They found greater detection performance over a BHT when multiple point spread function (PSF) locations or hypotheses are tested within a single pixel.

The underlying key to the success of any LRT is in the ability to distinguish between the probability density function (PDF)s under each hypothesis based on the data. An example of two Gaussian PDFs with varying means and variances are illustrated in Figure 8, as the separation between the two PDFs gets further, it is expected that the detection algorithm will more often correctly determine which

hypothesis the data follows. The performance of different LRT algorithms are defined by their probability of detection (P_D) and probability of false alarm (P_{FA}). Each are further discussed in Section 2.3. The P_{FA} is the primary factor used to adjust the threshold value in the LRT and the criteria used to evaluate the performance of various algorithms. The P_{FA} is usually set to an acceptable level to meet mission and resource constraints since each detection requires follow-up analysis.

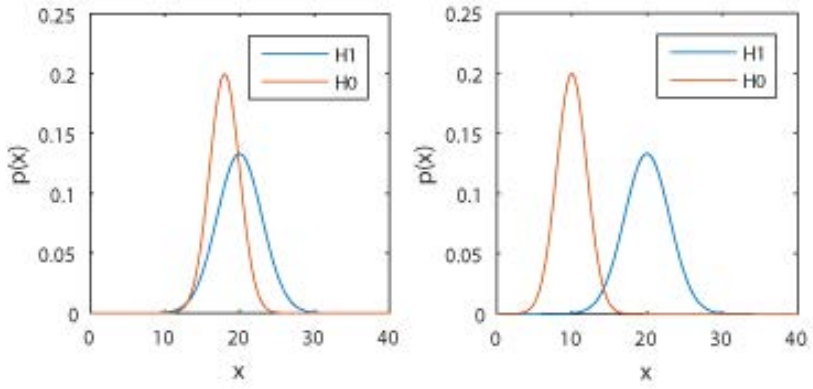

Figure 8. Illustration of difference between the separation of two probability distribution functions in a likelihood ratio test detection algorithm.

Point Detector.

One of the earlier programs dedicated to improving object detection using algorithms was the mid-1990s LINEAR program. The LINEAR algorithm developed within this program utilized imagery obtained from a ground-based electro-optic telescope to detect space objects using a BHT point detector [30]. Currently, the SST and other assets within the SSN use a modified version of the BHT point detector developed for LINEAR to make a detection decision on a single pixel in a given frame of data. The SNR level from the point detector, shown in Equation (2.2), is calculated by examining the received intensity at point, $d(x - x_0, y - y_0)$, from a single frame of data. This is a computationally simple algorithm designed to create a binary mask

to identify pixels that represent an object with an intensity over a set threshold. This method of detection relies on the assumption that the data is Gaussian distributed. Thus, when the background, B, is subtracted and the result divided by the standard deviation of the noise, σ_n, the result is the number of standard deviations the intensity of the pixel point is from the mean.

The first two steps of the LINEAR and SST detection process are the preprocessing procedures that involve reading several frames of data, registering the data using known stars within the frame and then averaging down to a single frame. This preprocessing removes telescope pointing error associated with the system while increasing the SNR of the image. A point source method of detection is employed in software where the registered images are normalized based on the assumption that the data is Gaussian distributed. Based on the LRT in Equation (2.2) , a binary mask of the image is calculated by examining each pixel location x_0, y_0,

$$SNR_{PD}(x, y) = \frac{(d(x - x_0, y - y_0) - B)}{\sigma_n} \underset{H_0}{\overset{H_1}{\gtrless}} \tau. \tag{2.2}$$

Where B is the background noise level in the image, σ_n is the localized standard deviation of the background noise and τ is the threshold level. The background is calculated by taking the median value of all N pixels in the x and y dimension around the x_0, y_0 pixel point,

$$B = median(d(x - x_0, y - y_0) \forall (x, y) \in [1 : N]). \tag{2.3}$$

Using the median value reduces the ability of bright pixel spots that contain known objects or noise spikes to skew the background level higher and adversely impact detection performance. The localized standard deviation of the background noise is

computed from the pixel values as

$$\sigma_n = \sqrt{\frac{\sum_{x=1}^{N}\sum_{y=1}^{N} d^2(x - x_0, y - y_0)}{N^2} - B^2}. \tag{2.4}$$

The left side of the inequality in Equation (2.2) represents the SNR level of the data at each pixel point and is assumed as a random variable from the standardized Gaussian distribution with zero mean and unit variance. The detection threshold, τ , then represents the number of standard deviations above the noise that is required to make an initial determination that an object is present at that pixel. The SST program typically uses a value of six as the detection threshold resulting in a P_{FA} $\approx 10^{-9}$. This seems extreme, however, a single frame in CCDs array is 6144 x 4086 pixels, containing over 25 million pixels [31]. At a P_{FA} rate of 10^{-9}, it is expected that a false alarm would occur on average once every 40 frames of data.

To achieve ideal performance in this detection method, the photons from the object must be focused down into a single pixel on the CCD detector in order to maximize the SNR. This is not the case for SST or many telescopes, where the PSF or size of the object on the detector is larger than a single pixel wide and is at least several pixels under best case scenarios. When the PSF is spread across several pixels, SNR decreases and will not meet the detection threshold required for initial detection by the algorithm.

Matched Filter.

A matched filter or correlation algorithm is utilized to achieve greater detection performance with a desired P_{FA} when searching for an unknown space object. The algorithm is based on correlating or matching the observed data with the expected PSF from a point source object. To perform the correlation with the captured image,

the expected PSF must be known. Typically, knowledge of the PSF has been limited to the long exposure case where the shape and size of the PSF can be determined from measurable statistical parameters of the atmosphere and can be considered, on average, a known value. However, Cain [32] has developed a matched filter method using the short exposure PSF. The PSF shape and location in this approach will be unknown due to atmospheric turbulence and tilt, however this is overcome using a MHT method.

Pohlig developed a unique matched filter algorithm based on the assumption that the background is the dominate source of noise in the image and is Poisson distributed instead of a traditional Gaussian assumption [27]. This premise leads to a dependence in the algorithm's detection threshold on the intensity of the target which would be unknown to an observer. Pohlig removes the intensity dependence by assuming that the target irradiance is low compared to the background. He further admits this assumption does not necessarily hold and is not accurate at a significantly low P_{FA} rate.

A Gaussian distribution has been widely used to describe the noise produced by CCD cameras. Using this distribution, the matched filter detection program referred to as SExtractor is used by multiple SSA detection programs [33], and is defined as

$$SNR_{MF} = \frac{\sum_{x=1}^{N}\sum_{y=1}^{N}(d(x,y)-B)h_L(x-x_0,y-y_0)}{\sigma_n\sqrt{\sum_{x=1}^{N}\sum_{y=1}^{N}h_L^2(x,y)}} \underset{H_0}{\overset{H_1}{\gtrless}} \gamma. \tag{2.5}$$

Where $d(x,y)$ is the single image frame, x_0, y_0 is the current pixel location being tested, N is the size of the window region of interest in pixels, $h_L(x,y)$ is the known long exposure PSF, B is the median background noise level in photons and σ_n is the standard deviation of the noise.

The performance of a matched filter algorithm is highly dependent on knowing the data from the long exposure PSF, h_L, which is correlated with the received image. The long exposure PSF is explained further in Section 2.4. However, in many SSA ground-based telescope systems the data is not sampled properly and the PSF will not appear as expected. Under-sampling will result in a non-symmetric PSF when captured on the CCD and will decrease the performance of the matched filter algorithm as was found by O'Dell [29].

Speckle Detection & Interferometry.

During short exposure image gathering, the atmospheric turbulence will induce random phase errors in the light as it propagates from the source to the detector. These random phase fluctuations cause the object to appear to change in position, shape and intensity, resulting in scintillation or speckle when observed over time. Speckle imaging and interferometry always involves taking many short exposure images, typically between 10 and a few thousand images with exposure times from a few milliseconds to a few tens of milliseconds [19]. Working in the short exposure regime has several benefits that researchers have been able to exploit to improve detection and imaging. The first is that the long exposure atmospheric optical transfer function (OTF) does not maintain high spatial frequency content which limits the resolution of imaging through turbulence. Additionally, there is the benefit of removing uncertainties in the registration of multiple frames when looking at the intensity of an object using short exposure images. Based on the Fourier shift theorem, a registration error or tilt in the image is the result of a phase shift in the Fourier domain. If the absolute value of the Fourier domain image is examined, the phase information and thus the spatial tilt error has been removed [19, 34].

Space object detection working with short exposure images in the spatial domain

with noise dominated by scintillation has been examined by Cain and Hardy in [32, 35]. This research involved building a LRT based on the probability distribution of the intensity fluctuations in short exposure images. Working under short exposure conditions, hundreds to thousands of frames can be collected in the same time that a single long exposure frame is captured by a CCD. The PSF in short exposure cases will have atmospheric induced tilt that requires the use of a MHT in order to accurately predict if an object is in the scene. Initial research in this technique has shown the potential to provide superior detection performance under certain conditions when compared to long exposure data of the same object.

Speckle interferometry has been researched and implemented at the AMOS telescope to improve the resolution and imaging capability of their 1.6 and 3.5-meter ground-based telescopes. This technique examines the Fourier transform of short exposure scintillated spatial image data obtained from a known space object and a nearby reference star. During post-processing, a Fourier transform is used to convert the image into the Fourier domain where the magnitude and phase information can be used to improve the resolution to near the diffraction limit of the system [22, 36, 19]. This is a result of the high spatial frequency content being preserved in the short exposure OTF.

Lucky imaging is another short exposure imaging technique that is used within the astronomical community primarily for image reconstruction [37, 38, 39, 40, 41, 42]. This technique involves taking tens to thousands of short exposure images and selecting a given percentage of them that are then registered and combined to obtain an improved image. Most commonly, the images are ranked based on their Strehl ratio which is a representation of the amount of phase aberrations present in the image due to turbulence. Typically, this method requires a guide star or beacon within the isoplanatic region to measure the quality of the image. Due to this constraint, this

method is nearly always limited to applications looking to improve the resolution of images containing a clearly visible object. This is only applied to detection in the sense that if imaging a known star system, an image with increased resolution could detect a binary star next to a known star. In a blind scan and survey detection method with no apparent object, it becomes difficult to register and combine frames while avoiding registration errors due to noise spikes in the data.

Detection and False Alarm Rates.

A metric commonly used within the SSA community in evaluating the performance of detection algorithms are the detection and false alarm rates [26, 27, 32]. These are also the metrics adopted within this dissertation. The detection rate is the rate at which an object is detected when an object actually exists at the tested location. The false alarm rate is the rate at which the algorithm detected an object at a location when no object exists. These rates are commonly referred to as the P_D and P_{FA}.

A Receiver Operating Characteristic (ROC) curve is used to plot of the probability of detection versus the probability of false alarm [43]. The ROC curve was first developed for analysis of radar signals and in signal detection theory. It was used to showcase the performance of different radar and signal detectors at various detection and false alarm rates. In this research, the traditional detector is replaced with an algorithm implemented in software that is making the detection decision. The use of a ROC curve allows the performance to be evaluated at all threshold values, τ. This allows various algorithms or processes to be tested and compared independent of a specific threshold value. The ROC curve is generated by calculating the P_D and P_{FA} for a range of threshold values and plotting the detection and false alarm rates.

Typically, the axis of a ROC curve plot are on a linear-linear scale. In order to capture the performance differences at extremely low false alarm rates a semi-log plot

is used with the $\log_{10}$ of the P_{FA} plotted on the x-axis, this method is used within other space object detection research [44, 26, 25]. Without a log scale, it would be impossible to distinguish the differences between similar algorithms at a false alarm rates near 10^{-9}. This approach is not a standard ROC curve and will be referred to as a Semi-log Receiver Operating Characteristic (LROC) curve throughout this research.

The approach used to generate the LROC curve is to utilize a large data set (either simulated or experimental) and examine the SNR values from the LRT, Λ, under each hypothesis [26, 25, 44]. These values are Gaussian distributed due to the Gaussian distribution noise of the data. With a significantly smaller sample of data points, the mean, μ_Λ, and variance, σ_Λ^2 of the SNR values can be found. Using a Gaussian cumulative distribution function (CDF) with the mean and variance, the P_D and P_{FA} can be calculated using Equations (2.6) and (2.7) [44]. Both the P_D and P_{FA} are based on a Gaussian CDF and their equations appear the same, however the statistics of the SNR values will vary between each.

The threshold value τ is varied across a range of values and the P_D and P_{FA} pair of values are noted. The LROC curve plots these pairs across all threshold values to illustrate the performance of multiple detection algorithms at a given false alarm rate.

$$P_D = \int_\tau^\infty \frac{\exp^{\frac{-(\Lambda-\mu_\Lambda)^2}{2\sigma_\Lambda^2}}}{\sqrt{2\pi\sigma_\Lambda^2}} d\Lambda. \tag{2.6}$$

$$P_{FA} = \int_\tau^\infty \frac{\exp^{\frac{-(\Lambda-\mu_\Lambda)^2}{2\sigma_\Lambda^2}}}{\sqrt{2\pi\sigma_\Lambda^2}} d\Lambda. \tag{2.7}$$

Confidence intervals on the LROC curve can be built using the statistics of the SNR values. In order to establish confidence intervals, the variance of the sample

mean and sample variance from the LRT values needs to be calculated. With a large set of N Gaussian random variables, the sample estimated mean, $\mu_{_{LRT}}$, and sample estimated variance, $\sigma^2_{_{LRT}}$, the variance of the sample mean and variance can be calculated. These are shown in Equations (2.8) and (2.9) [45, 46]. Each of these can be used to plot a new LROC curve that bounds the performance of each algorithm. For a LROC curve comparing two different algorithms, a lower bound can be applied to the higher performing algorithm which is plotted as the upper curve. Conversely, an upper bound can be established on the lower curve representing the lower performing algorithm. A confidence can then be applied when comparing the two algorithms performance at a given false alarm rate.

$$\mathrm{var}(\mu_{_{LRT}}) = \frac{\sigma^2_{_{LRT}}}{N}. \tag{2.8}$$

$$\mathrm{var}(\sigma^2_{LRT}) = \frac{2\sigma^4_{_{LRT}}}{N}. \tag{2.9}$$

To establish a 95% confidence interval when plotting the performance of two different algorithms on a LROC curve the mean and variance of each curve is adjusted by two standard deviations. The upper curve on the LROC plot is plotted using the Gaussian CDF and decreasing the mean by two standard deviations and increasing the variance by two standard deviations. An upper bound on the lower curve on the LROC plot can be plotted with the Gaussian CDF and a mean that is increased by two standard deviations and variance that has been decreased by two standard deviations.

2.4 Telescope & Optical Model

An accurate model for the telescope system, statistically correct PSF, and noise models along with correct statistical distributions are critical to the success of this research. Each of these components were an integral piece of the process in defining and developing new detection algorithms throughout this dissertation. This section will build a model for each component of the optical system that ultimately affects the statistics of the images obtained from ground-based telescopes for their space-based object detection mission. This includes a model of the telescope, the PSF due to the telescopes optics and the turbulent atmosphere that the light must propagate through during both short and long exposure images. In addition, additive noise sources and noise due to the discrete nature of photon counting by the CCD are examined.

Imaging System Model.

The principle operation of telescopes is to map the intensity of a scene in the object plane onto the imaging plane of the CCD detector of the optical system. Physically, this is a model of how the electromagnetic wave propagates through space from the object to the detector. This process is detailed by Goodman in [34] as a Rayleigh-Sommerfeld propagation derived from Maxwell's equations. In a space object scenario, the propagation distance between the object and detector is far enough that the propagation to the atmosphere can be modeled using a Fraunhofer propagation technique. This is ideal since Fraunhofer propagation can be implemented using a computationally simple Fourier transform. This process, known as Fourier optics, can be used to express the operation of mapping each point from the object plane to the imaging plane as the convolution of the object with the PSF as shown

in Equation (2.10) [34].

$$d(x,y) = \int_{-\infty}^{\infty}\int_{-\infty}^{\infty} o(u,v)h(x-u,y-v)\,du\,dv, \tag{2.10}$$

where $d(x,y)$ is the data of the received image at the pixel point x,y in the detector plane, u and v are coordinates in the object plane and h represents the PSF of the system. The object, $o(u,v)$, is a point source object in the object plane at the specified location.

As mentioned earlier in this chapter, one of the assumptions in this research is that the object is unresolvable and thus can be considered a point source at the detector. Therefore, based on Equation (2.10), it is expected that due to the linear shift invariant nature of the telescope system, the PSF is the image created on the detector by viewing a point source or spatial impulse through the optical system. As shown in Equation (2.11), the PSF of the imaging system is a combination of the optical system PSF and the atmospheric OTF using Fourier transforms [34, 24]. The PSF and OTF are inverse Fourier pairs describing the response of the system in the spatial and spatial frequency domains respectively.

$$h(x,y) = \mathcal{F}^{-1}\Big\{\mathcal{F}\big\{h_{opt}(x,y)\big\}H_{atm}(f_x,f_y)\Big\}. \tag{2.11}$$

The effects on the imaging system PSF due to aberrations in the optics of the telescope are captured in h_{opt}, while H_{atm} is the atmospheric OTF in the systems due to the turbulence encountered along the path of propagation. Each of these are further discussed in sections 2.4 and 2.4.

Optical System Model.

The optical PSF of the system, $h_{opt}(x, y)$, can be described by the Fourier transform of the pupil function, $P(m, n)$, of the telescope [34].

$$h_{opt}(x, y) = \left| \mathcal{F}\{P(m, n)\} \right|^2. \tag{2.12}$$

The pupil function of the system, $P(m, n)$ is defined below based on the physical properties of the aperture and phase errors in the optical path. The amplitude transfer function of the pupil, $A(m, n)$, is a masking function that mimics the geometry of the system pupil as illustrated in Figure 9 [34]. It is equal to one or zero corresponding to the locations in the pupil that pass light onto the system. In a perfect optical system with no aberrations, the pupil function is equal to the amplitude transfer function. All light that enters the optical system is transformed to the detector plane with no aberrations

$$P_{ideal}(m, n) = A(m, n). \tag{2.13}$$

In the more realistic case where optical aberrations are present due to non-uniformities in the optics of the system, all light captured by the primary mirror of the telescope will undergo measurable phase fluctuations along the optical path that can be represented as a phase error, θ_0, on the amplitude transfer function, $A(m, n)$.

$$P(m, n) = A(m, n)e^{j\theta_0(m,n)}. \tag{2.14}$$

The phase errors, θ_0, are represented as the summation of each weighted Zernike polynomial [47]. The weighting of each Zernike polynomial, a_j, is determined by the specific properties of the telescope and can be measured or solved for experimentally.

In the case for SST, the pupil amplitude transfer function masking would be a

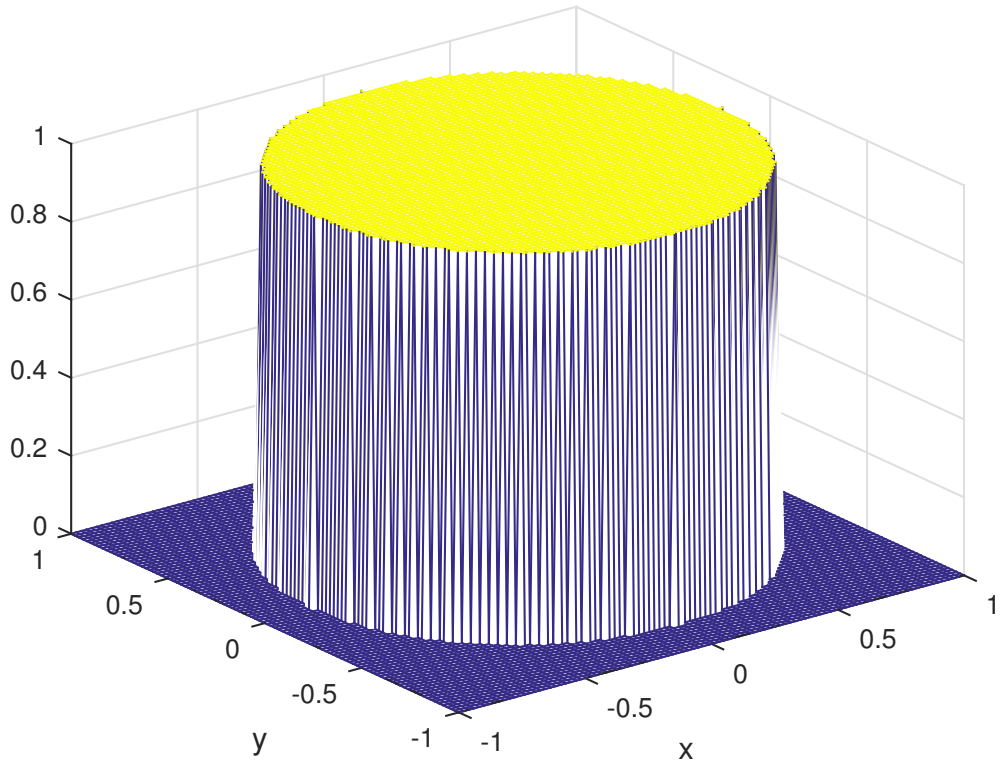

Figure 9. Amplitude of the pupil function with a circular aperture.

3.5 m circle with a 1.75 m obscuration in the middle. Previous research was conducted to solve for the weightings for each Zernike coefficient experimentally on the SST [13]. The first ten coefficient weighting are given in Table 1 and can be used to create an accurate model for the optical PSF associated with SST using Equations (2.12) and (2.14).

Atmospheric Model.

The effects of the atmosphere on the PSF is a random process that is well studied and can be modeled. As illustrated in Figure 10, random fluctuations in the index of refraction of air in the path of the light propagating from the source to the telescope result in phase distortions on the propagating field. These phase distortions result in

Table 1. First ten measured Zernike coefficients for the Space Surveillance Telescope [13].

Coefficient, a_j	Value (Waves)	Coefficient, a_j	Value (Waves)
a_1	2.09	a_6	-0.28
a_2	-5.95	a_7	0.28
a_3	-5.30	a_8	-0.73
a_4	6.89	a_9	0.36
a_5	1.26	a_{10}	-0.48

aberrations of the image once focused on the detector plane.

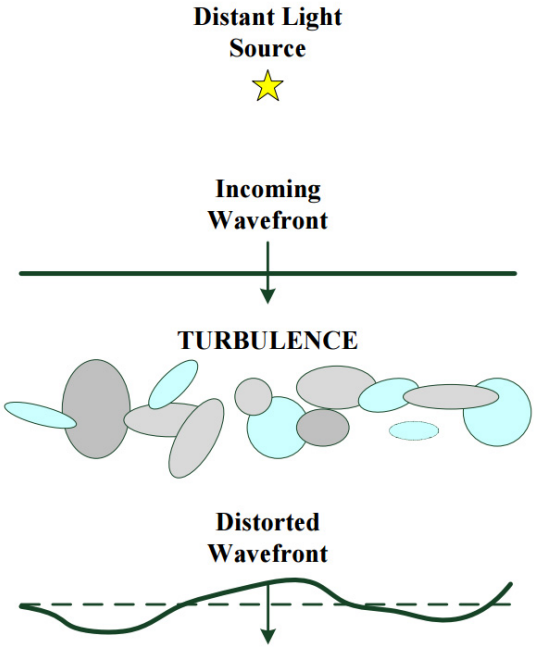

Figure 10. Distortion in the wavefront due to atmospheric turbulence [48].

This research uses two different models to determine the effects the atmosphere has on the PSF of the optical system. They are distinguished apart based on the exposure time or amount of time that the imaging system gathers light for a single frame of data. A short integration time, generally less than 10 ms, is modeled using a short exposure OTF, H_s [24]. Whereas, an integration time much greater than 10 ms would be modeled using a long exposure OTF, H_L.

Long Exposure Atmospheric Model.

In many SSA ground-based telescope systems, the integration time is significantly long enough that it only operates in the long exposure regime. For example, the SST operates with an integration time of between 100ms and 10 seconds [49] while the Panoramic Survey Telescope and Rapid Response System (Pan-STARRS) telescope has a significantly longer exposure time of between 30-60 seconds [50, 12]. The long exposure OTF is defined by Goodman in [24] as

$$H_L(f_x, f_y) = \exp\left[-3.44\left(\frac{\bar{\lambda} z \sqrt{f_x^2 + f_y^2}}{r_0}\right)^{\frac{5}{3}}\right]. \tag{2.15}$$

Where $\bar{\lambda}$ is the mean wavelength, z is the telescope focal length, f_x and f_y are spatial frequencies. The Fried parameter,r_0, called the seeing parameter, is a measure of the quality of optical propagations through the atmosphere [51, 24]. This term is used in multiple expressions to describe not only the quality of the atmosphere but the diffraction limited spot size for a given aperture since it is related to the coherence diameter of the atmosphere. Typical values of r_0 range between 5 and 20 cm depending on the site.

The long exposure OTF can be converted to the spatial domain by taking the inverse Fourier transform, this results in the long exposure PSF, $h_L(x, y)$.

$$h_L(x, y) = \mathcal{F}^{-1}\Big\{ H_L(f_x, f_y) \Big\}. \tag{2.16}$$

It is the inherent nature of the atmosphere over time to average out and this is shown in the zero mean Gaussian distribution of the random Zernike coefficients modeling the turbulent atmosphere. Thus, the long exposure PSF averages the random phase fluctuations due to the atmosphere to produce a spatially large PSF. On average, a long exposure PSF will contain zero tilt and will be an even and symmetric

function.

Short Exposure Atmospheric Model.

When operating at exposure times of around 10 ms or less, a short exposure OTF model is generally used [24]. As explained in Section 2.4, the short exposure PSF is the inverse Fourier transform of the short exposure OTF. The extremely short integration time limits the intensity or amount of light gathered by the system which makes imaging and detecting dim space objects inherently difficult. However, there are scenarios that short exposure imaging is used for improving imaging resolution and object detection in the SSA community [32, 19, 22, 36, 37, 38]. Due to the random nature of the atmospheric turbulence of a short time period, the short exposure OTF is described using a set of Zernike polynomials at each individual time instance. Previous AFIT research by Putnam has focused on building accurate individual Zernike phase screens with the correct temporal correlation statistics [52]. The coefficients used to build the set of Zernikes are zero mean Gaussian random variables with a given variance based primarily on the measure of the quality of the atmosphere, r_0 [47].

Noise Statistics.

In any optical telescope system there are numerous sources of noise that adversely impact the ability to detect dim objects. Ideally, every photon captured by a CCD pixel is converted into a digital count; however this is not usually the case. Sources of noise in the process include the discrete nature of photon counting, background light, read out noise, dark current and thermal noise. The systems deployed for SSA applications generally utilize hardware that limits the primary concern to the Poisson distributed photon counting noise and Gaussian distributed noise for all other sources

[27]. The manufacturers and operators of cameras attempt to minimize these noise sources using higher quality components while cooling the camera.

Photon Counting.

Photon noise or shot noise is a result of the CCD array in the detector plane array. The CCD is a discrete device that counts the number of photons that arrive at each element of the array [27]. The distribution of the photons is modeled as a Poisson process where photons arrive at random intervals with a mean number of photons, $\bar{k}$, arriving over a set time interval. The probability of k photons, $P(k)$, being counted at each pixel spot is given by the Poisson probability mass function (PMF) shown in Equation (2.17) [24]. Photon counting noise would cause the same object imaged at two different times to potentially appear to have different intensities.

$$P(k) = \frac{\bar{k}^k e^{-\bar{k}}}{k!} \text{ for } k = 0, 1, 2, 3... \tag{2.17}$$

Background Light.

Background noise is the result of any light or signal aside from the light propagating from the object that is measured by the detector. There are various sources of background noise and many are dependent on the situation, they include but are not limited to the sun, starlight and building or city lights reflecting off other surfaces and captured by the primary mirror of the telescope. The background can be estimated during data capture by moving to a nearby dark spot of the sky to calibrate the camera or can be accomplished during post-processing of the data by taking the median value of all N pixels in each dimension of the windowed data, $d(x, y)$, as shown in Equation (2.3).

Read Noise.

Photons are captured in each pixel of the CCD and are converted to a given number of electrons based on the gain of the camera. The electrons must then be passed in the circuitry to an analog to digital converter and transformed into a digital signal value. It is along this process of converting to electrons and reading out the value that multiple opportunities for noise arise in the camera's hardware. Under conditional space imaging this is not much of a concern because the variance of the Gaussian distributed read noise is significantly less than the photon counting variance noise. However, under short exposure night imaging, read noise can greatly degrade the SNR of images containing dim objects. This is especially true when many frames of short exposure data are averaged together as the read noise variance increases significantly. This is shown in Equation (2.18), as the variance for a given pixel in the image is related to the Poisson rate parameter, $\bar{K}$, the number of frames averaged together, F, and the readout noise variance, σ_{rn}^2. When imaging under daylight conditions, the higher photon count will drive this noise source to insignificant levels.

$$\mathbf{var}\{d(x,y)\} = F\bar{K} + F\sigma_{rn}^2. \tag{2.18}$$

2.5 Conclusion

The research in this dissertation focuses on improving space object detection algorithms already utilized with the community through transforming the data and improving the post-processing techniques. The goal of each new algorithm and processing technique is to increase the SNR of the image to improve the $\mathrm{P_D}$ for a given false alarm rate. Long and short exposure data and atmospheric turbulence models, along with accurate noise models are used throughout this research to ensure the validity of the developed data models and associated algorithms. The performance

of the various algorithms is plotted on a LROC curve to illustrate the probability of detection for a given false alarm rate across multiple algorithms. The algorithms developed in this research are compared to common approached such as a spatial point detector, spatial correlator, and a lucky imaging algorithm.

III. Improving Space Object Detection Using a Fourier Point Detection Algorithm

3.1 Introduction

In this chapter a new detection algorithm is proposed and developed for detecting space objects from images obtained using a ground-based telescope with the goal to improve space situational awareness. Most current space object detection algorithms rely on developing a LRT for the observed data based on a binary hypothesis test. These algorithms are based on the assumption that the observed data is Gaussian or Poisson distributed under both the null hypothesis, that an object is absent from the data, and the alternative hypothesis, that a low SNR space object is present in the data. The LRT algorithm in this chapter was developed based on the assumption that the distribution of the real component of the Fourier transform of the observed data will be different when a low SNR object is present in the data compared to when the data only contains background noise and known space objects. If the Fourier transform of the data contains a significantly different distribution then it could be used to increase the detection performance compared to a point detector or spatial correlator. The unique aspect of the research in this chapter is that unlike documented algorithms, this algorithm is based on data in the Fourier domain. It is the goal of this research that when transferring to the Fourier domain and developing statistical distributions on the Fourier transformed data that the LRT algorithms will provide superior detection performance through the usage of a statistically accurate designed LRT.

3.2 Telescope Data Model

An understanding of the expected data received by the optical system of the telescope is necessary to develop an algorithm optimized for detection. The algorithm presented in this chapter relies on typical spatial representation of the images. This spatial data is the signal detected by the CCD, later viewed as an image and manipulated by various detection processes for identifying unknown objects. The algorithm in this chapter proposes using a less common Fourier domain representation of the data. Under this transformation, each pixel in the image contains information on the frequency content of the image.

Spatial Data.

Referring to the model for the imaging system in Equation (2.10), a model for the expected signal on the detector CCD can be developed. This model will hold under both long and short exposure data since the model for the PSF is taken into account in later steps. The model for the point source space object absent of any atmospheric turbulence and noise is shown in Equation (3.1) as a Dirac function at some location u, v in the object plane scaled by the objects intensity, θ.

$$o(u, v) = \theta\delta(u, v). \tag{3.1}$$

Under the H_1 hypothesis, an object is present with some unknown intensity, θ, associated with it that will vary based on the position, orbit, orientation, material, time of day and observation angle along with other factors that affect the received intensity of the object. Under the H_0 hypothesis when no object is present, the model in Equation (3.1) is still accurate by setting the intensity of the object to zero.

The expected image on the detector, given in Equation (3.2), can be determined

using the model for the expected data along with the model for the space object (Equations (2.10) and (3.1)). There is some level of additive background noise, B, associated with the image as discussed in Section 2.4.

$$\mathrm{E}[d(x,y)] = \mathrm{E}\Bigg[\int_{-\infty}^{\infty}\int_{-\infty}^{\infty} \theta\delta(u,v)h(x-u,y-v)\,du\,dv\Bigg] + B. \tag{3.2}$$

Using the sifting property of the Dirac function [34], the double integral expression for the expected value of the image can be simplified.

$$\mathrm{E}[d(x,y)] = \theta h(x,y) + B. \tag{3.3}$$

The conditional expected value for the data under each hypothesis is developed. The object intensity, θ, is either an unknown value greater than zero under H_1 or equal to zero when no object is present under H_0.

$$\mathrm{E}[d(x,y)|H_0] = B. \tag{3.4}$$

$$\mathrm{E}[d(x,y)|H_1] = \theta h(x,y) + B. \tag{3.5}$$

As explained in Chapter 2, the background is a Gaussian distributed random variable with a measurable mean and variance from the pixel values in the image. To simplify the model for the data used in the development of the algorithm, the background is subtracted from all collected data. All detection algorithms researched for this dissertation follow a similar pre-processing step. The background subtracted data is defined as $d'(x,y)$.

$$d'(x,y) \triangleq d(x,y) - B. \tag{3.6}$$

Applying a conditional expectation, the models for the background subtracted data, $d'(x,y)$ are shown in Equations (3.7) and (3.8). When the background is re-

moved, and no object is present, on average no signal would be present. In the case of an object present, once the background is removed, the signal is an intensity scaled version of the PSF.

$$\mathrm{E}[d'(x,y)|H_0] = 0. \tag{3.7}$$

$$\mathrm{E}[d'(x,y)|H_1] = \theta h(x,y). \tag{3.8}$$

Fourier Domain Telescope Data.

A Fourier transform of the background-removed received data, $d'(x,y)$, is taken to develop a model for the statistics in the spatial frequency domain. The Fourier transform of the data is a spatial frequency domain representation of a typical spatial domain image. Frequency domain analysis is widely used in image reconstruction and post-processing to improve image resolution [53, 22]. Certain image reconstruction methods take advantage of removing the tilt component of atmosphere turbulence when working in the Fourier domain of short exposure images. This allows higher order aberrations to be averaged over many frames of data to obtain higher resolution images.

In this research, a standard Fourier kernel as given by Goodman is used to transfer between the spatial and frequency domain [24]. The Fourier transform of the background subtracted data is given by

$$\begin{aligned} D(f_x, f_y) &\triangleq \mathcal{F}\big\{d'(x,y)\big\} \\ &= \frac{1}{N}\sum_{x=1}^{N}\sum_{y=1}^{N} d'(x,y)e^{-j\frac{2\pi}{N}(xf_x+yf_y)}. \end{aligned} \tag{3.9}$$

Here $D(f_x, f_y)$ is defined as the Fourier transform of the background-removed data, N is the number of pixels in the window and f_x and f_y are the spatial frequency location in the transformed image.

The form of Equation (3.9) is similar to a random phasor sum which consist of a random amplitude and phase variable as described by Goodman [24]. Similar to the derivation of the statistics of a random phasor sum by Goodman, the real (r) and imaginary (i) components of the Fourier transformed data can be separated using Euler's formula and are defined as

$$\begin{aligned} D_r(f_x, f_y) &\triangleq \mathrm{Re}\big\{D(f_x, f_y)\big\} \\ &= \frac{1}{N}\sum_{x=1}^{N}\sum_{y=1}^{N} d'(x,y)\cos\left(\frac{2\pi}{N}(xf_x + yf_y)\right). \end{aligned} \tag{3.10}$$

$$\begin{aligned} D_i(f_x, f_y) &\triangleq \mathrm{Im}\big\{D(f_x, f_y)\big\} \\ &= \frac{1}{N}\sum_{x=1}^{N}\sum_{y=1}^{N} d'(x,y)\sin\left(\frac{2\pi}{N}(xf_x + yf_y)\right). \end{aligned} \tag{3.11}$$

For a large N, the real and imaginary components will be approximately Gaussian distributed due to the central limit theorem. As a Gaussian random variable, their PDF is defined by its mean and variance. Further work will be accomplished in calculating the mean and variance of the distribution under long exposure imaging scenario in order develop the conditional distribution under each hypothesis to construct a LRT. The key to the algorithm's success will be starting with accurate statistical assumptions which translates to distributions in the Fourier transformed telescope data.

Working with the real component of the Fourier transformed data, the Fourier domain LRT is given as

$$\Lambda = \frac{P(D_r(f_x, f_y)|H_1)}{P(D_r(f_x, f_y)|H_0)} \underset{H_0}{\overset{H_1}{\gtrless}} 1. \tag{3.12}$$

where the two conditional PDFs are Gaussian random variables with some mean and variance. The real component is used in this algorithm's development since long

exposure images on average are real and symmetric. Thus, the Fourier transform of a long exposure image is contained only in the real component. The imaginary component would contain noise and add no valuable information to the data.

3.3 Algorithm Development

This research is focused on improving space object detection using the LRT algorithm similar to other space detection algorithms [32, 26, 27, 30, 25]. The LRT will be developed for detecting objects using long exposure spatial data based on the two binary hypothesis decisions:

- $\boldsymbol{H_0}$: No object is present at the pixel point (x, y).
- $\boldsymbol{H_1}$: An unknown object is present at the pixel point (x, y).

As outlined in Chapter 2, a binary LRT is simply a ratio of the conditional probability distributions of the data and shown again in Equation (3.13).

$$\Lambda = \frac{P(d(x,y))\forall(x,y) \in [1,N]|H_1}{P(d(x,y))\forall(x,y) \in [1,N]|H_0} \underset{H_0}{\overset{H_1}{\gtrless}} 1. \tag{3.13}$$

Long Exposure Statistics.

Under the long exposure scenario, defined as integration times much greater than 10 ms by Goodman [24], the expected atmosphere at different time intervals is not random, but can be defined using the long exposure OTF given in Equation (2.15). Due to the averaging nature of turbulence over long time periods, the average PSF is both even and symmetric [24]. In order to develop a LRT, the PDFs under each hypothesis must be defined. Therefore, the mean and variance of the real component of the Fourier transformed and background-removed data under the two hypotheses must be calculated.

Null Hypothesis Statistics.

Using the model for the Fourier transformed data in Equation (3.10), the mean of the real component of the Fourier transformed data conditioned on H_0, μ_0, is equal to zero. This is due to the zero-mean nature of the modified spatial data, $d'(x, y)$, given in Equation (3.7).

$$\begin{aligned}\mu_0 &= \mathrm{E}[D_r(f_x, f_y)|H_0] \\ &= \frac{1}{N}\sum_{x=1}^{N}\sum_{y=1}^{N}\mathrm{E}[d'(x,y)|H_0]\cos\left(\frac{2\pi}{N}(xf_x + yf_y)\right) \\ &= 0.\end{aligned} \tag{3.14}$$

The variance of the conditional data, σ_0^2, can be calculated, however, it is not as straight forward as the mean.

$$\begin{aligned}\sigma_0^2 &= \mathrm{E}\big[\big((D_r(f_x, f_y)|H_0) - \mu_0\big)^2\big] \\ &= \mathrm{E}[(D_r(f_x, f_y)|H_0)^2] \\ &= \mathrm{E}\left[\left(\frac{1}{N}\sum_{x=1}^{N}\sum_{y=1}^{N} d'(x,y)\cos\big(\frac{2\pi}{N}(xf_x + yf_y)\big)\right)^2\right].\end{aligned} \tag{3.15}$$

Equation (3.15) can be expanded using additional variables, u and v, inside the summation. The variables u and v represent the spatial pixel locations in the data.

$$\sigma_0^2 = \frac{1}{N^2}\sum_{x=1}^{N}\sum_{y=1}^{N}\sum_{u=1}^{N}\sum_{v=1}^{N}\mathrm{E}\Big[d'(x,y)d'(u,v)\Big]\cos\big(\frac{2\pi}{N}(xf_x + yf_y)\big)\cos\big(\frac{2\pi}{N}(uf_x + vf_y)\big). \tag{3.16}$$

To evaluate all elements of the summation, there are two cases that must be evaluated separately and then summed. The first case is when $x \neq u$ and $y \neq v$. When this occurs the spatial elements of the data are at different pixel locations and are statistically independent. Referring to Equation (3.7), the variance is equal to

zero since the expected value term was found to be zero. Under the second case, $x = u$ and $y = v$.

Case 1:

$$\begin{aligned}\sigma_0^2 =& \frac{1}{N^2}\sum_{x=1}^{N}\sum_{y=1}^{N}\sum_{u=1}^{N}\sum_{v=1}^{N}\mathrm{E}\big[d'(x,y)\big]\mathrm{E}\big[d'(u,v)\big]\cos\big(\frac{2\pi}{N}(xf_x+yf_y)\big)\\ &\times\cos\big(\frac{2\pi}{N}(uf_x+vf_y)\big)\\ =&0.\end{aligned} \tag{3.17}$$

Case 2:

$$\sigma_0^2 = \frac{1}{N^2}\sum_{x=1}^{N^2}\sum_{y=1}^{N}\mathrm{E}\big[\big(d'(x,y)\big)^2\big]\cos^2\big(\frac{2\pi}{N}(xf_x+yf_y)\big).$$

The squared cosine term in the summation can be evaluated over the double summation by first using the cosine double angle formula [54]. When summing of all values of x and y from 1 to N, complete periods of the cosine function are summed and would equal zero for any number of complete periods. Thus, the cosine function in Equation (3.18) goes to zero and the double angle can be replaced with $\frac{1}{2}$.

$$\cos^2\big(\frac{2\pi}{N}(xf_x+yf_y)\big) = \frac{1}{2} + \frac{\cos\big(2\frac{2\pi}{N}(xf_x+yf_y)\big)}{2}. \tag{3.18}$$

Using the cosine double angle formula, the expression for the variance from Case 2 in

Equation (3.17) can be reduced to

$$\begin{aligned}
\sigma_0^2 &= \frac{1}{N^2}\sum_{x=1}^{N}\sum_{y=1}^{N}\mathrm{E}\big[\big(d'(x,y)\big)^2\big]\left(\frac{1}{2}\right) \\
&= \frac{1}{2N^2}\sum_{x=1}^{N}\sum_{y=1}^{N}\mathrm{E}\big[\big(d(x,y)-B\big)^2\big] \\
&= \frac{1}{2N^2}\sum_{x=1}^{N}\sum_{y=1}^{N}\mathrm{E}\big[\big(d(x,y)^2-2d(x,y)B+B^2\big)\big] \\
&= \frac{1}{2N^2}\sum_{x=1}^{N}\sum_{y=1}^{N}\big(\mathrm{E}\big[d(x,y)^2\big]-2\mathrm{E}\big[d(x,y)B\big]+\mathrm{E}\big[B^2\big]\big).
\end{aligned} \tag{3.19}$$

The physical number of photons measured by the optical detector, $d(x,y)$, is a Poisson distribution random variable which means that the Poisson moment theorem is applicable [24]. When k is a Poisson random variable with mean $\bar{k}$, the variance of a Poisson random variable is given as

$$\mathrm{E}[k^2] = \bar{k}^2 + k. \tag{3.20}$$

The Poisson moment theorem along with Equation (3.4) can be used to simplify the expression for the variance in Equation (3.19).

$$\begin{aligned}
\sigma_0^2 &= \frac{1}{2N^2}\sum_{x=1}^{N}\sum_{y=1}^{N}\big((B^2+B)-2B^2+B^2\big) \\
&= \frac{1}{2N^2}\sum_{x=1}^{N}\sum_{y=1}^{N}B \\
&= \frac{B}{2}.
\end{aligned} \tag{3.21}$$

Therefore, the variance under the null hypothesis is a sum of the two cases in Equation (3.17) resulting in

$$\sigma_0^2 = \frac{B}{2}. \tag{3.22}$$

Alternate Hypothesis Statistics.

Similar to the null hypothesis, the mean and variance of the real component of the background-removed Fourier transformed data, μ_1 and σ_1^2, in Equation (3.10) is needed to build the LRT. This data will be conditioned on the H_1 hypothesis being true, that is that an object is present in the scene.

Following the standard definition for calculating the mean,

$$\begin{aligned}\mu_1 &= \mathrm{E}\big[D_r(f_x, f_y)\big] \\ &= \mathrm{E}\bigg[\frac{1}{N}\sum_{x=1}^{N}\sum_{y=1}^{N}(d'(x,y)|H_1)\cos\big(\frac{2\pi}{N}(xf_x + yf_y)\big)\bigg].\end{aligned} \tag{3.23}$$

Euler's formula can be used to transfer the trigonometric function to a complex function which is easier to analytically evaluate [54]. Euler's formula states

$$e^{-j\theta} = \cos\theta - j\sin\theta. \tag{3.24}$$

There is an imaginary piece involved in Euler's formula, however the relationship shown in Equation (3.25) is true and will be used to find the mean.

$$\mathrm{Re}\{e^{-j\theta}\} = \cos\theta. \tag{3.25}$$

Thus, the complex form of the mean can then be found. This solution relies on the assumption that the data is long exposure therefore the average PSF is both entirely

real and symmetric.

$$\begin{aligned}\mu_1 &= \frac{1}{N}\mathrm{E}\Big[\sum_{x=1}^{N}\sum_{y=1}^{N}(d'(x,y)|H_1)\mathrm{Re}\big\{e^{-j\frac{2\pi}{N}(xf_x+yf_y)}\big)\big\}\Big] \\ &= \frac{1}{N}\sum_{x=1}^{N}\sum_{y=1}^{N}\mathrm{E}\big[(d'(x,y)|H_1)\big]\mathrm{Re}\big\{e^{-j\frac{2\pi}{N}(xf_x+yf_y)}\big)\big\} \\ &= \theta\ \mathrm{Re}\Big\{\frac{1}{N}\sum_{x=1}^{N}\sum_{y=1}^{N}h(x,y)e^{-j\frac{2\pi}{N}(xf_x+yf_y)}\big)\Big\}.\end{aligned} \tag{3.26}$$

The expression inside the real component operator of Equation (3.26) is the Fourier transform of the PSF which is known as the OTF, $\mathrm{H}(f_x, f_y)$. The mean is found to be

$$\mu_1 = \theta\mathrm{H}(f_x, f_y). \tag{3.27}$$

The calculations required to find the variance component of the PDF under hypothesis H_1 are more complex than what are used in the null hypothesis case due to the non-zero mean nature of the data. The standard form for the variance is defined as

$$\sigma_1^2 = \mathrm{E}\Big[\big(D_r(f_x, f_y) - \mathrm{E}[D_r(f_x, f_y)]\big)^2\Big]. \tag{3.28}$$

Using the calculated mean from Equation (3.27), expanding the square, and simplifying gives,

$$\sigma_1^2 = \mathrm{E}[D_r^2(f_x, f_y)] - \theta^2\mathrm{H}^2(f_x, f_y). \tag{3.29}$$

The expected value term in Equation (3.29) is evaluated separately and expanded

using the complex representation as was done in calculating the mean.

$$\begin{aligned}\mathrm{E}[D_r^2(f_x,f_y)] =&\mathrm{E}\left[\left(\frac{1}{N}\sum_{x=1}^{N}\sum_{y=1}^{N}(d'(x,y)|H_1)\mathrm{Re}\{e^{-j\frac{2\pi}{N}(xf_x+yf_y)}\}\right)^2\right]\\ =&\frac{1}{N^2}\mathrm{E}\Bigg[\sum_{x=1}^{N}\sum_{y=1}^{N}\sum_{u=1}^{N}\sum_{v=1}^{N}(d'(x,y)|H_1)(d'(u,v)|H_1)\\ &\times\mathrm{Re}\{e^{-j\frac{2\pi}{N}(xf_x+yf_y)}\}\mathrm{Re}\{e^{-j\frac{2\pi}{N}(uf_x+vf_y)}\}\Bigg].\end{aligned}\tag{3.30}$$

Where u and v are additional variables used to keep track of the indices in the summation. The variables u and v represent the pixel locations in the data in the same way x and y do. The variables are added in order to keep terms separated over the quadruple summation. Equation (3.30) is split into two cases to evaluate for all possible outcomes across the 4 summation variables. The first case is when the two points are the same, meaning $x = u$ and $y = v$. The second case occurs when the two points are statistically independent meaning that $x \neq u$ and $y \neq v$. A Dirac function is used to separate and evaluate the two cases.

Under the first case,

$$
\begin{aligned}
\mathrm{E}[D_r^2(f_x,f_y)|x=u\wedge y=v] =& \frac{1}{N^2}\mathrm{E}\Bigg[\sum_{x=1}^{N}\sum_{y=1}^{N}\sum_{u=1}^{N}\sum_{v=1}^{N}(d'(x,y)|H_1)(d'(u,v)|H_1) \\
& \times \mathrm{Re}\Big\{e^{-j\frac{2\pi}{N}(xf_x+yf_y)}\Big\}\mathrm{Re}\Big\{e^{-j\frac{2\pi}{N}(uf_x+vf_y)}\Big\}\Bigg]\delta(x-u,y-v) \\
=& \frac{1}{N^2}\mathrm{E}\Bigg[\sum_{x=1}^{N}\sum_{y=1}^{N}(d'^2(x,y)|H_1)\mathrm{Re}\Big\{e^{-j2\frac{2\pi}{N}(xf_x+yf_y)}\Big\}\Bigg] \\
=& \frac{1}{N^2}\sum_{x=1}^{N}\sum_{y=1}^{N}\mathrm{E}\Big[(d(x,y)|H_1-B)^2\Big]\mathrm{Re}\Big\{e^{-j2\frac{2\pi}{N}(xf_x+yf_y)}\Big\} \\
=& \frac{1}{N^2}\sum_{x=1}^{N}\sum_{y=1}^{N}\mathrm{E}\Big[((d^2(x,y)|H_1)-2B(d(x,y)|H_1)+B^2)\Big] \\
& \times \mathrm{Re}\Big\{e^{-j2\frac{2\pi}{N}(xf_x+yf_y)}\Big\} \\
=& \frac{1}{N^2}\sum_{x=1}^{N}\sum_{y=1}^{N}\Big(\mathrm{E}\big[(d^2(x,y)|H_1)\big]-2B\mathrm{E}\big[(d(x,y)|H_1)\big] \\
& +\mathrm{E}\big[B^2\big]\Big)\mathrm{Re}\Big\{e^{-j2\frac{2\pi}{N}(xf_x+yf_y)}\Big\}.
\end{aligned}
\tag{3.31}
$$

Using the Poisson moment theorem from Equation (3.20) and the model for the data under the H_1 hypothesis given in Equation (3.5), this term can be simplified.

$$
\begin{aligned}
\mathrm{E}[D_r^2(f_x, f_y)] =& \frac{1}{N^2}\sum_{x=1}^{N}\sum_{y=1}^{N}\Big(\mathrm{E}\big[d^2(x,y)|H_1\big] - 2B\mathrm{E}\big[d(x,y)|H_1\big] + \mathrm{E}\big[B^2\big]\Big) \\
& \times \mathrm{Re}\big\{e^{-j2\frac{2\pi}{N}(xf_x+yf_y)}\big\} \\
=& \frac{1}{N^2}\sum_{x=1}^{N}\sum_{y=1}^{N}\Big(\big((\theta h(x,y)+B)^2 + \theta h(x,y) + B\big) - 2B\big(\theta h(x,y)+B\big) \\
& + B^2\big)\mathrm{Re}\big\{e^{-j2\frac{2\pi}{N}(xf_x+yf_y)}\big\}\Big) \\
=& \frac{1}{N^2}\sum_{x=1}^{N}\sum_{y=1}^{N}\Big(\big(\theta^2 h^2(x,y) + \theta h(x,y) + B\big)\mathrm{Re}\big\{e^{-j2\frac{2\pi}{N}(xf_x+yf_y)}\big\}\Big).
\end{aligned}
\tag{3.32}
$$

The next step is to evaluate the second case of Equation (3.30) where $x \neq u$ and

$y \neq v$.

$$
\begin{aligned}
\mathrm{E}[D_r^2(f_x,f_y)|x\neq u \wedge y \neq v] = &\frac{1}{N^2}\mathrm{E}\Bigg[\sum_{x=1}^{N}\sum_{y=1}^{N}\sum_{u=1}^{N}\sum_{v=1}^{N}\Bigg((d'(x,y)|H_1)(d'(u,v)|H_1)\\
&\times \mathrm{Re}\Big\{e^{-j\frac{2\pi}{N}(xf_x+yf_y)}\Big\}\mathrm{Re}\Big\{e^{-j\frac{2\pi}{N}(uf_x+vf_y)}\Big\}\Bigg)\Bigg]\big(1-\delta(x-u,y-v)\big)\\
=&\frac{1}{N^2}\sum_{x=1}^{N}\sum_{y=1}^{N}\sum_{u=1}^{N}\sum_{v=1}^{N}\Bigg(\mathrm{E}\big[d'(x,y)|H_1\big]\mathrm{E}\big[d'(u,v)|H_1\big]\mathrm{Re}\Big\{e^{-j\frac{2\pi}{N}(xf_x+yf_y)}\Big\}\mathrm{Re}\Big\{e^{-j\frac{2\pi}{N}(uf_x+vf_y)}\Big\}\Bigg)\\
&\times\big(1-\delta(x-u,y-v)\big)\\
=&\frac{1}{N^2}\sum_{x=1}^{N}\sum_{y=1}^{N}\sum_{u=1}^{N}\sum_{v=1}^{N}\Bigg((\theta h(x,y))(\theta h(u,v))\mathrm{Re}\Big\{e^{-j\frac{2\pi}{N}(xf_x+yf_y)}\Big\}\mathrm{Re}\Big\{e^{-j\frac{2\pi}{N}(uf_x+vf_y)}\Big\}\Bigg)\\
&\times\big(1-\delta(x-u,y-v)\big)\\
=&\frac{1}{N^2}\sum_{x=1}^{N}\sum_{y=1}^{N}\sum_{u=1}^{N}\sum_{v=1}^{N}\Bigg((\theta h(x,y))(\theta h(u,v))\mathrm{Re}\Big\{e^{-j\frac{2\pi}{N}(xf_x+yf_y)}\Big\}\mathrm{Re}\Big\{e^{-j\frac{2\pi}{N}(uf_x+vf_y)}\Big\}\Bigg)\\
&-\frac{1}{N^2}\sum_{x=1}^{N}\sum_{y=1}^{N}\Bigg((\theta^2h^2(x,y))\mathrm{Re}\Big\{e^{-j2\frac{2\pi}{N}(xf_x+yf_y)}\Big\}\Bigg).
\end{aligned}
\tag{3.33}
$$

Again, under the long exposure case the PSF is real, Equation (3.33) can be simplified by recognizing that it is contains Fourier transforms of the PSF. This simplification gives,

$$
\mathrm{E}[D_r^2(f_x,f_y)] = \theta^2H^2(f_x,f_y) - \frac{1}{N^2}\sum_{x=1}^{N}\sum_{y=1}^{N}\Bigg((\theta^2h^2(x,y))\mathrm{Re}\Big\{e^{-j2\frac{2\pi}{N}(xf_x+yf_y)}\Big\}\Bigg).
\tag{3.34}
$$

The results from the two cases (Equation (3.32) and (3.34)) must be summed and

simplified.

$$\begin{aligned}
\mathrm{E}[D_r^2(f_x,f_y)] =& \frac{1}{N^2}\sum_{x=1}^{N}\sum_{y=1}^{N}\left(\big(\theta^2h^2(x,y)+\theta h(x,y)+B\big)\mathrm{Re}\big\{e^{-j2\frac{2\pi}{N}(xf_x+yf_y)}\big\}\right)\\
&+\theta^2H^2(f_x,f_y)-\frac{1}{N^2}\sum_{x=1}^{N}\sum_{y=1}^{N}\left((\theta^2h^2(x,y))\mathrm{Re}\big\{e^{-j2\frac{2\pi}{N}(xf_x+yf_y)}\big\}\right)\\
=&\frac{1}{N^2}\sum_{x=1}^{N}\sum_{y=1}^{N}\left(\big(\theta h(x,y)+B\big)\mathrm{Re}\big\{e^{-j2\frac{2\pi}{N}(xf_x+yf_y)}\big\}\right)+\theta^2H^2(f_x,f_y).
\end{aligned} \tag{3.35}$$

Equation (3.35) can be converted back into a trigonometric function and simplified using the cosine double angle function shown in Equation (3.18). Additionally, summing up all points of the PSF will always equal one and leads to the following simplification.

$$\begin{aligned}
\mathrm{E}[D_r^2(f_x,f_y)] =& \frac{1}{N^2}\sum_{x=1}^{N}\sum_{y=1}^{N}\left(\big(\theta h(x,y)+B\big)\left(\frac{1}{2}+\frac{cos\big(2\frac{2\pi}{N}(xf_x+yf_y)\big)}{2}\right)\right)\\
&+\theta^2H^2(f_x,f_y)\\
=&\frac{1}{N^2}\sum_{x=1}^{N}\sum_{y=1}^{N}\left(\frac{\theta h(x,y)}{2}+\frac{B}{2}+\frac{\theta h(x,y)}{2}\cos\big(2\frac{2\pi}{N}(xf_x+yf_y)\big)\right.\\
&\left.+\frac{B}{2}\cos\big(2\frac{2\pi}{N}(xf_x+yf_y)\big)\right)+\theta^2H^2(f_x,f_y)\\
=&\frac{\theta}{2N^2}+\frac{B}{2}+\frac{\theta}{2N^2}\sum_{x=1}^{N}\sum_{y=1}^{N}h(x,y)\cos\big(2\frac{2\pi}{N}(xf_x+yf_y)\big)\\
&+\frac{B}{2N^2}\sum_{x=1}^{N}\sum_{y=1}^{N}\cos\big(2\frac{2\pi}{N}(xf_x+yf_y)\big)+\theta^2H^2(f_x,f_y).
\end{aligned} \tag{3.36}$$

Using the frequency scaling property of Fourier transforms [34], Equation (3.36) can

be further simplified.

$$\mathrm{E}[D_r^2(f_x,f_y)] = \frac{\theta}{2N^2} + \frac{B}{2} + \frac{\theta H(2f_x,2f_y)}{N} + \frac{B}{2N}\delta(2f_x,2f_y) + \theta^2 H^2(f_x,f_y). \quad (3.37)$$

Lastly, the results from Equation (3.37) can be substituted into Equation (3.29) to arrive at the solution to the variance.

$$\sigma_1^2 = \frac{\theta}{2N^2} + \frac{B}{2} + \frac{\theta H(2f_x,2f_y)}{N} + \frac{B}{2N}\delta(2f_x,2f_y). \quad (3.38)$$

Under a dim object scenario, the target intensity, θ, is near the background level, N is over 100, and the OTF, H, is a number less than or equal to one. Thus, the variance is going to be dominated by the $\frac{B}{2}$ term and can be approximated.

$$\sigma_1^2 \approxeq \frac{B}{2}. \quad (3.39)$$

Developed Likelihood Ratio Test.

The LRT utilizing long exposure data can now be developed based on the mean and variances found under both hypotheses (Equations (3.14), (3.22), (3.27) and (3.39)) applied to a Gaussian PDF. As explained in Section 3.2, the LRT is defined as the ratio of two conditional Gaussian random variables following Equation (3.12).

$$\begin{aligned} P(D_r(f_x,f_y)|H_1) &= \frac{1}{\sqrt{2\pi\sigma_1^2}} e^{-\frac{(D_r(f_x,f_y)-\mu_1)^2}{2\sigma_1^2}} \\ &= \frac{1}{\sqrt{\pi B}} e^{-\frac{(D_r(f_x,f_y)-\theta \mathrm{H}(f_x,f_y))^2}{B}}. \end{aligned} \quad (3.40)$$

$$\begin{aligned} P(D_r(f_x,f_y)|H_0) &= \frac{1}{\sqrt{2\pi\sigma_0^2}} e^{-\frac{(D_r(f_x,f_y)-\mu_0)^2}{2\sigma_0^2}} \\ &= \frac{1}{\sqrt{\pi B}} e^{-\frac{D_r^2(f_x,f_y)}{B}}. \end{aligned} \quad (3.41)$$

Thus the LRT is

$$\begin{aligned}\Lambda =& \frac{P(D_r(f_x,f_y)|H_1)}{P(D_r(f_x,f_y)|H_0)} \underset{H_0}{\overset{H_1}{\gtrless}} 1 \\ =& \frac{\frac{1}{\sqrt{\pi B}} e^{-\frac{(D_r(f_x,f_y)-\theta \mathrm{H}(f_x,f_y))^2}{B}}}{\frac{1}{\sqrt{\pi B}} e^{-\frac{D_r^2(f_x,f_y)}{B}}} \underset{H_0}{\overset{H_1}{\gtrless}} 1 \\ =& e^{(2D_r(f_x,f_y)\theta \mathrm{H}(f_x,f_y)-\theta^2 \mathrm{H}^2(f_x,f_y))} \underset{H_0}{\overset{H_1}{\gtrless}} 1.\end{aligned} \tag{3.42}$$

To test the data against the LRT it is ideal to isolate the data and compare that to a threshold value. The real component of the Fourier transformed data is isolated and results in

$$D_r(f_x,f_y) \underset{H_0}{\overset{H_1}{\gtrless}} \frac{\theta \mathrm{H}(f_x,f_y)}{2}. \tag{3.43}$$

The terms on the right-hand side of Equation (3.43) are defined as the threshold value, τ.

$$\frac{\theta \mathrm{H}(f_x,f_y)}{2} \triangleq \tau. \tag{3.44}$$

Similar to the other detection algorithms as discussed in Chapter 2, this is a simple test comparing the real component of the Fourier transformed telescope data to a single threshold. Using a simple threshold value allows the $\mathrm{P_{FA}}$ to be set at the desired level based on the threshold.

3.4 Experiment Description

To evaluate the performance of the algorithm, data was simulated in MATLAB to test the performance of the Fourier domain algorithm against a spatial domain correlator and a point detector algorithm. The model generates realistic data that would mimic the data received from a telescope conducting space object detection. The MATLAB model accounts for random fluctuations in intensity due to the atmosphere

along with the Poisson distributed randomness associated with photon counting at the CCD sensor.

Atmospheric Turbulence.

To accurately generate telescope data, the model for the atmospheric turbulence must create realistic phase screens that mimic long exposure turbulence statistics. Previous research has shown that without the presence of extreme winds or very long times between images the statistics of the atmosphere will contain correlation between each time instance [52, 44]. Over the long exposure times examined in this research, the phase error induced by the atmosphere will be correlated and evolve over time. Utilizing the research of Putnam [52], the Zernike coefficients used to generate the model for the atmosphere are based on Taylor's frozen flow hypothesis [55] and will evolve over time depending on the correlation coefficient between time instances. This model allows thousands of correlated instances of the atmosphere to be generated in MATLAB given the atmospheric seeing conditions and wind speeds. One instance of a simulated short exposure and long exposure PSF from this data set is shown in Figure 11.

Figure 11. Single realization of the short exposure PSF (left side). Single realization of the long exposure PSF (right side).

Simulated Data.

The long exposure PSF was used to model the point source object following Equation (2.15). The long exposure model implies that integration times of greater than 100 ms are used to capture each frame and which averages the lower order Zernike aberrations to obtain a blurred and spread PSF. Combining the model for the data, optical system, and the atmospheric turbulence, simulated data is generated in MATLAB for both the H_1 and H_0 hypotheses. The signal background and target intensity can be varied to give varying SNR levels to evaluate performance differences. Two different references are used in this chapter when characterizing SNR values. Either a point source SNR or spatial correlator SNR. Each of these are significantly different due to the intensity needed to achieve the desired SNR value for each algorithm. Point source SNR values of one, three and six were examined for this research. As explained in Chapter 2, a point detector SNR six object implies that the normalized average signal is greater than six standard deviations from the noise floor of the background. The intensity level for a spatial correlator SNR six object is significantly less than a point detector. The parameters used to simulate this data in MATLAB are summarized in Table 2. An individual realization of the images under the H_1 hypothesis at different signal levels are shown in Figure 12. Spatial correlator SNR six data was also simulated for analysis in this research and is shown in Figure 13.

Table 2. Parameters used to create simulated data in MATLAB.

Parameter	**Value**
Background Intensity, B	10 Photons/pixel
Object Intensity, θ	11,000 Photons (Point Detector SNR 6) 1,050 Photons (Correlator SNR 6)
Telescope Diameter, D	0.50 m
Fried Parameter, r_0	5.0 cm
Grid size, N	51 x 51 pixels
Number of Frames	10,000

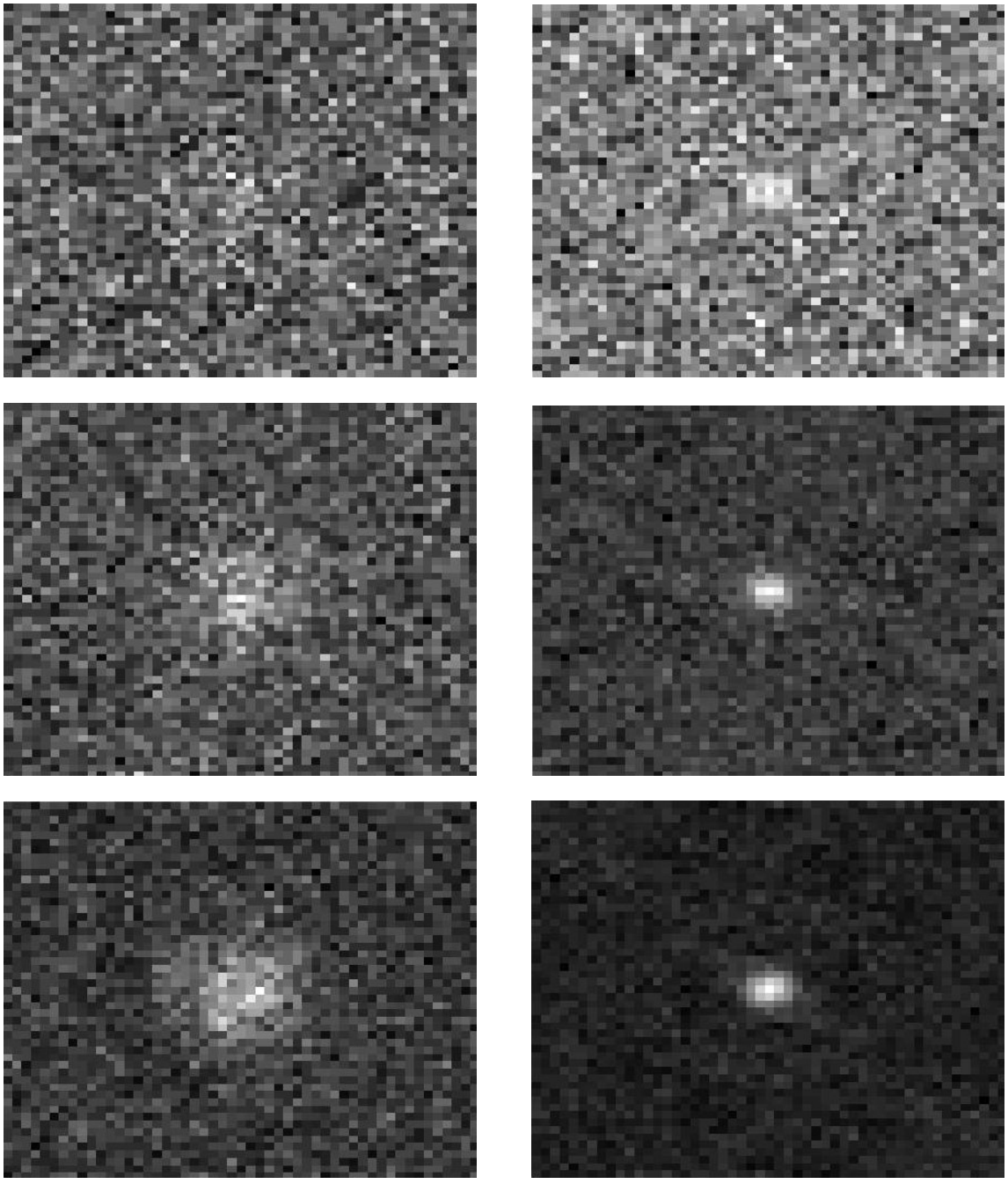

Figure 12. Simulated H_1 spatial data (left side). Real component of the Fourier transform of the H_1 data (right side). Top row - point detector SNR 1, middle row - point detector SNR 3, bottom row - point detector SNR 6.

Under the H_0 hypothesis, no object is present. However, it is possible that noise could appear as an object. To simulate data under this hypothesis, the intensity is

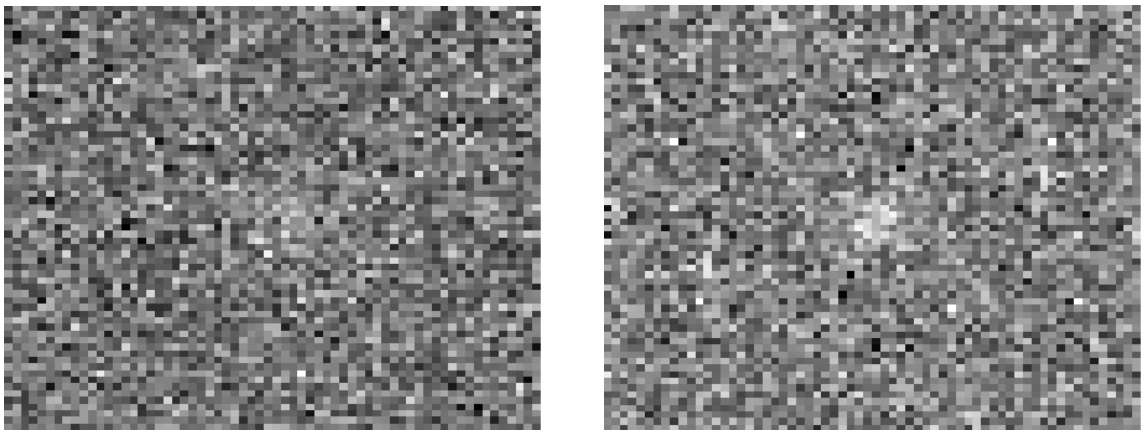

Figure 13. Spatial correlator SNR 6 simulated H_1 spatial data (left side). Real component of the Fourier transform of the H_1 data (right side).

set to zero and the same process implemented to create the H_1 data is utilized. One realization of data under the H_0 hypothesis is shown in Figure 14.

Although not apparent to the human eye when looking at the examples in Figures 12 and 13, it should be noted that there is a significant different in point detector SNR 6 data and correlator SNR 6 data. Due to the inherent nature of the algorithms, a point detector SNR 6 will require significantly more photons than a spatial correlator.

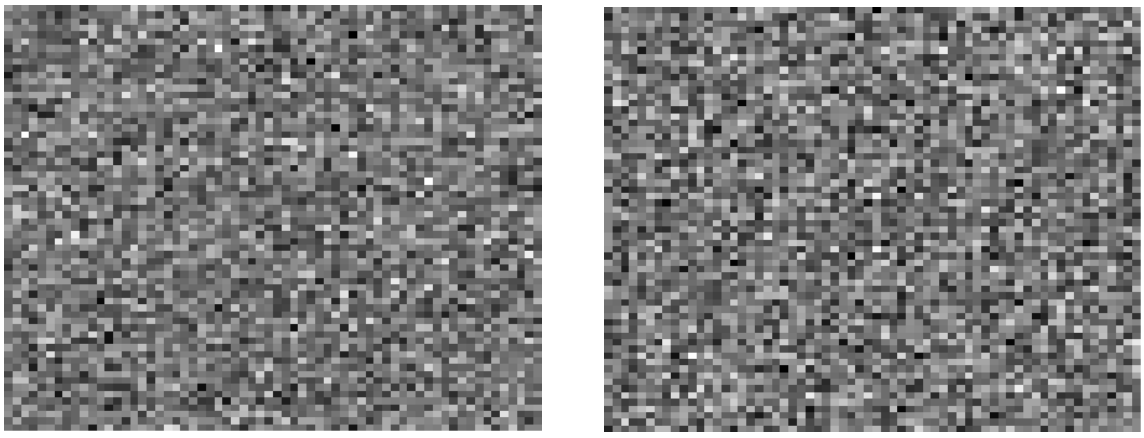

Figure 14. Simulated H_0 spatial data (left side). Real component of the Fourier transform of the H_0 data (right side).

Algorithm Implementation.

The spatial correlator, Fourier point detector and point detector algorithms are implemented in MATLAB following Equations (2.2), (2.5) and (3.43). Multiple correlated short exposure PSFs are generated and averaged together to obtain a long exposure PSF. The intensity scaled PSF with additive Gaussian background noise and Poisson photon counting noise was incorporated to obtain a set of long exposure images. Each of the three algorithms use the same data set and no additional data to ensure bias is not introduced into the process. The algorithm processes both the H_1 and the H_0 data in the exact same manner and has no knowledge on if an object is present in the scene or not.

3.5 Results & Analysis

A LROC curve was used for comparing performance of the three detection algorithms. The LROC curve, as described in Chapter 2, contains information on the probability of detection against the probability of false alarm. This plot is useful since this research is looking to increase the detection performance while maintaining a desired false alarm rate. By examining a specific spot on the curve, a desired false alarm rate can be set and the detection probability examined for multiple algorithms.

Receiver Operating Characteristic Curve.

Using Equation (2.6), the P_D is computed using the Gaussian CDF with the mean, Λ, and variance, σ_Λ^2, of the SNR statistics from the LRT [44].

Likewise, the P_{FA} is calculated using the same method however the LRT statistic are based on the algorithm's performance using data from the H_0 hypothesis. The false alarm probability is calculated as shown in Equation (2.7).

The LRT SNR values for each algorithm using the point detector SNR 6 data set

are shown in Figures 15, 16 and 17. The LRT values are also computed using the spatial correlator SNR 6 data set and shown in Figures 18, 19 and 20.

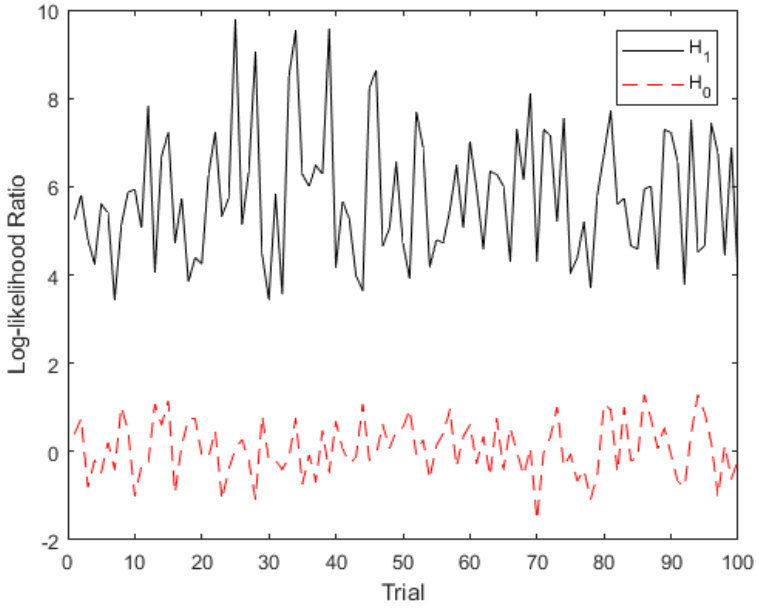

Figure 15. LRT values for the point detector algorithm using point detector SNR 6 data.

Using the results from each LRT, the LROC curve for each data set is generated and shown in Figures 21 and 22. In Figure 21, there appears to be only 2 lines, however, both the Spatial and Fourier correlation algorithms had the same performance and are plotted on each other. To better visualize the difference at extremely low false alarm rates, the $\log_{10}$ of the false alarm rate is plotted.

The statistics of the LRT SNR values are used to generate the LROC curves for each algorithm. When the curves are plotted on the same LROC plot, the P_D for a specific P_{FA} is illustrated for both the spatial and Fourier detectors. The LROC curves in Figures 21 and 22, shows that for any given P_{FA}, the spatial and Fourier correlation detectors significantly outperform the point detector since the detection probability is significantly higher for a given false alarm rate. The Fourier point source

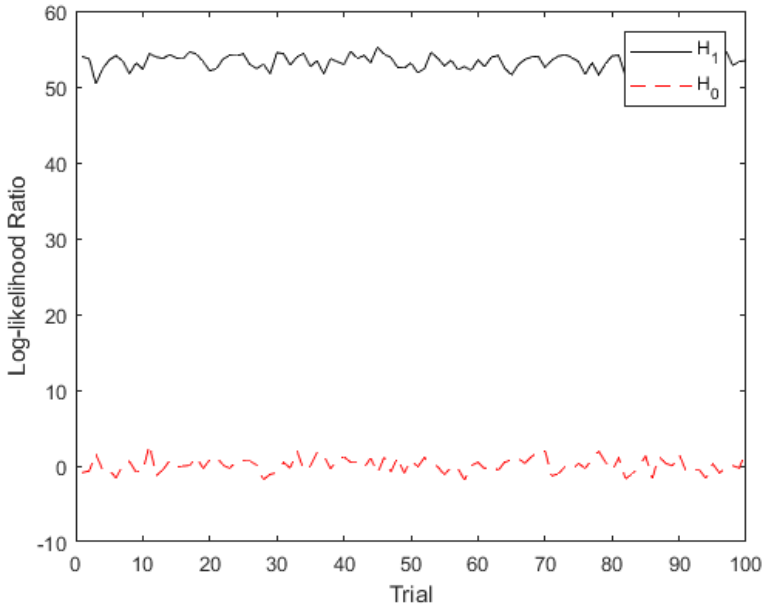

Figure 16. LRT values for the spatial correlator algorithm using point detector SNR 6 data.

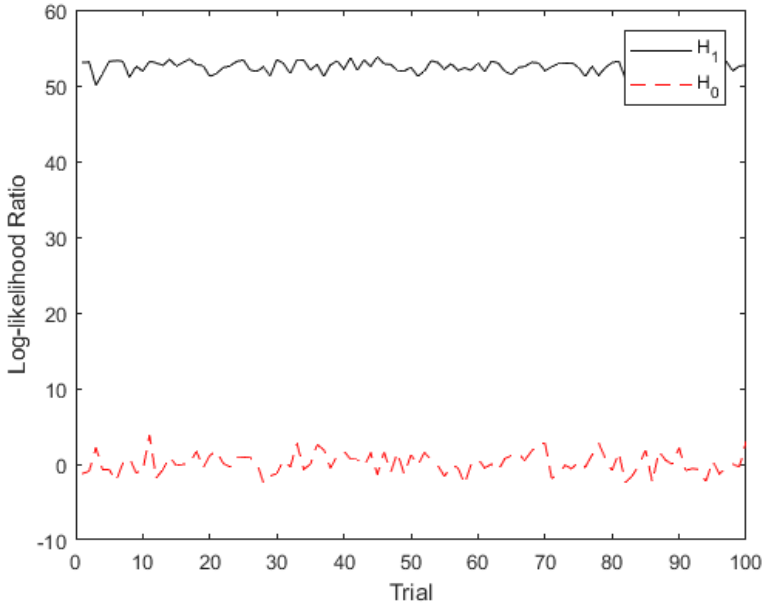

Figure 17. LRT values for the Fourier correlator algorithm using point detector SNR 6 data.

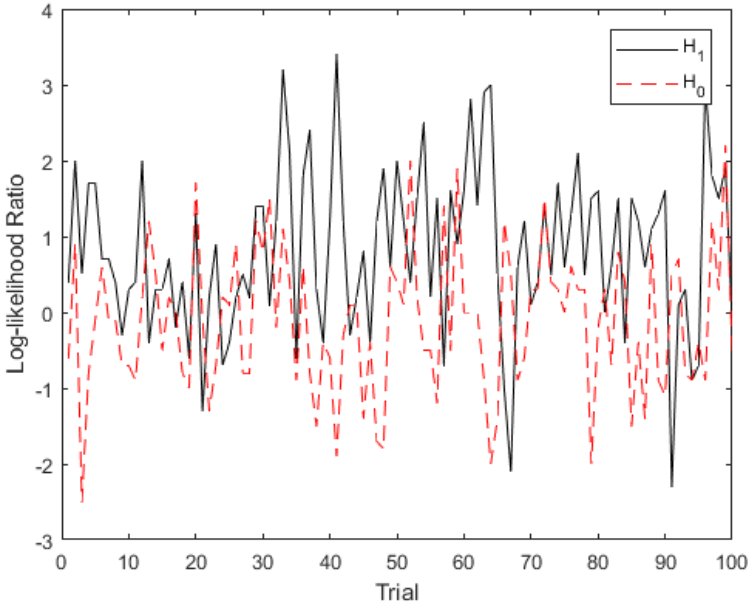

Figure 18. LRT values for the point detector algorithm using spatial correlator SNR 6 data.

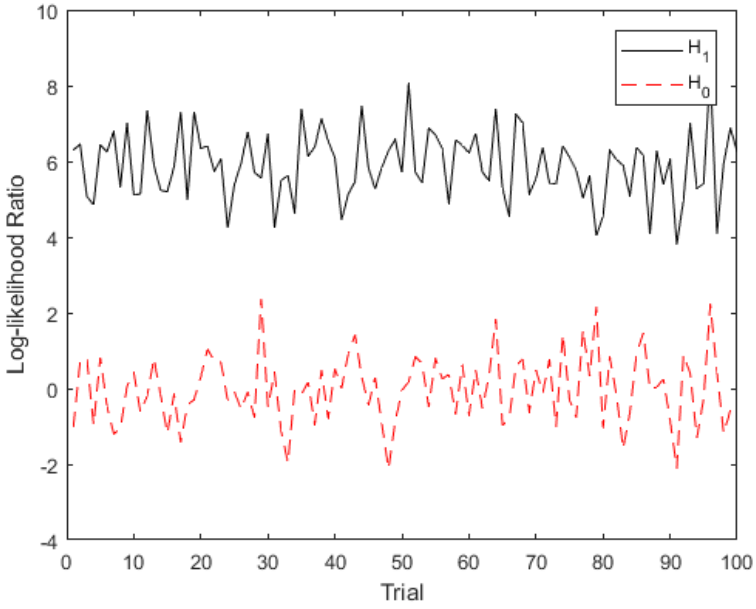

Figure 19. LRT values for the spatial correlator algorithm using spatial correlator SNR 6 data.

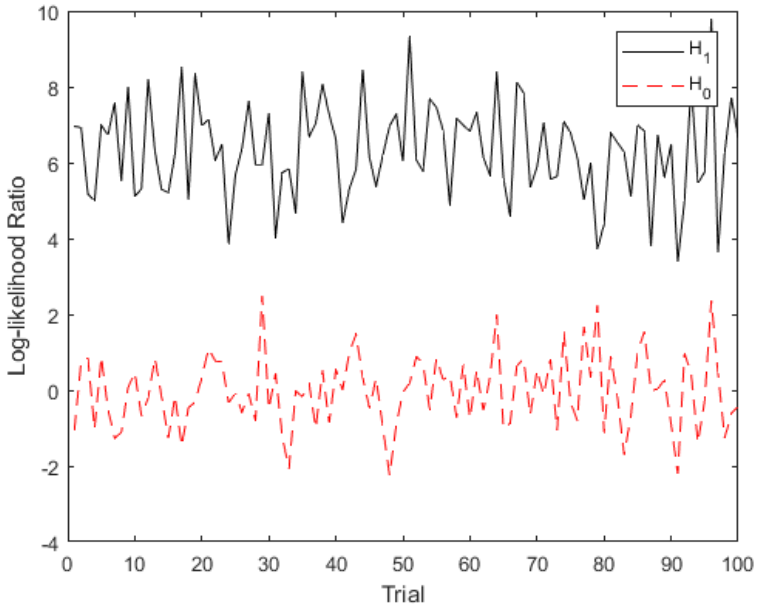

Figure 20. LRT values for the Fourier correlator algorithm using spatial correlator SNR 6 data.

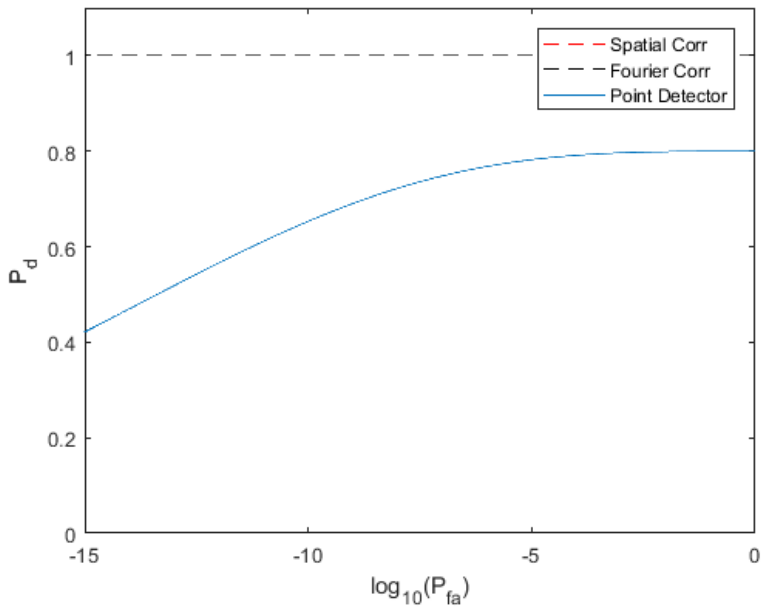

Figure 21. LROC curve using point detector SNR 6 data for each of the three algorithms.

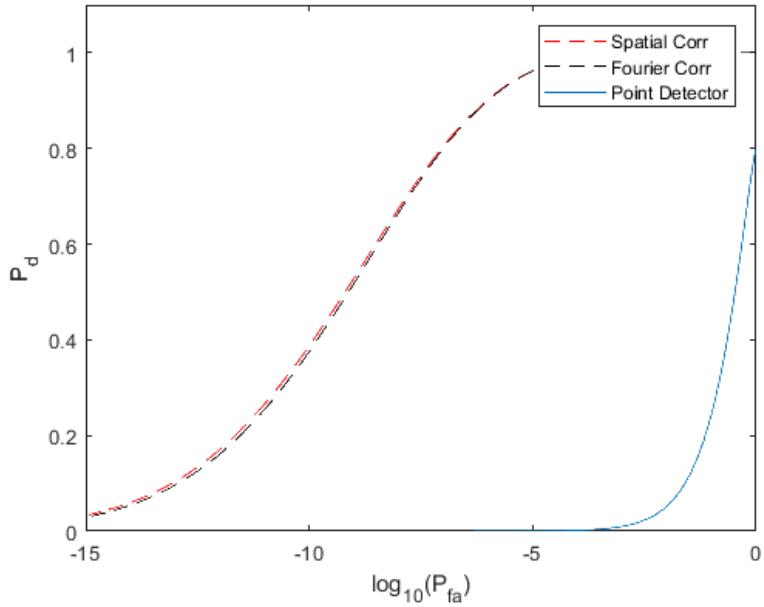

Figure 22. LROC curve using spatial correlator SNR 6 data for each of the three algorithms.

and spatial correlation algorithm each achieved a 40-50% increase in the probability of detection at the 10^{-9} false alarm rate using both sets of data.

Although the Fourier point detector did not outperform a spatial correlator, it did perform on par with the spatial correlator with less information. Taking the Fourier transform of the data and examining a single pixel point does not require information on the shape of the PSF which is required by the spatial correlator. This is significant in that a PSF is not always known and even if it is known, it may not be accurate. As a telescope slews across the sky, atmospheric conditions will dramatically change which would result in a different PSF. The Fourier point detector works independent of telescope pointing position and the shape of the PSF. If the PSF shape the spatial correlator uses in the detection process is different than the truth, the performance will significantly decrease. To test this, the spatial correlation algorithm was processed again with a PSF that was different than the true PSF. The

modified PSF was simulated to be smaller than the true PSF as shown in Figure 23. The Fourier and spatial algorithms were processed using the same simulated data set as above and the detection performance was plotted using a LROC curve. The results, shown in Figure 24, show that the Fourier point source detector achieves a 34% increase in detection probability at a false alarm rate of 10^{-9} in a scenario where the true PSF shape is not known. The difference in the detection performance will vary based on how off the estimated PSF is from the true shape.

Figure 23. PSFs simulated in MATLAB with two different shapes for use by a spatial correlator. Left side - true PSF. Right side - wrong PSF

3.6 Conclusion

In this chapter, a Fourier point detection algorithm using the real component of the Fourier transform of the spatial data is investigated. The algorithm was developed based on long exposure atmospheric turbulence models that account for turbulence correlation between each frame along with an optical model for the telescope system and the expected received data. Using the models for the data a LRT was designed based on the conditional probabilities of the data under both the hypothesis that an object is in the scene and the hypothesis that no object is in the scene. To test the

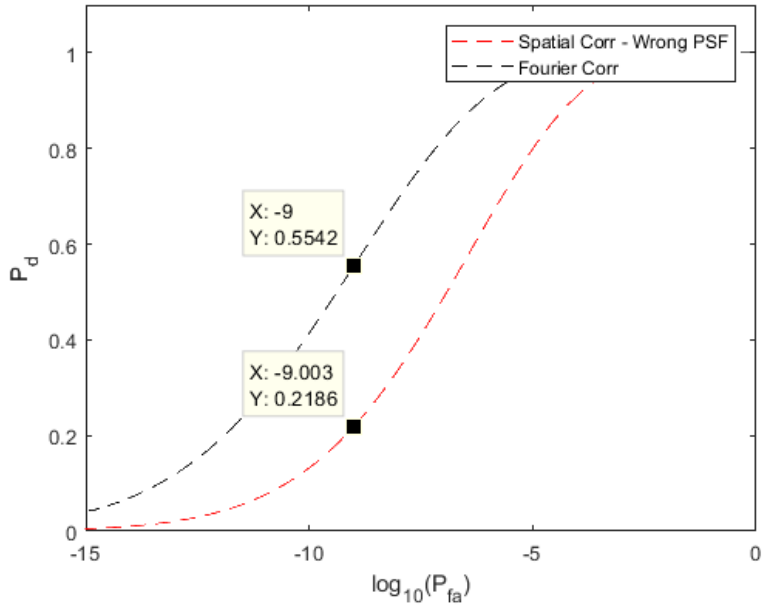

Figure 24. LROC curve comparing performance of Fourier point detector to a spatial correlation algorithm utilizing the wrong PSF shape.

performance of the algorithm, data was simulated in MATLAB and LROC curves were generated based on the statistics of the LRT.

The research in this chapter was focused on image processing in the Fourier domain to increase the probability of detecting unknown space objects. The results from the LROC curve show that the Fourier point detector will significantly outperform a spatial point detector. Additional, it performs nearly the same as the spatial domain correlator. Upon further evaluation, these are the results we would expect due to the nature of the spatial correlator. Specifically, this is because the real component of the Fourier transform of the data is mathematically equivalent to the spatial data which contains only a real signal. This research was focused on exploiting the Fourier domain image to obtain information that would further separate the PDFs under each hypothesis from the spatial domain. Using simulated data at various SNR levels, LROC curve analysis showed a 40-50% increase in the probability of detection at a

false alarm rate of 10^{-9} compared to a traditional point detector.

The algorithm developed in this chapter significantly improved the detection capability over a point detector algorithm like the one utilized by many telescopes within the space community. Just as significant, this algorithm provides the same performance as the spatial correlator but with less information required to operate. An accurate PSF model and shape is not needed to operate the Fourier point detector. This is significant since the PSF is constantly changing and operators don't always have a good understanding of the expected PSF. When comparing the Fourier point detection algorithm to a spatial correlator using an incorrect PSF, the Fourier point detector produced a 34% increase in detection probability. The simplicity of this algorithm allows for the Fourier domain analysis to be implemented in systems that are already working in the Fourier domain without using a spatial domain correlator technique dependent on knowing the exact PSF shape.

IV. Fourier Correlator Algorithm Utilizing Joint Probability Likelihood Ratio Detection

4.1 Introduction

The research in this chapter further explores the potential for detection performance advantages when operating in the Fourier domain of long exposure images of small and/or dim space objects from ground-based telescopes. A binary hypothesis test is developed based on the joint probability distribution function of the image under the hypothesis that an object is present and under the hypothesis that no object exists. The detection algorithm tests each pixel point of the Fourier transformed images to make the determination if an object is present based on the criteria threshold found in the likelihood ratio test. Using simulated data, the performance of the Fourier domain detection algorithm is compared to a spatial correlator used in space object detection applications to evaluate its value.

The Fourier domain correlation algorithm developed in this chapter is a natural extension of the Fourier point source detector examined in Chapter 3 in the same way that a spatial correlator expands on a spatial point source detector. Spatial frequency analysis is not a new area of research as it has been utilized in previous image processing technique. Specifically, imaging in the short exposure regime using post-processing techniques such as speckle imaging reconstruction and lucky imaging [37, 38, 39, 42, 19]. The research in this chapter is focused on purely detection and not directly improving the resolution of the image by expanded and developing a LRT utilizing joint Gaussian probability distribution statistics.

4.2 Data Model

As in Chapter 3, the research in this chapter uses the real component of the Fourier transform of the long exposure spatial images captured by a ground-based optical telescope. There are two hypotheses for modeling the spatial image obtained by the telescope. Under the first hypothesis, H_1, the data contains a distorted point source object along with various noise sources and under the H_0 hypothesis, the data does not contain an object. Preprocessing of the raw telescope data measures and removes the background noise. The first and second order statistical models developed for the data in Chapter 3 are given again below as they are used extensively in the development of the Fourier correlation algorithm in this chapter.

$$\mathrm{E}[d(x,y)|H_0] = B. \tag{4.1}$$

$$\mathrm{E}[d(x,y)|H_1] = \theta h(x,y) + B. \tag{4.2}$$

$$D_r(f_x, f_y) \triangleq \mathrm{Re}\big\{D(f_x, f_y)\big\} = \frac{1}{N}\sum_{x=1}^{N}\sum_{y=1}^{N} d'(x,y)\cos\left(\frac{2\pi}{N}(xf_x + yf_y)\right). \tag{4.3}$$

$$\begin{aligned} \mu_0 &= \mathrm{E}[D_r(f_x, f_y)|H_0] \\ &= 0. \end{aligned} \tag{4.4}$$

$$\begin{aligned} \sigma_0^2 &= \mathrm{E}\big[\big((D_r(f_x, f_y)|H_0) - \mu_0\big)^2\big] \\ &= \frac{B}{2}. \end{aligned} \tag{4.5}$$

$$\begin{aligned}\mu_1 &= \mathrm{E}\big[D_r(f_x, f_y)|H_1\big] \\ &= \theta \mathrm{H}(f_x, f_y).\end{aligned} \tag{4.6}$$

$$\begin{aligned}\sigma_1^2 &= \mathrm{E}\Big[\big(D_r(f_x, f_y)|H_1 - \mu_1\big)^2\Big] \\ &= \frac{\theta}{2N^2} + \frac{B}{2} + \frac{\theta H(2f_x, 2f_y)}{N} + \frac{B}{2N}\delta(2f_x, 2f_y).\end{aligned} \tag{4.7}$$

4.3 Algorithm Development

The Fourier correlation algorithm developed and evaluated in this chapter is based on building a LRT using the conditional joint PDFs of the data under each hypothesis. Working in the spatial domain, each pixel in a spatial image is statistically independent from one another. However, converting to the Fourier domain, the image contains information on the spatial frequency content of the image and doesn't follow the same statistical independence property. To account for the correlation between spatial frequencies, a covariance matrix must be developed to build a conditional joint LRT. Each element of a covariance matrix represents the covariance between two points, m and n. Each element on the diagonal of a covariance matrix relays the variance of the m^{th} spatial frequency.

A covariance matrix, Σ, is generated from the covariance between any two spatial frequency points, D_{r_m} and D_{r_n}, in the image as given in Equation (4.8).

$$
\begin{aligned}
\Sigma_{m,n} &= \operatorname{cov}\Big(D_{r_m} D_{r_n}\Big) \\
&= \mathrm{E}\Big[\Big(D_r(f_{x_m}, f_{y_m}) - \mathrm{E}\big[D_r(f_{x_m}, f_{y_m})\big]\Big)\Big(D_r(f_{x_n}, f_{y_n}) - \mathrm{E}\big[D_r(f_{x_n}, f_{y_n})\big]\Big)\Big] \\
&= \mathrm{E}\Big[D_r(f_{x_m}, f_{y_m}) D_r(f_{x_n}, f_{y_n})\Big] - \mathrm{E}\big[D_r(f_{x_m}, f_{y_m})\big]\mathrm{E}\big[D_r(f_{x_n}, f_{y_n})\big] \\
&= \Gamma_{m,n} - \mathrm{E}\big[D_r(f_{x_m}, f_{y_m})\big]\mathrm{E}\big[D_r(f_{x_n}, f_{y_n})\big].
\end{aligned}
\tag{4.8}
$$

Similarly, the correlation, Γ, between two spatial frequencies is defined as shown in Equation (4.9). This equation utilizes the model for the data as given in Equation (4.3) and is a component in the covariance. To represent that two distinct points are being observed, a change of variables from (x, y) to (u, v) in the second half of this equation is necessary.

$$
\begin{aligned}
\Gamma_{m,n} =& \mathrm{E}\Big[D_r(f_{x_m}, f_{y_m}) D_r(f_{x_n}, f_{y_n})\Big] \\
=& \mathrm{E}\Bigg[\Bigg(\frac{1}{N}\sum_{x=1}^{N}\sum_{y=1}^{N} d'(x,y)\cos\Bigg(\frac{2\pi}{N}(x f_{x_m} + y f_{y_m})\Bigg)\Bigg) \\
& \times \Bigg(\frac{1}{N}\sum_{x=1}^{N}\sum_{y=1}^{N} d'(u,v)\cos\Bigg(\frac{2\pi}{N}(u f_{x_n} + v f_{y_n})\Bigg)\Bigg)\Bigg].
\end{aligned}
\tag{4.9}
$$

Null Hypothesis Statistics.

In this subsection, statistics under the null hypothesis are calculated. This implies that the data, D_r is conditioned on the H_0 hypothesis and has a mean and variance given in Equations (4.4) and (4.5). An analytical derivation of the covariance matrix under the H_0 hypothesis, Σ_0, is evaluated using the standard form for covariance given in Equation (4.8). In order to separate out the work, first the correlation is

calculated using Equation (4.9). In order to evaluate the correlation, there are two cases that must be solved independently. One where the two points are the same, $d(x,y) = d(u,v)$, and when they are different, $d(x,y) \neq d(u,v)$.

CASE 1. $x = u, y = v$

$$\begin{aligned}
\Gamma_{D_{rm}D_{rn}}|H_0 = & \\
&= \mathrm{E}\Bigg[\left(\frac{1}{N}\sum_{x=1}^{N}\sum_{y=1}^{N} d'(x,y)\cos\left(\frac{2\pi}{N}(xf_{x_m} + yf_{y_m})\right)\right) \\
&\quad \times \left(\frac{1}{N}\sum_{u=1}^{N}\sum_{v=1}^{N} d'(u,v)\cos\left(\frac{2\pi}{N}(uf_{x_n} + vf_{y_n})\right)\right)\Bigg]\delta(x-u, y-v) \\
&= \mathrm{E}\left[\frac{1}{N^2}\sum_{x=1}^{N}\sum_{y=1}^{N} d'^2(x,y)\cos\left(\frac{2\pi}{N}(xf_{x_m} + yf_{y_m})\right)\cos\left(\frac{2\pi}{N}(xf_{x_n} + yf_{y_n})\right)\right] \\
&= \frac{1}{N^2}\sum_{x=1}^{N}\sum_{y=1}^{N} \mathrm{E}\left[d'^2(x,y)\right]\cos\left(\frac{2\pi}{N}(xf_{x_m} + yf_{y_m})\right)\cos\left(\frac{2\pi}{N}(xf_{x_n} + yf_{y_n})\right).
\end{aligned} \tag{4.10}$$

The expression can be simplified using Prosthaphaeresis formula given in Equation (4.11) along with a utilization of the Poisson moment theorem in Equation (4.12) [56].

$$\cos\alpha\cos\beta = \frac{\cos(\alpha+\beta) + \cos(\alpha-\beta)}{2}. \tag{4.11}$$

$$\begin{aligned}
\mathrm{E}[d'(x,y)^2|H_0] &= (B^2 + B) - 2B^2 + B^2 \\
&= B.
\end{aligned} \tag{4.12}$$

This results in an expression for the correlation under this first case where the two points are the same.

$$
\begin{aligned}
\Gamma_{D_{r_m} D_{r_n}} | H_0 = & \\
&= \frac{1}{2N^2} \sum_{x=1}^{N} \sum_{y=1}^{N} \mathrm{E}\Big[d'^2(x,y) \Big] \Bigg(\cos\left(\frac{2\pi}{N} (x f_{x_m} + y f_{y_m}) + \frac{2\pi}{N} (x f_{x_n} + y f_{y_n}) \right) \\
&\quad + \cos\left(\frac{2\pi}{N} (x f_{x_m} + y f_{y_m}) - \frac{2\pi}{N} (x f_{x_n} + y f_{y_n}) \right) \Bigg) \\
&= \frac{1}{2N^2} \Bigg[\sum_{x=1}^{N} \sum_{y=1}^{N} B \cos\left(\frac{2\pi}{N} \big(x(f_{x_m} + f_{x_n}) + y(f_{y_m} + f_{y_n}) \big) \right) \\
&\quad + \sum_{x=1}^{N} \sum_{y=1}^{N} B \cos\left(\frac{2\pi}{N} \big(x(f_{x_m} - f_{x_n}) + y(f_{y_m} - f_{y_n}) \big) \right) \Bigg] \\
&= \frac{B}{2N^2} \Bigg[\sum_{x=1}^{N} \sum_{y=1}^{N} \cos\left(\frac{2\pi}{N} \big(x(f_{x_m} + f_{x_n}) + y(f_{y_m} + f_{y_n}) \big) \right) \\
&\quad + \sum_{x=1}^{N} \sum_{y=1}^{N} \cos\left(\frac{2\pi}{N} \big(x(f_{x_m} - f_{x_n}) + y(f_{y_m} - f_{y_n}) \big) \right) \Bigg] \\
&= \frac{B}{2} \delta\big((f_{x_m} + f_{x_n}), (f_{y_m} + f_{y_n}) \big) + \frac{B}{2} \delta\big((f_{x_m} - f_{x_n}), (f_{y_m} - f_{y_n}) \big).
\end{aligned}
\tag{4.13}
$$

Case 2 is slightly easier to solve due to the zero-mean nature of the data under H_0.

CASE 2. $x \neq u, y \neq v$

$$\begin{aligned}
\Gamma_{D_{r_m} D_{r_n}} | H_0 =& \mathrm{E}\Bigg[\left(\frac{1}{N}\sum_{x=1}^{N}\sum_{y=1}^{N} d'(x,y)\cos\left(\frac{2\pi}{N}(xf_{x_m}+yf_{y_m})\right)\right) \\
&\times\left(\frac{1}{N}\sum_{u=1}^{N}\sum_{v=1}^{N} d'(u,v)\cos\left(\frac{2\pi}{N}(uf_{x_n}+vf_{y_n})\right)\right)\Bigg](1-\delta(x-u,y-v)) \\
=& \mathrm{E}\Bigg[\frac{1}{N^2}\sum_{x=1}^{N}\sum_{y=1}^{N}\sum_{u=1}^{N}\sum_{v=1}^{N} d'(x,y)d'(u,v)\cos\left(\frac{2\pi}{N}(xf_{x_m}+yf_{y_m})\right) \\
&\times\cos\left(\frac{2\pi}{N}(uf_{x_n}+vf_{y_n})\right)\Bigg](1-\delta(x-u,y-v)) \\
=& \frac{1}{N^2}\sum_{x=1}^{N}\sum_{y=1}^{N}\sum_{u=1}^{N}\sum_{v=1}^{N} \mathrm{E}\Big[d'(x,y)\Big]\mathrm{E}\Big[d'(u,v)\Big]\cos\left(\frac{2\pi}{N}(xf_{x_m}+yf_{y_m})\right) \\
&\times\cos\left(\frac{2\pi}{N}(uf_{x_n}+vf_{y_n})\right)\Bigg](1-\delta(x-u,y-v)) \\
=& 0.
\end{aligned} \tag{4.14}$$

The results from the two cases (results in Equations (4.13) and (4.14)) are combined to give an expression for the correlation between two points.

$$\Gamma_{D_{r_m} D_{r_n}} | H_0 = \frac{B}{2}\delta\big(f_{x_m}+f_{x_n}, f_{y_m}+f_{y_n}\big) + \frac{B}{2}\delta\big(f_{x_m}-f_{x_n}, f_{y_m}-f_{y_n}\big). \tag{4.15}$$

The covariance can then be calculated using Equation (4.8). Since the mean of the data under this hypothesis is zero, the covariance is equal to the correlation. Due to the long exposure nature of the data and that the real component of the Fourier transform was taken, the data will be symmetric. Thus, only the positive frequencies are considered in processing the data with the algorithm. With only positive frequencies, the first Dirac function will always be zero unless all spatial

frequencies, $f_{x_m}, f_{x_n}, f_{y_m}, f_{y_n}$, are equal to zero.

$$\begin{aligned}\Sigma_{m,n}|H_0 &= \Gamma_{D_{r_m}D_{r_n}}|H_0 - \mathrm{E}\Big[D_r(f_{x_m}, f_{y_m})\Big]\mathrm{E}\Big[D_r(f_{x_n}, f_{y_n}\Big] \\ &= \frac{B}{2}\delta\big(f_{x_m} + f_{x_n}, f_{y_m} + f_{y_n}\big) + \frac{B}{2}\delta\big(f_{x_m} - f_{x_n}, f_{y_m} - f_{y_n}\big).\end{aligned} \tag{4.16}$$

Alternative Hypothesis Statistics.

Similar to the previous subsection, statistics under the alternative hypothesis are calculated in this subsection. This implies that the data, D_r is conditioned on the H_1 hypothesis and has a mean and variance given in Equations (4.6) and (4.7). The steps in deriving the statistics are the same but more difficult in this subsection due to the non-zero nature of the mean. As before, when calculating the correlation, there are two cases that must be solved independently. One where the two points are the same, $d(x,y) = d(u,v)$, and when they are different, $d(x,y) \neq d(u,v)$.

Under the H_1 hypothesis, the following equations are used in evaluating the correlation.

$$\begin{aligned}\mathrm{E}[(d'(x,y)|H_1)^2] &= \mathrm{E}\big[\big(d(x,y)|H_1 - B\big)^2\big] \\ &= \mathrm{E}\big[(d(x,y)|H_1)^2 - 2B(d(x,y)|H_1) + B^2\big].\end{aligned} \tag{4.17}$$

The Poisson moment theorem along with the model for the data in Equation (4.2) can be used to simplify this expression.

$$\begin{aligned}\mathrm{E}[(d'(x,y)|H_1)^2] =& (\theta h(x,y) + B)^2 + (\theta h(x,y) + B) - 2B(\theta h(x,y) + B) + B^2 \\ =& \theta^2 h^2(x,y) + 2B\theta h(x,y) + B^2 + \theta h(x,y) + B - 2B\theta h(x,y) \\ & - 2B^2 + B^2 \\ =& \theta^2 h^2(x,y) + \theta h(x,y) + B.\end{aligned} \tag{4.18}$$

CASE 1. $x = u, y = v$

$$\begin{aligned}
\Gamma_{D_{r_m} D_{r_n}}|H_1 =& \mathrm{E}\Bigg[\left(\frac{1}{N}\sum_{x=1}^{N}\sum_{y=1}^{N} d'(x,y)\cos\left(\frac{2\pi}{N}(xf_{x_m}+yf_{y_m})\right)\right) \\
&\times\left(\frac{1}{N}\sum_{u=1}^{N}\sum_{v=1}^{N} d'(u,v)\cos\left(\frac{2\pi}{N}(uf_{x_n}+vf_{y_n})\right)\right)\Bigg]\delta(x-u,y-v) \\
=& \mathrm{E}\Bigg[\left(\frac{1}{N}\sum_{x=1}^{N}\sum_{y=1}^{N} d'(x,y)\cos\left(\frac{2\pi}{N}(xf_{x_m}+yf_{y_m})\right)\right) \\
&\times\left(\frac{1}{N}\sum_{x=1}^{N}\sum_{y=1}^{N} d'(x,y)\cos\left(\frac{2\pi}{N}(xf_{x_n}+yf_{y_n})\right)\right)\Bigg] \\
=& \frac{1}{N^2}\sum_{x=1}^{N}\sum_{y=1}^{N}\mathrm{E}\Big[d'^2(x,y)\Big]\cos\left(\frac{2\pi}{N}(xf_{x_m}+yf_{y_m})\right) \\
&\times\cos\left(\frac{2\pi}{N}(xf_{x_n}+yf_{y_n})\right) \\
=& \frac{1}{2N^2}\sum_{x=1}^{N}\sum_{y=1}^{N}\mathrm{E}\Big[d'^2(x,y)\Big]\left(\cos\left(\frac{2\pi}{N}\big(x(f_{x_m}+f_{x_n})+y(f_{y_m}+f_{y_n})\big)\right)\right. \\
&\left.+\cos\left(\frac{2\pi}{N}\big(x(f_{x_m}-f_{x_n})+y(f_{y_m}-f_{y_n})\big)\right)\right).
\end{aligned} \tag{4.19}$$

The expected value of the square of the background-removed data was previously calculated using the Poisson moment theorem in Equation (4.18). This result is substituted into the expression to give,

$$\begin{aligned}
\Gamma_{D_{r_m} D_{r_n}}|H_1 =& \frac{1}{2N^2}\sum_{x=1}^{N}\sum_{y=1}^{N}(\theta^2h^2(x,y)+\theta h(x,y)+B) \\
&\times\cos\left(\frac{2\pi}{N}\big(x(f_{x_m}+f_{x_n})+y(f_{y_m}+f_{y_n})\big)\right) \\
&+\frac{1}{2N^2}\sum_{x=1}^{N}\sum_{y=1}^{N}(\theta^2h^2(x,y)+\theta h(x,y)+B) \\
&\times\cos\left(\frac{2\pi}{N}\big(x(f_{x_m}-f_{x_n})+y(f_{y_m}-f_{y_n})\big)\right).
\end{aligned} \tag{4.20}$$

Expanding the expression out shows that it is a series of Fourier transforms and Diracs,

$$\begin{aligned}
\Gamma_{D_{r_m}D_{r_n}}|H_1 =& \frac{1}{2N^2}\sum_{x=1}^{N}\sum_{y=1}^{N}\theta^2 h^2(x,y)\cos\left(\frac{2\pi}{N}\big(x(f_{x_m}+f_{x_n})+y(f_{y_m}+f_{y_n})\big)\right) \\
&+\frac{1}{2N^2}\sum_{x=1}^{N}\sum_{y=1}^{N}\theta h(x,y)\cos\left(\frac{2\pi}{N}\big(x(f_{x_m}+f_{x_n})+y(f_{y_m}+f_{y_n})\big)\right) \\
&+\frac{1}{2N^2}\sum_{x=1}^{N}\sum_{y=1}^{N}B\cos\left(\frac{2\pi}{N}\big(x(f_{x_m}+f_{x_n})+y(f_{y_m}+f_{y_n})\big)\right) \\
&+\frac{1}{2N^2}\sum_{x=1}^{N}\sum_{y=1}^{N}\theta^2 h^2(x,y)\cos\left(\frac{2\pi}{N}\big(x(f_{x_m}-f_{x_n})+y(f_{y_m}-f_{y_n})\big)\right) \\
&+\frac{1}{2N^2}\sum_{x=1}^{N}\sum_{y=1}^{N}\theta h(x,y)\cos\left(\frac{2\pi}{N}\big(x(f_{x_m}-f_{x_n})+y(f_{y_m}-f_{y_n})\big)\right) \\
&+\frac{1}{2N^2}\sum_{x=1}^{N}\sum_{y=1}^{N}B\cos\left(\frac{2\pi}{N}\big(x(f_{x_m}-f_{x_n})+y(f_{y_m}-f_{y_n})\big)\right) \\
=& \frac{\theta^2}{2N}\mathcal{F}[h^2(x,y)|(f_{x_m}+f_{x_n},f_{y_m}+f_{y_n})]+\frac{\theta}{2N}H(f_{x_m}+f_{x_n},f_{y_m}+f_{y_n}) \\
&+\frac{B}{2}\delta(f_{x_m}+f_{x_n},f_{y_m}+f_{y_n})+\frac{\theta^2}{2N}\mathcal{F}[h^2(x,y)|(f_{x_m}-f_{x_n},f_{y_m}-f_{y_n})] \\
&+\frac{\theta}{2N}H(f_{x_m}-f_{x_n},f_{y_m}-f_{y_n})+\frac{B}{2}\delta(f_{x_m}-f_{x_n},f_{y_m}-f_{y_n}).
\end{aligned} \tag{4.21}$$

CASE 2. $x \neq u, y \neq v$

$$
\begin{aligned}
\Gamma_{D_{r_m} D_{r_n}} | H_1 =& \mathrm{E}\Bigg[\bigg(\frac{1}{N}\sum_{x=1}^{N}\sum_{y=1}^{N} d'(x,y)\cos\big(\frac{2\pi}{N}(xf_{x_m}+yf_{y_m})\big)\bigg) \\
&\times\bigg(\frac{1}{N}\sum_{u=1}^{N}\sum_{v=1}^{N} d'(u,v)\cos\big(\frac{2\pi}{N}(uf_{x_n}+vf_{y_n})\big)\bigg)\Bigg]\big(1-\delta(x-u,y-v)\big) \\
=&\frac{1}{N^2}\sum_{x=1}^{N}\sum_{y=1}^{N}\sum_{u=1}^{N}\sum_{v=1}^{N}\mathrm{E}\Big[d'(x,y)\Big]\mathrm{E}\Big[d'(u,v)\Big]\cos\big(\frac{2\pi}{N}(xf_{x_m}+yf_{y_m})\big) \\
&\times\cos\big(\frac{2\pi}{N}(uf_{x_n}+vf_{y_n})\big)\big(1-\delta(x-u,y-v)\big) \\
=&\frac{\theta^2}{N^2}\sum_{x=1}^{N}\sum_{y=1}^{N}\sum_{u=1}^{N}\sum_{v=1}^{N}h(x,y)h(u,v)\cos\big(\frac{2\pi}{N}(xf_{x_m}+yf_{y_m})\big) \\
&\times\cos\big(\frac{2\pi}{N}(uf_{x_n}+vf_{y_n})\big)\big(1-\delta(x-u,y-v)\big) \\
=&\frac{\theta^2}{N^2}\sum_{x=1}^{N}\sum_{y=1}^{N}\sum_{u=1}^{N}\sum_{v=1}^{N}h(x,y)h(u,v)\cos\big(\frac{2\pi}{N}(xf_{x_m}+yf_{y_m})\big) \\
&\times\cos\big(\frac{2\pi}{N}(uf_{x_n}+vf_{y_n})\big)-\frac{\theta^2}{N^2}\sum_{x=1}^{N}\sum_{y=1}^{N}\sum_{u=1}^{N}\sum_{v=1}^{N}h(x,y)h(u,v) \\
&\times\cos\big(\frac{2\pi}{N}(xf_{x_m}+yf_{y_m})\big)\cos\big(\frac{2\pi}{N}(uf_{x_n}+vf_{y_n})\big)\delta(x-u,y-v) \\
=&\frac{\theta^2}{N^2}\sum_{x=1}^{N}\sum_{y=1}^{N}h(x,y)\cos\big(\frac{2\pi}{N}(xf_{x_m}+yf_{y_m})\big)\sum_{u=1}^{N}\sum_{v=1}^{N}h(u,v) \\
&\times\cos\big(\frac{2\pi}{N}(uf_{x_n}+vf_{y_n})\big)-\frac{\theta^2}{N^2}\sum_{x=1}^{N}\sum_{y=1}^{N}h^2(x,y)\cos\big(\frac{2\pi}{N}(xf_{x_m}+yf_{y_m})\big) \\
&\times\cos\big(\frac{2\pi}{N}(xf_{x_n}+yf_{y_n})\big) \\
=&\theta^2 H(f_{x_m},f_{y_m})H(f_{x_n},f_{y_n})-\frac{\theta^2}{2N^2}\sum_{x=1}^{N}\sum_{y=1}^{N}h^2(x,y)\Bigg(\cos\bigg(\frac{2\pi}{N}\big(x(f_{x_m} \\
&+f_{x_n})+y(f_{y_m}+f_{y_n})\big)\bigg)+\cos\bigg(\frac{2\pi}{N}\big(x(f_{x_m}-f_{x_n})+y(f_{y_m}-f_{y_n})\big)\bigg)\Bigg) \\
=&\theta^2 H(f_{x_m},f_{y_m})H(f_{x_n},f_{y_n})-\frac{\theta^2}{2N}\Big(\mathcal{F}[h^2(x,y)|(f_{x_m}+f_{x_n},f_{y_m}+f_{y_n})] \\
&+\mathcal{F}[h^2(x,y)|(f_{x_m}-f_{x_n},f_{y_m}-f_{y_n})]\Big).
\end{aligned}
\tag{4.22}
$$

Adding the results from the two cases (Equations (4.21) and (4.22)) together gives the complete expression for the correlation between two spatial frequencies under the H_1 hypothesis.

$$\begin{aligned}
\Gamma_{D_{r_m}D_{r_n}}|H_1 =& \frac{\theta^2}{2N}\mathcal{F}[h^2(x,y)|(f_{x_m}+f_{x_n},f_{y_m}+f_{y_n})] + \frac{\theta}{2N}H(f_{x_m}+f_{x_n},f_{y_m}+f_{y_n}) \\
&+ \frac{B}{2}\delta(f_{x_m}+f_{x_n},f_{y_m}+f_{y_n}) + \frac{\theta^2}{2N}\mathcal{F}[h^2(x,y)|(f_{x_m}-f_{x_n},f_{y_m}-f_{y_n})] \\
&+ \frac{\theta}{2N}H(f_{x_m}-f_{x_n},f_{y_m}-f_{y_n}) + \frac{B}{2}\delta(f_{x_m}-f_{x_n},f_{y_m}-f_{y_n}) \\
&+ \theta^2 H(f_{x_m},f_{y_m})H(f_{x_n},f_{y_n}) \\
&- \frac{\theta^2}{2N}\Big(\mathcal{F}[h^2(x,y)|(f_{x_m}+f_{x_n},f_{y_m}+f_{y_n})] \\
&+ \mathcal{F}[h^2(x,y)|(f_{x_m}-f_{x_n},f_{y_m}-f_{y_n})]\Big) \\
=& \theta^2 H(f_{x_m},f_{y_m})H(f_{x_n},f_{y_n}) + \frac{\theta}{2N}H(f_{x_m}+f_{x_n},f_{y_m}+f_{y_n}) \\
&+ \frac{\theta}{2N}H(f_{x_m}-f_{x_n},f_{y_m}-f_{y_n}) \\
&+ \frac{B}{2}\delta(f_{x_m}+f_{x_n},f_{y_m}+f_{y_n}) + \frac{B}{2}\delta(f_{x_m}-f_{x_n},f_{y_m}-f_{y_n}).
\end{aligned} \tag{4.23}$$

The covariance can then be calculated using Equation (4.8) and the correlation results. This result differs from the H_0 hypothesis since the mean is nonzero under H_1. Like the H_0 case, with only positive frequencies, the first Dirac function will

always be zero unless $f_{x_m}, f_{x_n}, f_{y_m} + f_{y_n}$ are all equal to zero.

$$\begin{aligned}
\Sigma_{m,n}|H_1 =& \Gamma_{D_{r_m} D_{r_n}}|H_1 - \mathrm{E}\Big[D_r(f_{x_m}, f_{y_m})\Big]\mathrm{E}\Big[D_r(f_{x_n}, f_{y_n}\Big] \\
=& \theta^2 H(f_{x_m}, f_{y_m})H(f_{x_n}, f_{y_n}) + \frac{\theta}{2N}H(f_{x_m} + f_{x_n}, f_{y_m} + f_{y_n}) \\
&+ \frac{\theta}{2N}H(f_{x_m} - f_{x_n}, f_{y_m} - f_{y_n}) + \frac{B}{2}\delta(f_{x_m} + f_{x_n}, f_{y_m} + f_{y_n}) \\
&+ \frac{B}{2}\delta(f_{x_m} - f_{x_n}, f_{y_m} - f_{y_n}) - \theta^2 H(f_{x_m}, f_{y_m})H(f_{x_n}, f_{y_n}) \\
=& \frac{\theta}{2N}H(f_{x_m} + f_{x_n}, f_{y_m} + f_{y_n}) + \frac{\theta}{2N}H(f_{x_m} - f_{x_n}, f_{y_m} - f_{y_n}) \\
&+ \frac{B}{2}\delta(f_{x_m} + f_{x_n}, f_{y_m} + f_{y_n}) + \frac{B}{2}\delta(f_{x_m} - f_{x_n}, f_{y_m} - f_{y_n}).
\end{aligned} \tag{4.24}$$

Likelihood Ratio Test.

Due to the off-diagonal covariance between frequencies, the joint probability is not the sum of the individual probabilities. The joint probability will follow a multivariate Gaussian distribution given as

$$P(D_r|H_k) = \frac{1}{(2\pi)^{(\frac{N^2}{2})}|\mathbf{\Sigma_k}|^{(\frac{1}{2})}} \exp\left\{ -\frac{1}{2}(D_r - \mu_k)^T \mathbf{\Sigma_k}^{-1}(D_r - \mu_k)\right\}. \tag{4.25}$$

The random variable image data, $D_r|H_k$, is a N^2 x 1 vector of the real component of the Fourier transformed and background-removed data. The covariance matrix, Σ_k, is size N^2 x N^2 and represent the covariance matrix for each hypothesis from Equations (4.16) and (4.24). The determinant of the covariance matrix, $|\Sigma_k|$, is a 1 x 1. The mean, μ_k, are N^2 x 1 vectors representing the mean of the conditional data at each spatial frequency pair f_x, f_y.

The ratio of the two joint conditional probabilities is taken to develop a LRT, Λ, which is compared to 1. When the ratio is greater than one, H_1 case is true and when

less than one, H_0 case is true. The ratio is defined as

$$\Lambda = \frac{P(D_r|H_1)}{P(D_r|H_0)} \underset{H_0}{\overset{H_1}{\gtrless}} 1. \tag{4.26}$$

Combining Equations (4.25) and (4.26) results in the following

$$\begin{aligned}\Lambda &= \frac{\frac{1}{(2\pi)^{(\frac{N^2}{2})}|\mathbf{\Sigma_1}|^{(\frac{1}{2})}} \exp\left\{ -\frac{1}{2}(D_r-\mu_1)^T {\mathbf{\Sigma_1}}^{-1}(D_r-\mu_1)\right\}}{\frac{1}{(2\pi)^{(\frac{N^2}{2})}|\mathbf{\Sigma_0}|^{(\frac{1}{2})}} \exp\left\{ -\frac{1}{2}(D_r-\mu_0)^T {\mathbf{\Sigma_0}}^{-1}(D_r-\mu_0)\right\}} \underset{H_0}{\overset{H_1}{\gtrless}} 1 \\ &= \frac{|\mathbf{\Sigma_0}|^{(\frac{1}{2})} \exp\left\{ -\frac{1}{2}(D_r-\mu_1)^T {\mathbf{\Sigma_1}}^{-1}(D_r-\mu_1)\right\}}{|\mathbf{\Sigma_1}|^{(\frac{1}{2})} \exp\left\{ -\frac{1}{2}(D_r-\mu_0)^T {\mathbf{\Sigma_0}}^{-1}(D_r-\mu_0)\right\}} \underset{H_0}{\overset{H_1}{\gtrless}} 1.\end{aligned} \tag{4.27}$$

The LRT can be simplified by taking the natural log of both sides of the LRT equation to obtain a Log-Likelihood Ratio Test (LLRT),

$$\ln\left(\frac{|\mathbf{\Sigma_0}|^{(\frac{1}{2})}}{|\mathbf{\Sigma_1}|^{(\frac{1}{2})}}\right) - \frac{1}{2}(D_r-\mu_1)^T {\mathbf{\Sigma_1}}^{-1}(D_r-\mu_1) + \frac{1}{2}(D_r-\mu_0)^T {\mathbf{\Sigma_0}}^{-1}(D_r-\mu_0) \underset{H_0}{\overset{H_1}{\gtrless}} 0. \tag{4.28}$$

This expression can be further simplified down to the expression shown in Equation (4.29) by expanding out the matrix multiplications, substituting the means and further combining terms. None of the terms on the right side are data dependent and would only act as offsets to a threshold so it has been replaced with τ to represent the threshold since specific threshold values are not needed to evaluate the algorithms performance.

$$-{D_r}^T\mathbf{\Sigma_1^{-1}}D_r + {D_r}^T\mathbf{\Sigma_0^{-1}}D_r + 2(\theta H)^T\mathbf{\Sigma_1^{-1}}D_r \underset{H_0}{\overset{H_1}{\gtrless}} (\theta H)^T\mathbf{\Sigma_1^{-1}}(\theta H) - 2\ln\left(\frac{|\mathbf{\Sigma_0}|^{(\frac{1}{2})}}{|\mathbf{\Sigma_1}|^{(\frac{1}{2})}}\right) \equiv \tau. \tag{4.29}$$

The Fourier LRT in this form represents some challenges that must be solved before it could be implemented using measured data. The first issue is the need to

know the target intensity, θ, if an object was in the image. In a detection scenario this value will not be known and estimating it from the data will be difficult since the algorithm would have to estimate the intensity when an object was not in the scene as well. A similar challenge exists in developing each of the covariance matrices since both also have dependence on the target intensity. Additionally, the OTF, H, cannot be separated from the data and must be known.

The Fourier correlation LRT investigated further in this research is going to take components of the complete Fourier LRT derived above to simplify the test and remove the dependency on θ. This modified approach is shown in Equation (4.30). The modified Fourier correlation algorithm utilizes the covariance matrix along with the Fourier transformed data to build a LRT and make a detection decision. The second term of the Fourier LRT is simply a representation of the spatial correlator in the frequency domain. Thus, this LRT is taking the data derived by the spatial correlator using a Fourier transform and including additional information on the correlation between the received image and the expected image if an object was in the scene.

$$H^T \mathbf{\Sigma_1^{-1}} D_r + H^T \mathbf{\Sigma_0^{-1}} D_r \underset{H_0}{\overset{H_1}{\gtrless}} \tau. \tag{4.30}$$

4.4 Simulated Data

Dim space object data was simulated in MATLAB to test the performance of the Fourier correlation algorithm compared to the matched filter algorithm. The MATLAB simulation allows access to accurately distributed and realistic looking data while removing unknowns in the scenarios. Under the H_1 hypothesis, the intensity of the object can be varied to test the algorithm at various SNR levels and data under the H_0 hypothesis can be simulated by setting the intensity to zero. The simulation

will develop data with accurate long exposure PSF statistics and utilizing built in Poisson random variable functions to simulate the statistics of the background noise.

The simulation was set up for two different scenarios using the parameters shown in Table 3. The first and third scenarios have slightly worse seeing conditions with a r_0 value of 5 cm compared to scenario two which was simulated with a r_0 value of 8 cm. The object intensity level was adjusted in each scenario to simulate a SNR six object which has a P_D of approximately 0.5 when the P_{FA} is at 10^{-9} using the spatial correlator.

Table 3. Parameters used to create simulated data in MATLAB.

Parameter	**Scenario 1**	**Scenario 2**	**Scenario 3**
Aperture Diameter, D (m)	0.25	0.25	0.25
Fried Parameter, r_0 (cm)	5.0	8.0	5.0
Object Intensity, θ (photons)	1,050	700	700
Background, B (photons)	100	100	100
Window Size, N (pixels)	32	32	32
Number of Frames	100,000	100,000	100,000

Examples of simulated data from the first scenario are shown in Figure 25 which illustrates one frame of simulated spatial and Fourier transformed data obtained from the optical system under each of the hypothesis for the first scenario. The long exposure PSF used to generate the data was created by averaging 100 correlated short exposure PSFs generated using a statistically accurate atmospheric turbulence generation approach developed by Putnam [52].

Examples of the simulated data under the better seeing conditions of scenario two are shown in Figure 26. Only the H_1 data was shown in the figure since the H_0 data is just noise and will look similar to scenario one since the atmospheric seeing conditions doesn't affect the data when there is no object to image. Under the dimmer object scenario, the simulated data is shown in Figure 27.

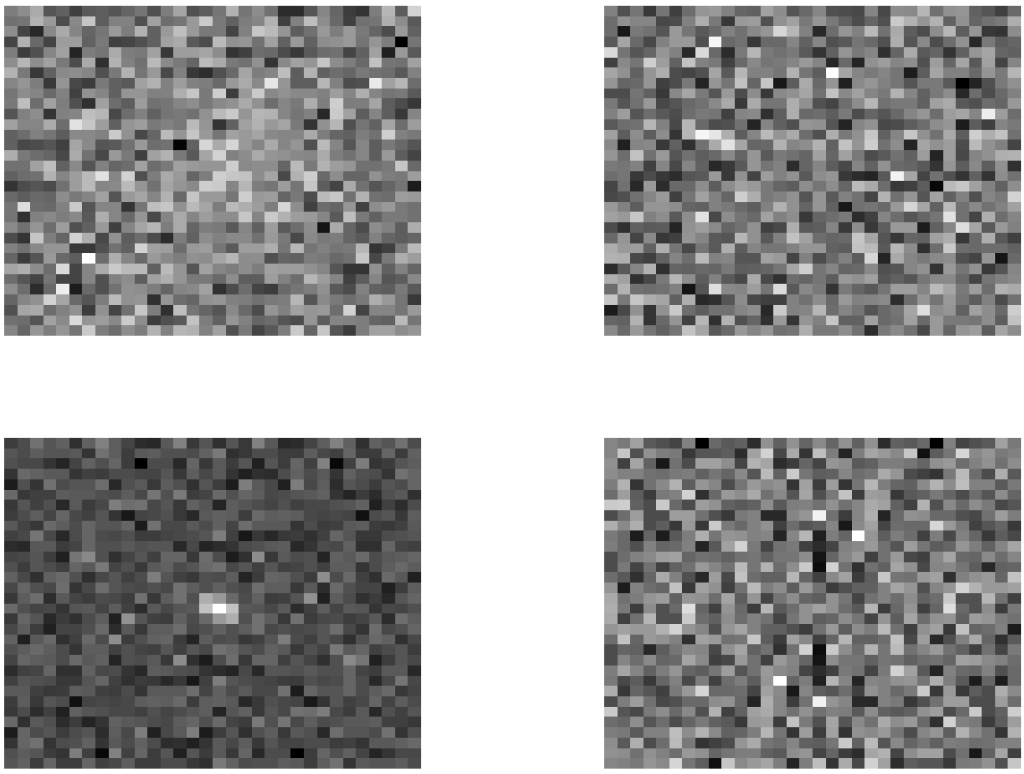

Figure 25. Scenario 1: Simulated H_1 data (left side). Simulated H_0 data (right side). Spatial data (top row). Real component of the Fourier transform of the data (bottom row).

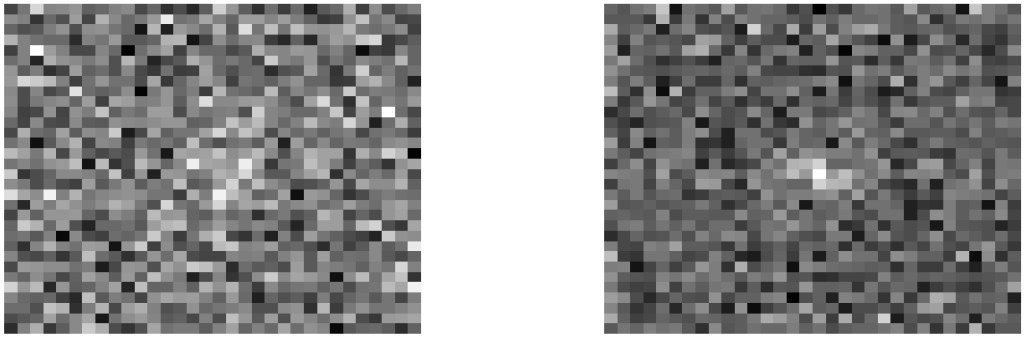

Figure 26. Scenario 2: Simulated H_1 spatial data (left side). Simulated H_1 Fourier data (right side).

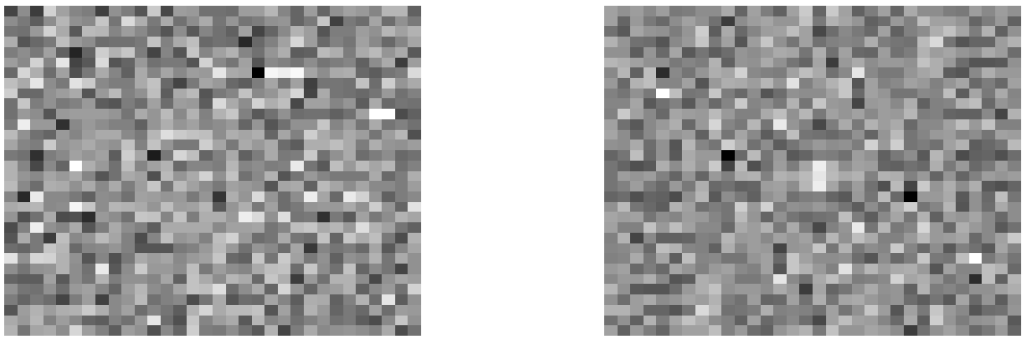

Figure 27. Scenario 3: Simulated H_1 spatial data (left side). Simulated H_0 Fourier data (right side).

4.5 Results & Analysis

The simulated data was used to evaluate the performance of the Fourier LRT against the spatial correlator utilizing a LROC curve. As described in Section 2.3, a LROC curve allows the performance to be evaluated without setting a specific threshold value across different algorithms. This showcases the performance of contrasting algorithms at difference detection and false alarm rates.

To build a LROC curve, the statistics of the LLRT must be examined. The LLRT values under each scenario are shown in Figures 28, 29 and 30. These figures plot the calculated value from the LLRT based on the data from each scenario. These mean and variance statistics from these values are used to generate the LROC curves. Plotting the PDF of the likelihood ratio values is another platform to visualize the difference in the two algorithms. Using a histogram plot, the distribution for each hypothesis and scenario are shown in Figures 31, 32 and 33. As the separation between the H_1 and H_0 distributions increase, the probability of detection increases and false positives decreases.

The LROC curves for the three scenarios are shown in Figures 34, 35 and 36.

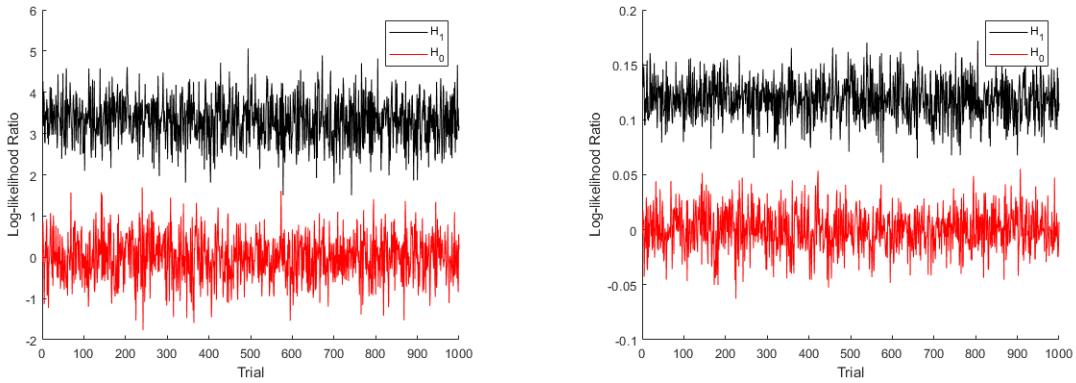

Figure 28. Scenario 1: Spatial correlation LLRT values in each simulated frame (left side). Fourier correlation LLRT values in each simulated frame (left side).

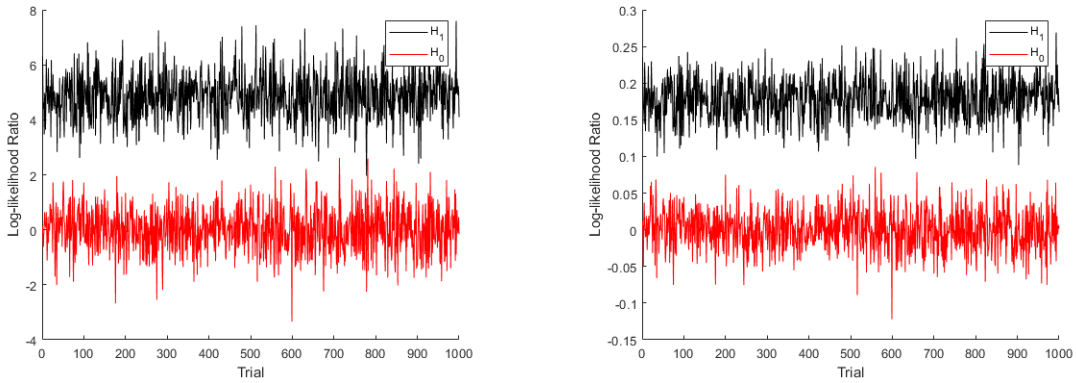

Figure 29. Scenario 2: Spatial correlation LLRT values in each simulated frame (left side). Fourier correlation LLRT values in each simulated frame (right side).

Under both scenarios one and two, a 23% increase in the P_D at a P_{FA} of 10^{-9} is achieved by the Fourier correlator. Under the dimmer object scenario, there was an 11% increase in detection probability when a spatial correlator had a 50% chance of detection. This increase is accomplished through accounting for correlations in the frequency domain. In each of these plots, a 95% confidence interval bound was plotted for each algorithm. The upper bound was plotted for the lower performing algorithm and a lower bound was plotted for the higher performing bound. Each of these plots show that at a 95% confidence the Fourier correlator algorithm achieves

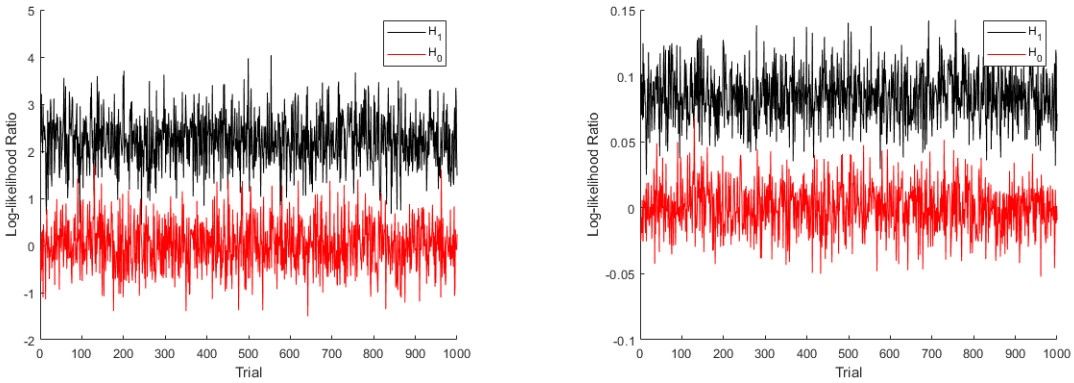

Figure 30. Scenario 3: Spatial correlation LLRT values in each simulated frame (left side). Fourier correlation LLRT values in each simulated frame (right side).

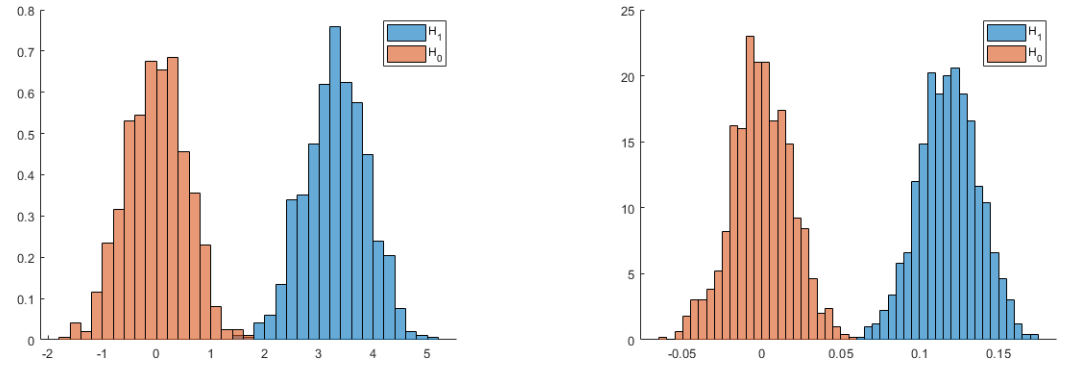

Figure 31. Scenario 1: Spatial correlation PDF showing separation between H_1 and H_0 (left side). Fourier correlation PDF showing separation between H_1 and H_0 (right side).

a higher probability of detection than a spatial correlation algorithm at a false alarm rate of10^{-9}.

To run this algorithm, the theoretical covariance matrix in Equations (4.16) and (4.24) were not utilized. The covariance matrix used by the Fourier LRT was calculated from the data sample set. This is not the ideal scenario since it would prohibit real time processing of data but this technique could be utilized to build a covariance matrix based on the entire set of data in a post-processing detection process. How-

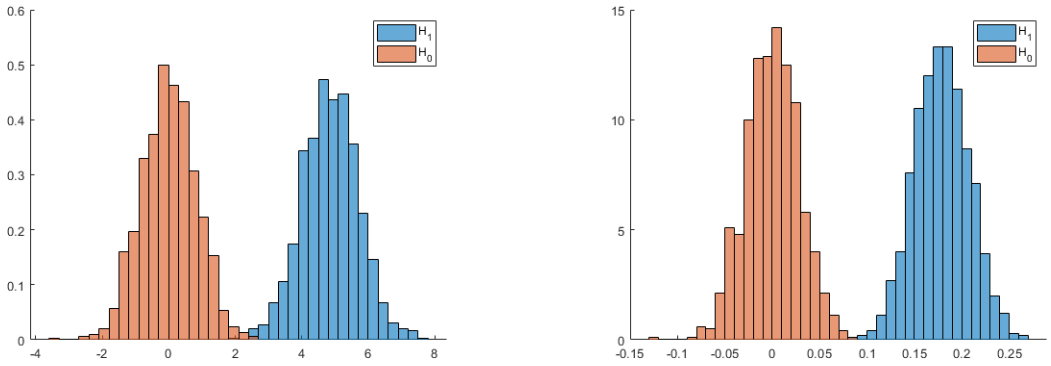

Figure 32. Scenario 2: Spatial correlation PDF showing separation between H_1 and H_0 (left side). Fourier correlation PDF showing separation between H_1 and H_0 (right side).

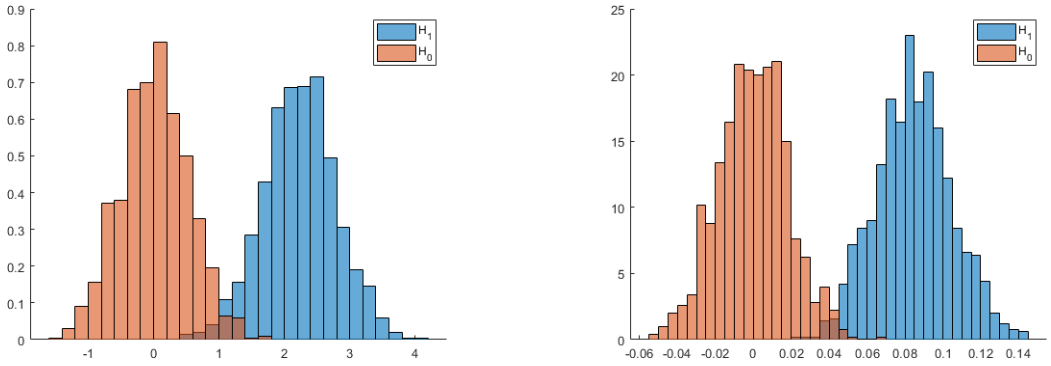

Figure 33. Scenario 3: Spatial correlation PDF showing separation between H_1 and H_0 (left side). Fourier correlation PDF showing separation between H_1 and H_0 (right side).

ever, the algorithm processes the data for detection the same under both hypotheses. There is no built-in bias to the post processing scheme that categorizes the data and allows it to be processed differently.

The results show that when using long exposure data, the Fourier LRT achieves a significant increase in the detection probability at realistic false alarm rates using the modified Fourier LRT compared to the matched filter approach. Both techniques assume that the background level is known along with knowing the atmospheric seeing

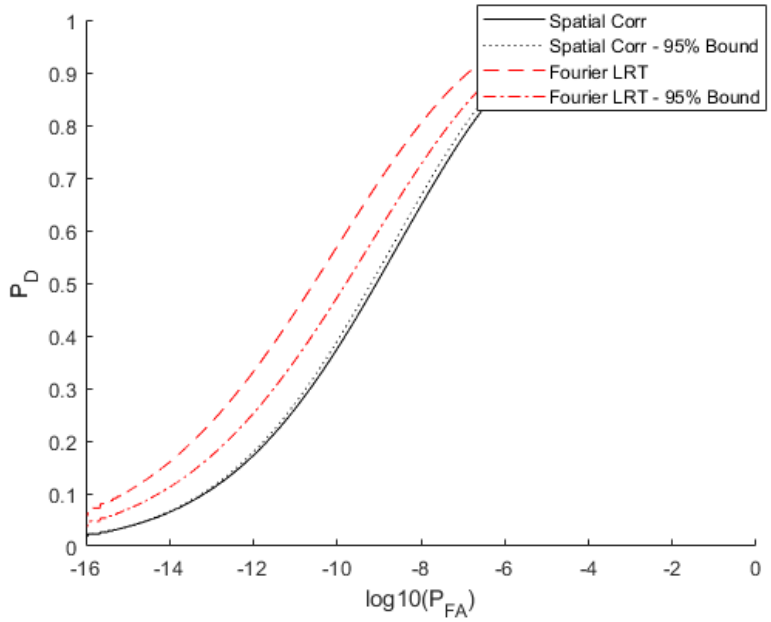

Figure 34. Scenario 1: LROC curve comparing the detection and false alarm rates between a spatial correlation and Fourier correlation techniques.

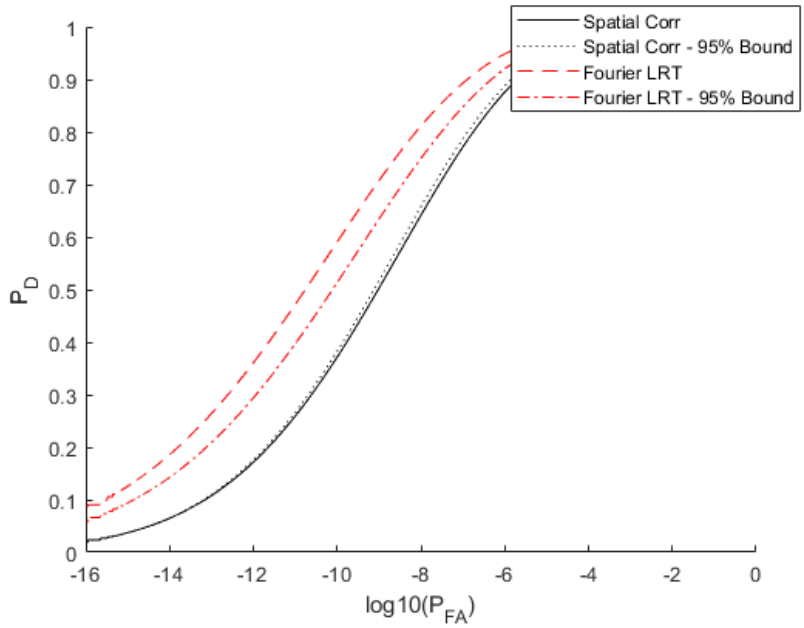

Figure 35. Scenario 2: LROC curve comparing the detection and false alarm rates between a spatial correlation and Fourier correlation techniques.

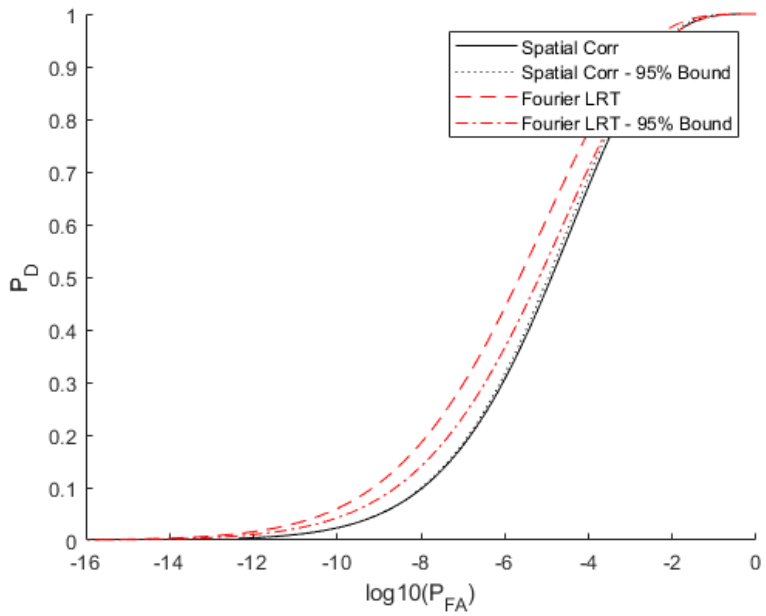

Figure 36. Scenario 3: LROC curve comparing the detection and false alarm rates between spatial correlation and Fourier correlation techniques.

conditions to develop a long exposure PSF. The modified Fourier LRT approach used in this chapter did not depend on knowing the target intensity but did assume the covariance matrix could be calculated from the data when an object was present. This requires the algorithm to operate in a post-processing format and to potentially collect additional data knowing an object was present to generate the covariance matrix.

4.6 Conclusion

The goal of the research in this chapter was to improve the detection probability of dim space objects for a given false alarm rate. The method proposed in this chapter was based on utilizing current techniques for gathering long exposure images taken with a ground-based telescope and altering the post-processing algorithm used for detection. In detection scenarios, the image is typically processed in the spatial

domain using a point detector or matched filter spatial correlation. The Fourier correlation algorithm developed in this chapter is based off a modified LLRT utilizing the statistics of the real component of the Fourier transformed and background-removed spatial image. It was analytically shown that there is a level of covariance between frequencies when an object is present that doesn't exist when no object is present. The Fourier correlation algorithm is designed to improve upon the spatial correlation algorithm by taking the covariance into account in the detection process.

The LROC curve analysis using simulated data showed a significant detection improvement for a given false alarm rate over a spatial correlation technique. When tested at SNR six levels, a 23% increase in detection was noted. The algorithm was also tested at a lower SNR four and found a 11% increase in the detection.

The Fourier correlation algorithm was implemented in MATLAB using simulated data. The algorithm required the covariance matrix to be built from the complete data set and not the theoretical covariance matrix. This is not an ideal situation for several reasons. First, two different covariance matrices must be built, one for the H_1 hypothesis and another for the H_0 hypothesis. In a blind test for detection where no apparent object exists, a covariance matrix could not be built from the data since no detection has been made. Second, if implemented using the theoretical covariance matrix, the target intensity must be known. The research in this chapter was unable to decouple the target intensity from the covariance matrix or the LRT which are both highly dependent on this parameter. When detecting for dim objects, the target intensity will not be known prior to detection. However, the research in this chapter did show that there is correlation between spatial frequencies in the Fourier domain that doesn't exist in the spatial domain. When these correlations are correctly applied in the detection process, the detection performance was shown to improve.

Further research is needed to implement the full Fourier LRT and to develop a solution based on having no prior information on the target intensity in the LRT or in the covariance matrix. While this research showed that correlations in the Fourier domain exist and can be exploited to improve detection performance, further research will determine if post-processing long exposure SSA data in the Fourier domain is a practical approach.

V. Daylight Space Object Detection Using a Short Exposure Frame Selection Algorithm

5.1 Introduction

One of the factors seriously limiting space object detection assets is the inadequate telescope time available to collect data in support of the detection mission. Factors such as hardware upgrades, weather and maintenance all affect the amount of time available for astronomers and operators to collect data. Possibly the greatest hindrance is the amount of prime night sky time available. Imaging during twilight and daylight conditions is possible with smaller aperture telescopes but the detection algorithms are not designed for operating under these conditions. Due to the brighter background and the limited capabilities of the CCD to not reach saturation, short exposure images become necessary during daylight imaging. With a shorter integration time, tens to thousands of short exposure images can be captured in the time that a typical SSA asset collects a single long exposure image. Currently, processing these short exposure images relies on traditional long exposure methods such as a point detector or matched filter [27, 30, 57]. Neither of these methods are optimized to improve detection performance for short exposure imaging as they are developed using long exposure imaging in mind. Lucky imaging is a short exposure image processing technique used within the astronomical community. Significant research has delivered near diffraction limited viewing on up to 2.5m ground-based telescope. However, this technique requires that a guide star be present in the image to evaluate the quality of each short exposure image [37, 38, 39, 42]. Additionally, this method relies on registering and combining the retained images to obtain the processed image. This process is ideal for improving the resolution when imaging an object that is bright enough to easily detect.

There are multiple challenges associated with daylight imaging from large telescopes on both the hardware and software side. Sun avoidance, while not difficult, is necessary to avoid serious damage to optics and sensors. A more difficult challenge exists due to the heating and cooling of large primary mirrors from sun exposure. Small temperature changed in the optical material such as the mirror glass cause large random fluctuations in the optical system that are difficult to measure and correct. Background light bleeding into the optical path must be mitigated to reduce noise and avoid saturation of CCD sensors. Despite these challenges, interest in daylight imaging and detection using large telescopes has increased over the last several years [58, 41, 21].

This research is focused on improving the capability to detect dim and small space objects such as satellites and space debris to improve SSA from short exposure data obtained with current ground based electro-optic systems. The ability to detect dim objects is greatly impacted by the performance of the detection algorithm used to filter the data and decide if an unknown space object is present in the noisy scene. This chapter proposes an improvement upon current detection algorithms by developing a process to selectively average multiple short exposure images to improve the SNR and thus improve the detection performance. Frame selection is accomplished using a two-pass approach to process the data in an effective manner while utilizing a correlation between the resulting data and the expected PSF. Increasing the ability to detect space objects from short exposure images taken during daylight conditions will increase the amount of time a telescope can be operated, provide opportunities to imaging different parts of the sky and therefore increase the number of space objects detected, tracked and then cataloged.

The frame selection algorithm developed in this chapter combines a set of short exposure images that have been filtered to remove images that do not improve the

correlation of the summed frames with an expected PSF. This process differs from the point detector, matched filter and lucky imaging techniques in several ways. First, minimal information is needed to apply this technique. A local guide star or reference point is not required to correlate the image with a PSF or provide a means to examine the quality of the image. Second, local registration of frames is not required. When looking for an unknown object in an image that spans an angle much larger than the tilt-isoplanatic angle, registering frames locally when no object exists in the frame results in noise spikes being registered and false alarms are identified. Gross image registration is still possible using natural guide stars, but this will not remove local motion caused by atmospheric tilt. Third, a decision on the quality of the image is made using all the frames of data in the set. This is significantly different than a lucky imaging technique which evaluates and ranks the quality of each frame individually.

The results of the frame selection short exposure correlation algorithm are compared to the performance of a spatial domain matched filter algorithm like the one used within the space community whose mission is asteroid and/or debris detection. The underlying difference lies in the way the short exposure images are averaged. Unlike a traditional approach which would involve averaging all the frames of data, the proposed algorithm discards noisy and turbulent frames of data that do not improve the overall image. The results are illustrated on a LROC curve which highlights the difference in the probability of detection against the false alarm rate.

5.2 Short Exposure Imaging Techniques

Both traditional spatial correlation and point detection algorithms are designed for utilizing long exposure data with traditionally low background light. A long exposure image is generally used because it allows a lower SNR object to be detected while averaging out lower order atmospheric turbulence and random spikes in intensity due

to the Poisson nature of the photons received. However, under a daylight imaging scenario, the background will be dominant in the image and the intensity of the object appears to be lost in the background light. Short exposure imaging becomes necessary to avoid saturation in the image due to the limited depth of the camera pixel wells and the sheer number of photons arriving during longer integration times in daylight conditions. While there is limited research in detection of space objects using daylight imaging, short exposure imaging is not a new area of research. As described in Chapter 2, lucky imaging is a speckle imaging post-processing technique used within the astronomical community to obtain near diffraction limited images from ground-based telescopes using many short exposure imaging [8, 9, 14-16].

Short exposure imaging is typically utilized for image reconstruction and for obtaining higher resolution imaging from ground-based telescopes. When many frames of data are taken over the course of a single long exposure image time frame the atmosphere over each image is essentially frozen. The brief integration time allows for some images in a set to obtain near diffraction limited viewing conditions since the lower order aberrations such as tip and tilt are not averaged in that time instance. The freezing of the atmosphere over this short time period allows photons to remain concentrated on the CCD. When a select number of these images are registered and combined the result is an increase in the resolution of the combined image. Using the lucky imaging technique with a point source object or a guide star in the image frame, a metric such as the Strehl ratio is used to evaluate the quality or sharpness of each individual frame of data. A defined percentage of bad frames are removed from the ensemble of short exposure images. The remaining frames are then registered and combined to achieve an improved image [38]. The lucky imaging technique can provide significant improvements to spatial resolution under the right conditions and with the appropriate hardware. However, under daylight imaging of dim objects

the technique loses its advantage since the object's SNR is too low for the daylight background and there is no obvious object in the image. As a result, the technique fails to have an object to register and tends to register random noise spikes in the frame if a low SNR object exists in the image or not. Additionally, this technique is difficult to implement in a sky scan and detect mission. Under typical conditions, lucky imaging has an isoplanatic patch of nearly 1 arc-minute or 0.01667 degrees [37]. In order to scan and detect a single 90-degree portion of the sky would require over 50,000 images using the lucky technique with a guide star. This number of images would far exceed the time available for the telescope to capture in a given night.

A significant drawback to short exposure imaging is that the shorter integration time means fewer photons will be measured by the CCD. This fault is typically overcome by averaging together many frames of data to essentially obtain a long exposure image. The Poisson photon noise statistics of the averaged image will be comparable to the sum of the short exposure images since the sum of multiple Poisson random variables is itself a Poisson random variable with a rate parameter equal to the sum of the individual rates [16]. An issue with averaging many short exposure images in traditional night time imaging scenarios is detector readout noise which accumulates as frames are combined. Unlike photon noise, Gaussian distributed detector noise is not signal dependent and is a result of the detector and readout electronics [16, 19].

As the number of expected photons decreases for shorter integration times, the detector noise variance, σ_n^2, becomes significant compared to the Poisson rate parameter, $\bar{K}$. When P frames of data are averaged together, the detector noise variance follows Gaussian statistics and is a function of the number of frames averaged and the readout noise variance given in Chapter 2 with Equation (2.18). Under a daylight imaging scenario, the expected number of photons is significantly large enough even under short exposure integration times that the readout noise variance becomes

insignificant in the received image.

5.3 Algorithm Development

Space object detection algorithms utilize both single and multiple spatial images obtained from ground-based telescopes. Many SSA platforms use multiple frames in their processing chain, however they begin with being able to detect on a single frame and use the multiple frames of follow-up data to confirm or reject the detection decision. Additionally, multiple frames can be tested to reduce the false alarm rate to an acceptable level. The research in this chapter is focused on improving the ability to detect a dim space object from a single frame of data so that detection can be passed on to further multi-frame analysis techniques and follow-up analysis. The detection process chain sometimes includes some amount of pre-processing of the data to do tasks such as measure background, discard faulty pixels or remove known objects from the image using telescope pointing information and a celestial map [59].

This algorithm takes advantage of the short exposure atmospheric turbulence to improve the SNR of the data. The data is divided into subsets of ten frames that will be processed together to emulate a camera imaging at a rate of 10-25 ms. This short time is chosen to reflect the fact that sky surveys looking for new objects must scan the sky in a reasonable amount of time. Instead of simply stacking the images to obtain a higher SNR image, the images are processed and stacked in a manner that further increases the SNR and improves detection performance. This process removes frames of data in the subset that do not contribute to improving the stacked image. Due to the need for multiple frames of data, each iteration of this algorithm would not achieve real time performance however it could operate in a near real time post-processing scheme.

The first step in the daylight space object detection algorithm is to start with a

modified version of the matched filter detection method used with long exposure data. An estimate of the background, B, is obtained by calculating the median value for all pixels in the windowed data as given in Equation (2.3), this estimated background is removed from the data. The algorithm processes 10 frames of short exposure data in each iteration step, this represents the amount of time the telescope would have captured a scene in a long exposure scenario.

Frame Ranking.

This first processing step removes each individual frame one at a time then averages the remaining unregistered frames to obtain $\tilde{d}$. With the n^{th} frame removed from the average, $\tilde{d}$, is convolved with the expected PSF, $h(x, y)$. The convolution of each n^{th} removed summed image and the PSF, $h(x, y)$ is calculated from Equation (5.1), resulting in SNR values for each n^{th} removed frame of data, $Q_{FS}(n)$. This is implemented in the Fourier domain as the multiplication of the Fourier transformed data and the long exposure OTF, H_L, which is the Fourier representation of the PSF. The flow of this initial processing is illustrated in Figure 37. After each frame has been removed and a new SNR value is calculated, the values are ranked in descending order. This translates to ranking which frames decrease the SNR the most when removed from the average and convolved with the PSF.

$$Q_{FS}(n) = \sum_{k=1,k\neq n}^{n} \Big(d_k(x, y) - B \Big) * h(x, y). \tag{5.1}$$

Frame Rejection.

With the ranked frames, the algorithm then processes the ten data frames by removing the one that most significantly decreased the SNR and calculating the new average correlated SNR of the remaining frames using a match filter between the data

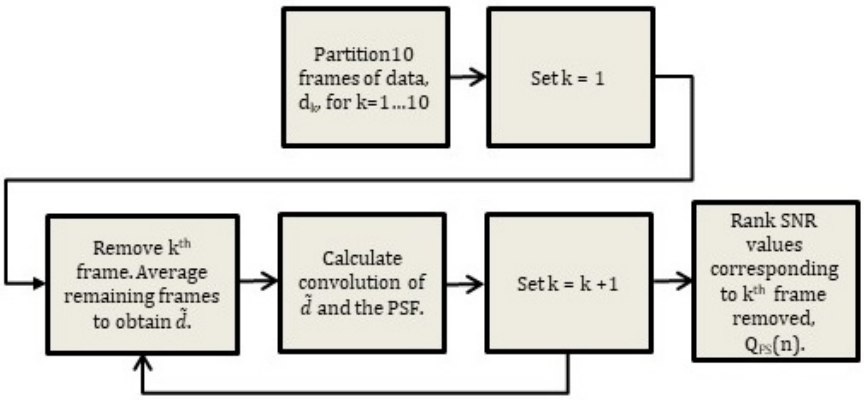

Figure 37. Flow chart of initial processing completed in the short exposure frame selection algorithm.

and the expected PSF. This step utilizes the matched filter SNR given in Equation (2.5). As each poor frame is removed, the correlation between the PSF and the averaged data increases. The algorithm continues to remove frames in descending order until the computed average SNR fails to increase from the last iteration. Once the SNR has reached its peak the algorithm stops removing frames of data. This process differs from the initial processing step in that it is removing the least viable frames first and then computing the SNR. It is important to note that the initial process does not factor in where the peak of the convolution occurs. This becomes apparent in the H_0 case where the algorithm would pick up on noise fluctuations. At no time are the individual frames registered prior to averaging them together. Especially in the H_0 scenario, registration would result in noise spikes being shifted and averaged together to resemble an object.

The process would seem to be counterintuitive, that throwing away data would increase the likelihood of detection using short exposure data. However, under atmospheric conditions, averaging noisy or highly distorted image data could potentially result in a lower SNR image due to the unpredictability of lower order atmospheric aberrations in short exposure image. This process removes frames that do not col-

lectively contribute to improving the SNR of the data. Collecting data using this method requires significantly higher data transfer rates as tens to thousands of short exposure images can be captured in the typical long exposure time frame.

5.4 Simulation and Experimental Data

Simulated and experimental data were used to analyze the performance of the proposed space object detection algorithm. This section describes the setup used to collect the two data sets in detail. In practice, it is likely that a wide FOV camera capturing data on a telescope will contain many thousands of objects. These objects will include stars, satellites and potentially space debris and will all have varying levels of intensity. These objects are treated identically by the algorithm since they would appear as point sources to the optical system. Additionally, the frame of data collected by the optical system is reduced to only test a small subset of the entire frame. This increases the likelihood that multiple objects do not exist within the subset windowed data while decreasing the computational complexity involved in processing large frames of data. This approach is used with other space object detection algorithms [26, 25, 49]. For example, data collected from the SST contains 6144 x 4096 pixels, however, subsets as low as 15 x 15 are used in object detection algorithms. A window of this size allows for a PSF to be contained within the window while providing enough pixels for the background statistics to be calculated. Operationally, the 15 x 15 window would slide across the entire image as each individual pixel was tested. The window size used for testing this algorithm was set at 20 x 20 pixels. Outside of computation time and possible interference from other objects, there is no reason that a larger window could not be chosen [26].

Simulated Data.

The simulated data was developed in MATLAB to mimic a single point source object within the data frame. The parameters used in the simulation are summarized in Table 4. The use of MATLAB to create data allowed the ability to simulate accurate statistical distributions and create realistic looking data while removing unknown variables in the scenario. Removing these unknown variables limits the data to investigate only the scope of the research in the proposed algorithm. Images were simulated under both the hypothesis that an object is present at the pixel location being tested and that no object is present in the scene. Under the H_1 hypothesis, an object exists at the tested pixel location, (x_0, y_0). The intensity of the object was set at 2000 photons with a background of 10,000 photons. To test the algorithm at various signal levels, the seeing parameter, r_0, was varied between 5 cm and 8 cm. The higher r_0 results in a more compact PSF and less spreading of the target intensity across multiple pixels. Under the H_0 hypothesis, no object exists in the scene. This hypothesis is simulated using the same statistical assumptions for background light and the atmosphere except the intensity of the object is set to zero to represent no target at pixel location (x_0, y_0).

Accurate short and long exposure PSF statistics were incorporated based on correlated turbulence models and built-in Poisson random variable functions were used to simulate accurate statistical distributions for the background noise [52]. Temporally evolving correlated short exposure PSFs were generated and averaged together to get the effective long exposure PSF in Figure 38. The figure clearly shows the effect r_0 has on the PSF with the diminished intensity spread in scenario two.

For each hypothesis, 10,000 frames of short exposure data were simulated. Long exposure data was generated by averaging together 10 frames of short exposure data. An example of the long and short exposure data for the second scenario is shown in

Figure 39, the object in this scenario cannot be detected from a single frame to the naked eye. Data for scenario one is not shown since the intensity of this object is lower than the second scenario and would also appear as noise to the eye.

Table 4. Parameters used to create simulated data in MATLAB.

Parameter	**Scenario 1**	**Scenario 2**
Aperture Diameter, D (cm)	4.5	4.5
Fried Parameter, r_0 (cm)	5.0	8.0
Object Intensity, θ (photons)	2,000	2,000
Background, B (photons)	10,000	10,000
Window Size, N (pixels)	32	32
Number of Frames	10,000	10,000

Figure 38. Point spread functions used to generate simulated data and conduct spatial correlation testing. Scenario 1: PSF with $r_0 = 5$ cm (left side). Scenario 2: PSF with $r_0 = 8$ cm (right side).

Experimental Data.

Experimental data was collected using a hybrid approach in an optics laboratory. A camera, aperture stop and focusing lens were set up on an optical bench to capture frames of data. A hot air fan was used in the optical path to induce random atmospheric turbulence in the scene. A light emitting diode (LED) behind a 75-micron

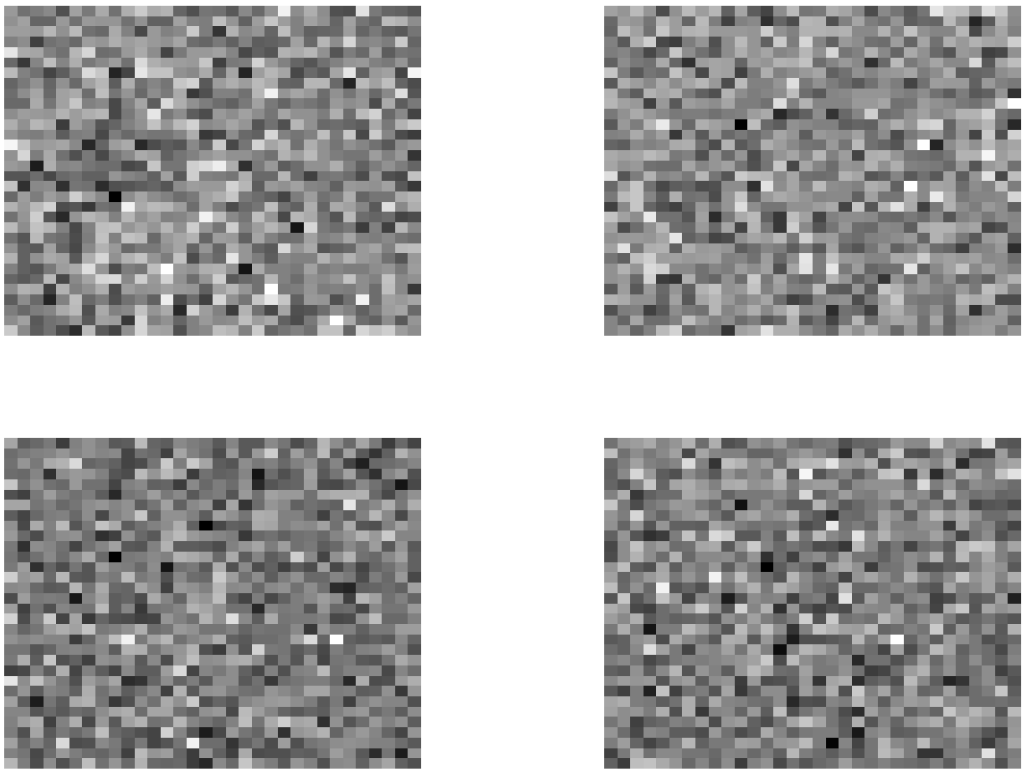

Figure 39. Scenario 2: Simulated short exposure H_1 data (upper left side). Simulated short exposure H_0 data (upper right side). Simulated long exposure H_1 data (lower left side). Simulated long exposure H_0 data (lower right side).

pinhole was placed in focus with the detector after passing through a neutral density filter and reflecting off two mirrors on the end of the optical table using a 500mm focal length lens. A computer screen was placed out of focus behind the mirror to provide an adjustable background light source. This hybrid approach allowed for producing a point source object with a bright background at varying SNR levels by adjusting the background brightness, neutral density filter and integration time. Using this approach removes the entirely simulated environment and provides randomness to collected data while allowing for ease in adjusting the intensity of the background compared to the point source object.

To collect H_1 data, the MATLAB displayed image was adjusted to a 256-grayscale

image with the background level set to 3/4 the maximum brightness of the object and the LED turned on to represent the object. This provided nearly 10,000 counts of background light on the detector. 2,000-3,000 short exposure images were collected under the two different scenarios. One with the camera integration time set to 10 ms and another at 25 ms. Similarly, 5,000 frames of H_0 data was collected with the same intensity level for the background and integration times except the LED is turned off to remove the object from the image. The parameters for the experimental data collected in the lab are summarized in Table 5. An example of the collected short exposure data under each hypothesis and the resulting long exposure image is shown in Figure 40 for the first scenario and Figure 41 for the second scenario with a longer integration time.

Table 5. Parameters used to generate experimental data.

Parameter	**Scenario 1**	**Scenario 2**
Camera	ThorLabs 8050M-GE-TE	ThorLabs 8050M-GE-TE
Display	Dell UltraSharp U2410	Dell UltraSharp U2410
Average Background Counts, B (short exposure)	804	1950
LED Pinhole Size (micron)	75	75
Aperture Diameter, D (cm)	2	2
Integration time, (msec)	10	25
Neutral Density Filter, (optical density)	0.8	1.0
Focusing Lens, f_l (mm)	500	500
Window Size, N (pixels)	32	32
Number of Frames	2,000	3,000

The long exposure PSF of the optical system is needed for object detection using the spatial correlator. This was experimentally collected by removing the monitor background light and imaging the point source LED. The camera was integrated for 100 ms to obtain the long exposure PSF, shown in Figure 42. One observation noted is the smaller PSF in the experimental data compared to the simulation. This is due to the larger sampling of the data in the CCD. This binning of data effectively reduces the size of the PSF and object footprint on the CCD. However, this has no effect on the algorithm since the PSF is an accurate model of the expected data under the H_1

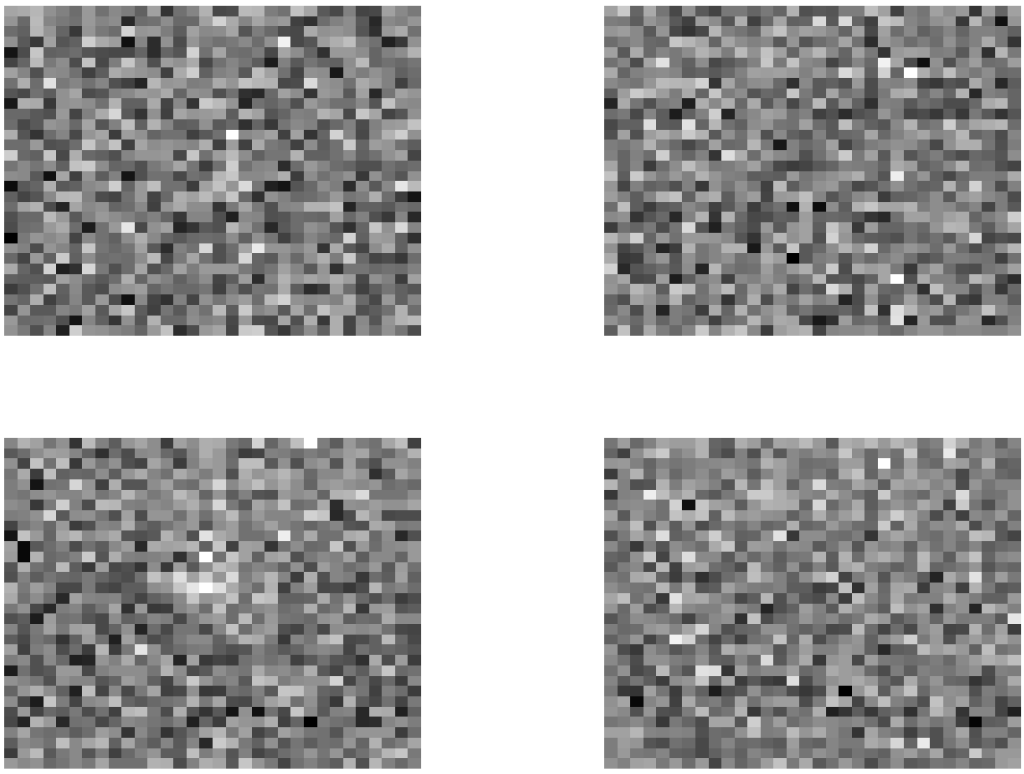

Figure 40. Scenario 1: Experimental short exposure H_1 data (upper left side). Experimental short exposure H_0 data (upper right side). Experimental long exposure H_1 data (lower left side). Experimental long exposure H_0 data (lower right side).

hypothesis. The PSF was collected both with the hot air fan on and off to confirm atmospheric turbulence effects.

5.5 Results & Analysis

To properly evaluate the performance of this algorithm, the exact same script must be used for H_1 and H_0 data sets. The MATLAB script for processing this data only requires the captured data set and does not require any preset information outside of the expected PSF. The expected PSF can be obtained by imaging a nearby star or estimated from system parameters and a measurement of the seeing parameter,

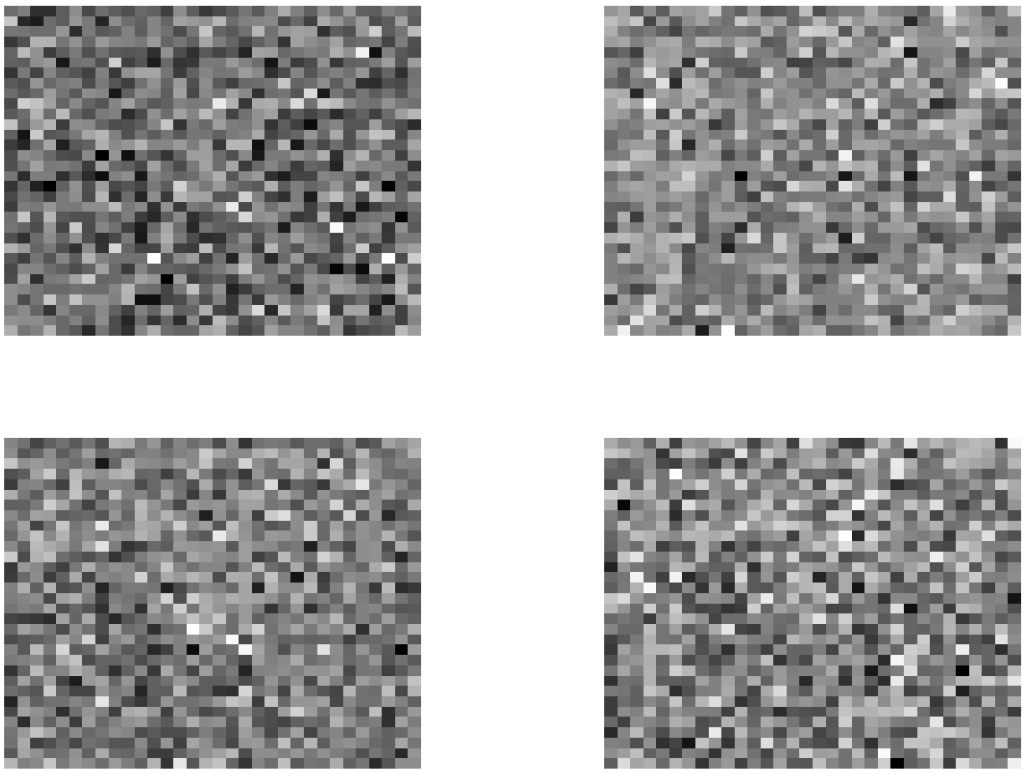

Figure 41. Scenario 2: Experimental short exposure H_1 data (upper left side). Experimental short exposure H_0 data (upper right side). Experimental long exposure H_1 data (lower left side). Experimental long exposure H_0 data (lower right side).

Figure 42. Collected long exposure PSF. No hot air fan generating turbulence (left side). With hot air fan generating turbulence (right side).

r_0, using the long exposure PSF formula given in Equation (2.15). While the data collected is defined as short exposure, the long exposure PSF model is used since the individual frames of data are averaged together prior to correlation to create an effective long exposure image.

The LROC curve does not require a specific detection threshold to be set. Instead, the P_D and P_{FA} are both calculated for the full range of threshold values that result in detection and false alarm probabilities between zero and one. The LROC curve is built by modeling the SNR values from the algorithm's test data as Gaussian random variables. The mean and variance of the test statistic can then be used to generate the detection and false alarm probabilities using a Gaussian PDF. The upper right corner of the LROC curve represents the performance of the algorithms as the threshold is lowered.

Using the simulated data, the performance of the new algorithm proposed in this paper was compared to both a traditional matched filter approach and a lucky imaging technique. Under the traditional matched filter, the 10 frames of data are averaged together, no frames are removed, and the data is correlated with the expected PSF and calculates the SNR using the matched filter. The lucky imaging technique was set with a selection rate of 40%. The best four frames of data are selected using the Strehl ratio as a quality metric, these frames were registered and averaged. The LROC curves for the simulated data for both scenarios are shown in Figure 43 and Figure 44. The LROC curve using the simulated data illustrates the difficulty the lucky technique encounters with low SNR objects. Selection rates of 10 and 20% were also attempted with the lucky imaging technique but produced even worse results. The results from both of the LROC curves show a significant P_D increase for a given P_{FA} when operating in the low SNR regime for the new frame selection algorithm. The low SNR can be predicted by examining the data in Figure 39 and seen by the

extremely low detection probability for a $P_{FA} \approxeq 10^{-9}$. At this operational level of false alarm, the frame selection algorithm shows a nearly 10% improvement in the P_D under scenario one and a 25% improvement under scenario two which had better seeing conditions and less spreading of the target intensity due to the smaller PSF. There is a point in upper right corner of Figure 43 where the traditional matched filter outperforms the proposed algorithm. In this region, the false alarm rate is significantly higher and above levels used in operation.

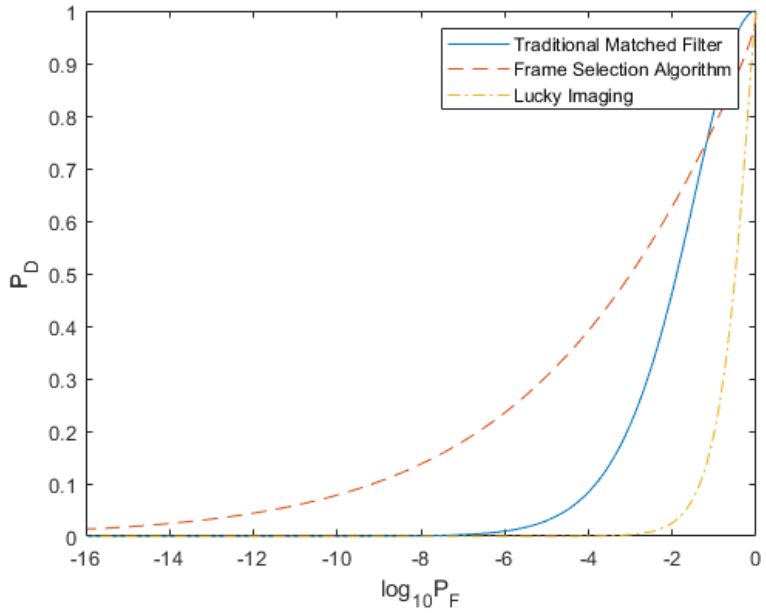

Figure 43. LROC curve using simulated data under the first scenario.

A LROC curve was also generated using experimental data collected as described in Section 5.4. The LROC curves for each scenario are shown in Figures 45 and 46. At a 10^{-9} false alarm rate, the new frame selection algorithm achieved a 20% increase in the probability of detection under the first scenario and 6% increase under the second scenario. At slightly higher false alarm rates, the frame selection algorithm achieved significantly higher detection probabilities. Although the scenario parameters for the simulated and experimental data are different, the new algorithm shows performance

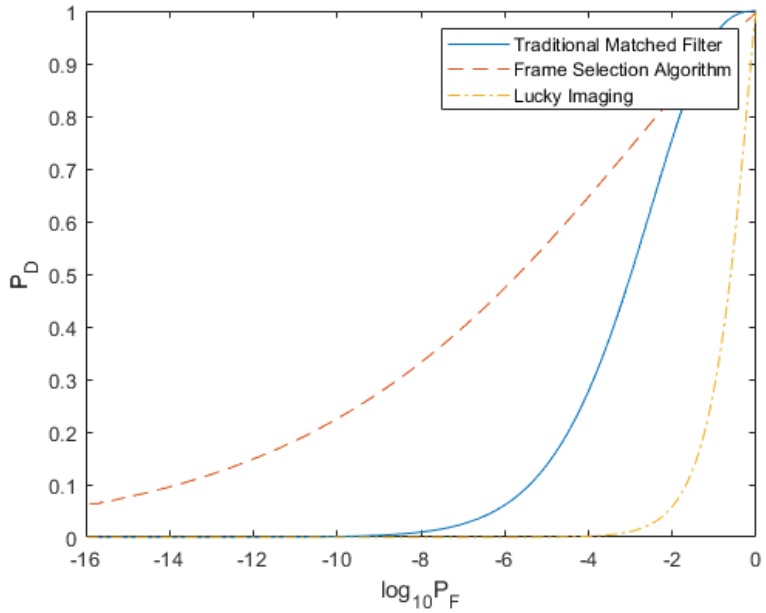

Figure 44. LROC curve using simulated data under the second scenario.

increases in both data sets.

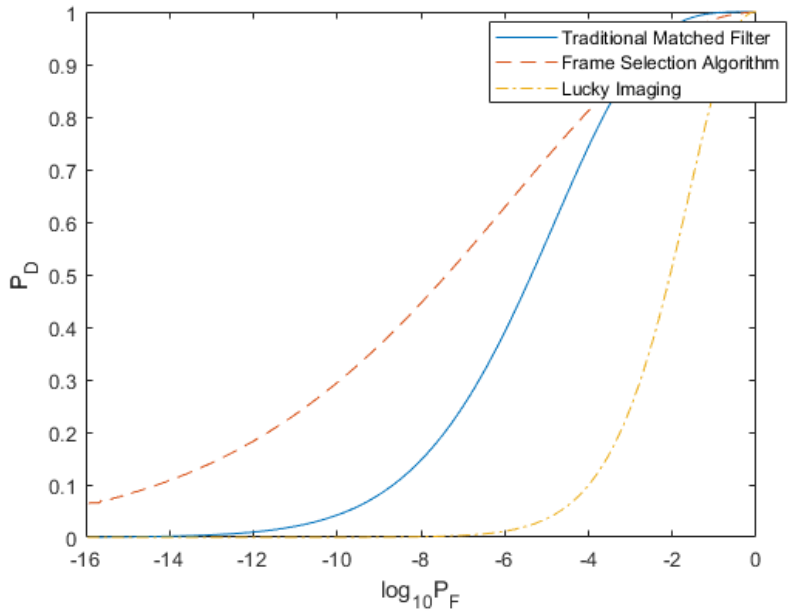

Figure 45. LROC curve using experimental data under the first scenario.

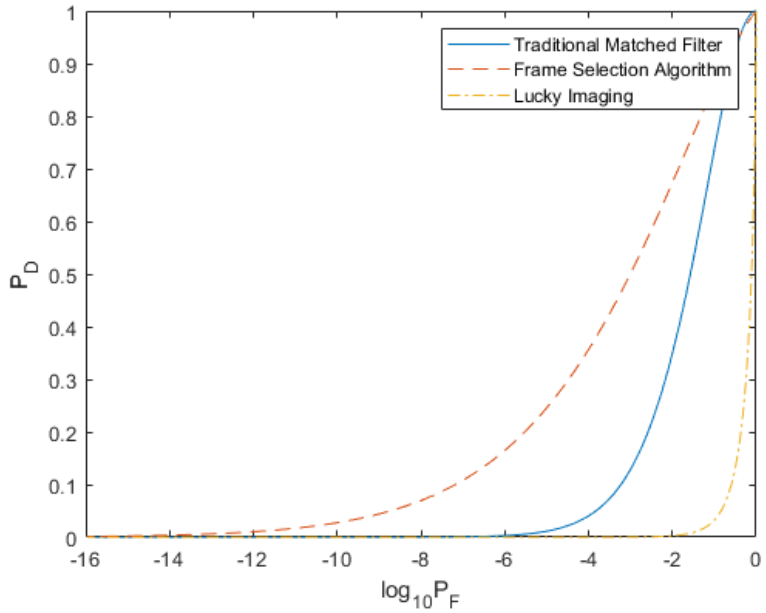

Figure 46. LROC curve using experimental data under the second scenario.

5.6 Conclusion

This chapter presents a method to improve the probability of detecting dim or low SNR space objects in images obtained during bright sky daylight conditions. Under daylight imaging conditions, it is required to reduce the integration time of the sensor down to short exposure time intervals to accommodate the increased number of photons arriving at the CCD and the limited well depth. Two techniques for post-processed object detection were examined and compared to the proposed algorithm. First, a matched filter algorithm approach using a single frame of data obtained by averaging the individual frames. Second, a lucky imaging approach was examined that selects a portion of the short exposure frames based on their quality which are then registered and combined. The proposed algorithm considers that under short exposure conditions there will be time instances that result in excellent viewing and times when the atmosphere is particularly poor, and the image is greatly distorted.

The algorithm iteratively removed frames to generate a higher SNR image which results in increased detection probabilities. Unique to this approach is that the PSF of the object is not required for correlating or for using as a reference in evaluating the quality of each individual short exposure image. The entire set of short exposure images is used to reject frames that do not improve the quality of the combined image. Additionally, image registration is not utilized due to the assumed low SNR of the object. This results in a lower false alarm rate as noise spikes are not registered and combined to create a false object.

Using both simulated and experimental data, the algorithm demonstrated the ability to significantly improve the probability of detection by 5-25% for low SNR objects while maintaining low false alarm rates. This could potentially result in a significant number of new detections found if implemented using current SSA systems.

This approach does require short exposure imaging with hardware that would require higher frame rates. The sensor must output significantly more frames of data in the same time as a single image frame. The higher frame rate can result in significantly greater readout noise when averaging the frame together. Under daylight imaging, this is mitigated due to high photon counting noise becoming the dominating noise source. It is possible that this algorithm's approach would be feasible under traditional night sky imaging if additive noise from the detector, camera's readout electronics and dark current was significantly less than the noise induced by the background, or if the object was significantly bright. However, current algorithms already work well with high SNR object.

With an increase in the number of assets launched into space, the need to improve our detection and tracking of harmful objects will only increase as well. It is likely this will further constrain tight budgets and operators time with telescope assets. The potential to improve the detection capability of imaging in the daylight could

mitigate some of these issues while providing newer areas of the sky to scan and an increased number of object detections.

Future research focused on refining the frame selection process to better select frames would increase the correlated SNR. This would increase the performance of the algorithm. Additionally, this algorithm can be tested using data obtained from a SSN sensor for further testing and evaluation. Utilizing a faster camera with less readout noise, the algorithm could be developed for shorter integration times and a great number of frames used in each iteration. The research in this chapter was focus on improving detection on daylight images. Additionally, a camera with extremely low readout noise would allow multiple short exposure images of typical night sky images to be averaged without readout noise variance burying the signal.

VI. Conclusion

This chapter summarizes the research results and contributions of this dissertation to address the three research questions raised in Chapter 1. Potential follow-on research to expand each of these topics will be presented. Additionally, conferences and publications that resulted from this work are listed in this chapter.

6.1 Research Goals, Work Completed & Future Research Topics

The stated goal of this research was to improve the ability to detect small or dim space objects using spatial images obtained from existing ground-based telescopes. The research in this dissertation was focused on improving the performance of the SSA detection mission for potential use within the DoD, USAF and others within the astronomical community. In Chapter 1, three questions addressed in this research were listed. Each of those questions, the research conducted in this dissertation to answer those questions and future related research on each topic is listed below.

In order to continue to detect new, smaller and dimmer objects, there will continue to be advancements in object detection algorithms based on images taken from small and large aperture ground-based telescopes. Advancements in computing power will allow more complex algorithms. It is unlikely that the current approaches are the best, and no further improvements could be made. There are future research opportunities in each of the three chapters of this dissertations.

1. *Will converting a spatial image to the Fourier domain improve the detection performance of a point source detector?*

Chapter 3 of this research specifically addresses this question. In this chapter,

an algorithm was developed that utilized the Fourier transform of a long exposure spatial image obtained from a ground-based telescope. The Fourier point detection algorithm developed in this chapter compared the performance to a spatial point detection algorithm similar to the one used by large telescopes within the SSN such as the SST. A statistical model was developed for the data obtained under both the hypothesis that an object exist in the scene (H_1) and that no object exist in the scene (H_0). The mean and variance of the data under each hypothesis was calculated to build a LRT using a Gaussian PDF.

Compared to a spatial point source, the Fourier point source algorithm had a 40% improvement in the probability of detection at a false alarm rate of 10^{-9}. When compared to a spatial correlation or matched filter algorithm, the Fourier point source algorithm achieved detection performances that were nearly the same as a spatial correlator which knew the true PSF shape. The distinct advantage in the Fourier point source is that no knowledge of the PSF is needed to run the detection scheme. In a spatial correlator, the data is correlated against the expected PSF. In many scenarios, the shape of the PSF is unknown and must be estimated. The Fourier point source detector does not correlate the received image to produce a SNR value. When compared to a spatial correlator using an incorrect PSF shape, the Fourier point detector produced a 34% improvement in the probability of detection.

This research in this chapter, concluded with the development of the Fourier point detector. However, there is likely more information to be obtained from the Fourier domain that could improve a spatial point detection algorithm. The performance of a spatial point detector is highly sensitive to the measured standard deviation of the background. As the estimate of the standard deviation varies from the truth, the algorithm will fail to identify an object at the correct SNR threshold. This is usually estimated by looking at all the pixels in the image. However, this could be

skewed by known objects, bright pixels due to noise or outside sources, and a large PSF. It is possible that Fourier domain analysis might provide a better estimate of the backgrounds standard deviation. Specifically, the imaginary component of the Fourier transform which should contain only noise in a long exposure scenario. Such research could lead to an improved estimate of the background statistics and would improve a spatial point detectors performance.

2. *Can a covariance matrix between spatial frequencies in a Fourier domain image be used to build a Fourier correlation algorithm to improve object detection?*

This question is addressed by the research in Chapter 4, which is an extension of the point detector built in Chapter 3. In this chapter, a model for the real component of the Fourier transform of the background-removed data is developed. The mean and variance under each hypothesis from Chapter 3 research was utilized in building this algorithm. A model for the covariance between spatial frequencies of the Fourier transformed data was developed. A LRT was then built using a joint Gaussian PDF for each hypothesis. The covariance matrix under the H_0 hypothesis was diagonal. This indicates that there is no covariance between spatial frequencies. However, under the H_1 hypothesis, there existed small correlations between local spatial frequencies.

The Fourier correlation algorithm developed in this chapter was compared to a traditional spatial correlation algorithm widely used within the community. Long exposure data was simulated in MATLAB to mimic a dim space object in a turbulent atmosphere at a SNR value of 6. When tested with simulated data and compared using a LROC curve, the Fourier correlation algorithm achieved a significant 11-23% increase in detection probability at a false alarm rate of 10^{-9}.

Challenges exist incorporating this algorithm into the detection process. The two

covariance matrices utilized in the algorithm were based off the measured data which is not an ideal scenario. Ideally, the theoretically derived covariance matrix could be utilized in the detection process. However, this research did show that there exists a correlation between spatial frequencies in the Fourier domain of an image. When these correlations are taken into account, they can be used to significantly improve a traditional spatial correlation algorithm which is built on all spatial points being independent random variables.

There is a great opportunity to further the research in this chapter. There was a correlation between spatial frequencies in the Fourier transformed image both theoretical and experimentally using simulated data. However, this research was limited to using all the experimentally developed covariance matrix. Further research into this correlation could improve detection performance that did not require building a covariance matrix based on the pointing position of the telescope at the time of data capture.

3. *Under daylight imaging where short exposure images are necessary, will frame selection increase the ability of detecting objects over simply combining multiple frames?*

In Chapter 5, a short exposure imaging detection algorithm was developed. There is growing interest within the SSA community to collect images from large ground-based telescopes during the broad daylight. Many unique engineering challenges exist in order to accomplish this feat that go beyond the scope of this research. However, the work in this chapter was to develop an algorithm to process and detect objects from this data. Due to the bright background and limiting sensors, short exposure imaging becomes necessary during daylight imaging. There are current short exposure techniques designed to image quality and resolution however these are not practical

for scanning a large area of space for object detection. Typically, all short exposure images are averaged together to obtain a long exposure image which is then correlated with an expected PSF. In some short exposure techniques, the frames are registered prior to combining.

The frame selection algorithm developed in this chapter was an iterative process which selectively removed frames that did not contribute positively to the SNR of the image. The frames are then evaluated based on their SNR contribution rank to test their contribution to the ensemble of images. The frames which are kept are then correlated with the expected PSF. This process requires no registration of frames which is significant when working with dim objects in a bright background since there is no apparent object to register. Registration, as was shown by the lucky imaging results, causes a significantly high false alarm rate and can't be used in these scenarios.

A dim object in a bright background was simulated in MATLAB to create data under two different scenarios. Statistically accurate short exposure atmospheric turbulence models are utilized along with Poisson noise statistics to create data under both hypothesis. Data was also collected in the optics laboratory with an electronically cooled CCD using a hot air fan to generate turbulence along the optical path and a point source object created with a LED behind a pinhole. Background light was added to the experiment using an brightness adjustable computer display.

The performance of the algorithm was compared to both a spatial correlation and lucky imaging algorithm on a LROC curve. With simulated data, the frame selection algorithm achieved a 10-25% improvement in the probability of detection at a 10^{-9} false alarm rate. Using experimental data, an improvement of 6-20% was noted depending on the parameters used to adjust the SNR of the object. The results show that when short exposure images are selectively rejected prior to combining,

significant detection rates are achieved and would lead to a greater number of space objects detected.

The algorithm developed in this chapter should be further tested using imagery obtained from a ground-based telescope to further showcase the detection performance increases. Additionally, I do not believe this algorithm has to be limited to daylight imaging scenarios. It was in this research due to the need for a low noise, fast readout sensor. However, if the readout noise was low enough, multiple short exposure images could be averaged of night sky conditions without the readout noise swamping the signal. This would expand the adaptability of this algorithm to many sensors within the SSN as few today are capable of daylight imaging. Additionally, the algorithm developed in this chapter was based on using 10 frames of data. This was chosen since 10 frames of short exposure data could be captured in the time frame of a typical long exposure scene. Further improvements of dimmer space object could potentially be possible by using many more short exposure frames.

6.2 Publications

To ensure the originality and significant contribution of the research in this dissertation, each portion of this research was submitted and published as either a conference or journal paper for evaluation and critic from experts within the field.

Conference Presentations & Papers

- Fourier point detector research and results from Chapter 3 was published and presented at the SPIE Optics + Photonics Conference.

  D. Becker and S. Cain. Improving space object detection using a Fourier likelihood ratio detection algorithm, in SPIE Optics + Photonics, International Society for Optics and Photonics, 2016.

- Fourier correlation algorithm research and results from Chapter 4 was published and presented at the Advanced Maui Optical and Space Surveillance Technologies Conference.

  D. Becker and S. Cain. A Space Object Detection Algorithm using Fourier Domain Likelihood Ratio Test, Advanced Maui Optical and Space Surveillance Technologies Conference, 2017.

Journal Article

- Frame selection research and results from Chapter 5 was published in Applied Optics and selected as an "Editor's Choice" article.

  David Becker and Stephen Cain, "Improved space object detection using short-exposure image data with daylight background," Applied Optics 57, 3968-3975 (2018)

Bibliography

1. US Department of Defense and Office of the Director of National Defense. National Security Space Strategy Unclassified Summary. page 14, 2011.

2. Office of the President of the United States of America. National Space Policy of the United States of America. *United States Government*, page 18, 2010.

3. US Congress. National Aeronautics and Space Administration Authorization Act of 2005, 2005.

4. NASA Near Earth Object Program, http://neo.jpl.nasa.gov/.

5. NASA Orbital Debris Program Office, https://orbitaldebris.jsc.nasa.gov/.

6. Steven Hildreth and Allison Arnold. Threats to U.S. National Security Interests in Space: Orbital Debris Mitigation and Removal. 2014.

7. Joint Functional Component Command for Space, http://www.vandenberg.af.mil/About-Us/Fact-Sheets/Display/Article/338339/joint-functional-component-command-for-space/.

8. Bryce Space & Technology. State of the Satellite Industry. Technical report, 2017.

9. Caleb Henry. SpaceX, OneWeb detail constellation plans to Congress, http://spacenews.com/spacex-oneweb-detail-constellation-plans-to-congress/, 2017.

10. Ground-based electro-optical deep space surveillance, http://www.af.mil/About-Us/Fact-Sheets/Display/Article/104594/groundbased-electro-optical-deep-space-surveillance, 2010.

11. National Aeronautics and Space Administration. Orbital Debris Quarterly News. *Orbital Debris Quarterly News*, 20(1 & 2).

12. Nicholas Kaiser. Pan-STARRS: a wide-field optical survey telescope array. (September 2004):11, 2004.

13. Deborah Woods, Ronak Shah, Julie Johnson, Alexander Szabo, Eric Pearce, Richard Lambour, and Walter Faccenda. The Space Surveillance Telescope: Focus and Alignment of a Three Mirror Telescope. In *Advanced Maui Optical and Space Surveillance Technologies Conference*, 2012.

14. Joel Wm Parker, S Alan Stern, Peter C Thomas, Michel C Festou, William J Merline, Elliot F Young, Richard P Binzel, and Larry A Lebofsky. Analysis of the First Disk-Resolved Images of Ceres from Ultraviolet Observations with the Hubble Space Telescope. *The Astronomical Journal*, 123:9, 2001.

15. Elizabeth Howell. Asteroid Skimming Past Earth May Loom Larger Than Exploding Russian Meteor, 2018.

16. Hanneke Weitering. 'Tunguska'-Size Asteroid Makes Surprise Flyby of Earth, 2017.

17. National Aeronautics and Space Administration. Orbital Debris Quarterly News. *Orbital Debris Quarterly News*, 9(2).

18. Russian Satellite Hit by Debris from Chinese Anti-Satellite Test, http://www.space.com/20145-russian-satellite-chinese-debris-crash-infographic.html.

19. Michael Roggemann and Byron Welsh. *Imaging Through Turbulence*. CRC Press, Boca Raton, FL, 1996.

20. Michael Hart, Stuart M. Jefferies, Douglas A. Hope, James G. Nagy, and Ryan Swindle. A Comprehensive Approach to High-Resolution Daylight Imaging for SSA. In *Advanced Maui Optical and Space Surveillance Technologies Conference*, 2016.

21. John D. Gonglewski, Ronald G. Highland, David C. Dayton, Steven C. Sandven, Samuel C. Rogers, and Stephen L. Browne. ADONIS: daylight imaging through atmospheric turbulence. In *International Symposium on Optical Science, Engineering, and Instrumentation*, number October 1996, pages 152–161, 1996.

22. T W Lawrence, D M Goodman, E M Johansson, and J P Fitch. Speckle imaging of satellites at the U.S. Air Force Maui Optical Station. *Applied optics*, 31(29):6307–21, 1992.

23. Spacewatch Project, http://spacewatch.lpl.arizona.edu/.

24. Joseph W. Goodman. *Statistical Optics*. John Wiley & Sons, Inc., New York, 2000.

25. John C Zingarelli. *Enhancing Ground Based Telescope Performance With Image Processing*. PhD thesis, Air Force Institute of Technology, 2013.

26. Tyler Hardy. *Optical Theory Improvements to Space Domain Awareness*. PhD thesis, Air Force Institute of Technology, 2016.

27. Stephen C. Pohlig. An Algorithm for Detection of Moving Optical Targets. *IEEE Transactions on Aerospace and Electronic Systems*, 25(1):56–63, 1989.

28. Steven M Kay. Fundamentals of Statistical Signal Processing, Volume 2: Detection Theory, 1998.

29. Anthony O'Dell. *Detecting Near-Earth Objects Using Cross-Correlation With A Point Spread Function*. PhD thesis, Air Force Institute of Technology, 2009.

30. H. Viggh, G. Stokes, F. Shelly, M. Blythe, and J. Stuart. Applying Electro-Optical Space Surveillance Technology to Asteroid Search and Detection: The LINEAR Program Results. *Space 98*, pages 373–381, 1998.

31. DF Woods, RY Shah, Julie A. Johnson, Alexander Szabo, Eric C. Pearce, Richard L. Lambour, and Walter J. Faccenda. Space Surveillance Telescope: focus and alignment of a three mirror telescope. *Optical Engineering*, 52(5):053604, 2013.

32. Stephen Cain. Improved space object detection via scintillated short exposure image data. 9982:99820K–99820K–8, 2016.

33. E. Bertin and S. Arnouts. SExtractor: Software for source extraction. *Astronomy and Astrophysics Supplement Series*, 117(2):393–404, 1996.

34. Joseph W. Goodman. *Introduction to Fourier Optics*. Roberts & Company, Englewood, CO, 3rd edition, 2005.

35. Stephen C. Cain Tyler J. Hardy. Characterizing Point Spread Function (PSF) fluctuations to improve Resident Space Object detection (RSO). In *Sensors and Systems for Space Applications VIII*, 2015.

36. John H. Seldin, Michael F. Reiley, Richard G. Paxman, Bruce E. Stribling, Brent L. Ellerbroek, and Dustin C. Johnston. Space object identification using phase-diverse speckle. In *Image Reconstruction and Restoration II*, pages 2–15, San Diego, CA, 1997.

37. Craig Mackay. High-Resolution Imaging with Large Ground-Based Telescopes. *Optics and Photonics News*, 20(11):22, 2009.

38. Craig Mackay. High-efficiency lucky imaging. *Monthly Notices of the Royal Astronomical Society*, 432(1):702–710, 2013.

39. J.-L. Nieto and E. Thouvenot. Recentring and selection of short-exposure images with photon-counting detectors. *Astronomy and Astrophysics*, 241(2):663–672, 1991.

40. David L. Fried. Probability of getting a lucky short-exposure image through turbulence*. *Journal of the Optical Society of America*, 68(12):1651, 1978.

41. Douglas A. Hope, Stuart M. Jefferies, Michael Hart, and James G. Nagy. High-resolution speckle imaging through strong atmospheric turbulence. *Optics Express*, 24(11):12116, 2016.

42. Nicholas M. Law, Craig D. Mackay, and John E. Baldwin. Lucky Imaging: High Angular Resolution Imaging in the Visible from the Ground. *Astronomy and Astrophysics*, 446:739–745, 2005.

43. Harry L. Van Trees. *Detection, Estimation and Modulation Theory*. Wiley, New York, 1968.

44. Stephen C. Cain and Richard D. Richmond. *Direct-Detection LADAR Systems*. SPIE Publications, 2010.

45. Steven M Kay. Intuitive probability and random processes using MATLAB, 2006.

46. Harald Cramèr. *Mathematical Methods of Statistics*. Princeton University Press, 1946.

47. Robert J. Noll. Zernike polynomials and atmospheric turbulence. *Journal of the Optical Society of America*, 66(3):207, 1976.

48. Kevin P Vitayaudom. *Analysis of Non-uniform Gain for Control of a Deformable Mirror in an Adaptive-Optics System*. Master's thesis, Air Force Institute of Techology, 2008.

49. D. Monet, T. Axelrod, C. Claver, T. Blake, R. Lupton, E. Pearce, R. Shah, and D. Woods. Rapid Cadence Collections with the Space Surveillance Telescope. In *AMOS*, Maui, Hi, 2012.

50. Pan-STARRS, http://pan-starrs.ifa.hawaii.edu/public/home.html.

51. D. L. Fried. Optical Resolution Through a Randomly Inhomogeneous Medium for Very Long and Very Short Exposures. *Journal of the Optical Society of America*, 56(10):1372, 1966.

52. Isaac Putnam. *Atmospheric Impact on Long Pulse Laser Detection and Ranging (LADAR) Systems*. Master's thesis, Air Force Institute of Technology, 2013.

53. Adam Macdonald. *Blind Deconvolution Of Anisoplanatic Images Collected By A Partially Coherent Imaging System*. PhD thesis, Air Force Institute of Technology, 2006.

54. James Stewart. *Calculus: Concepts and Contexts*. Brooks/Cole, Pacific Grove, CA, 2nd edition, 2001.

55. G. I. Taylor. The Spectrum of Turbulence. *Proceedings of the Royal Society A: Mathematical, Physical and Engineering Sciences*, 164(919):476–490, feb 1938.

56. R. C. Pierce. A Brief History of Logarithms. *The Two-Year College Mathematics Journal*, 8(1):22–26, 1977.

57. J. Chris Zingarelli, Eric Pearce, Richard Lambour, Travis Blake, Curtis J R Peterson, and Stephen Cain. Improving the space surveillance telescope's performance using multi-hypothesis testing. *Astronomical Journal*, 147(5), 2014.

58. Steven Griffin, Andrew Whiting, Shawn Haar, and Stacie Williams. Compliant Baffle for Large Telescope Daylight Imaging. In *Amostech*, pages 1–5, 2014.

59. Jessica D. Ruprecht, J. Scott Stuart, Deborah Freedman Woods, and Ronak Y. Shah. Detecting small asteroids with the Space Surveillance Telescope. *Icarus*, 239:253–259, 2014.

REPORT DOCUMENTATION PAGE

Form Approved
OMB No. 0704-0188

1. REPORT DATE *(DD-MM-YYYY)*	2. REPORT TYPE	3. DATES COVERED *(From - To)*
13-09-2018	Doctoral Dissertation	Sept 2015-Sept 2018

4. TITLE AND SUBTITLE

Techniques for Improved Space Object Detection Performance from Ground-Based Telescope Systems Using Long and Short Exposure Images

5a. CONTRACT NUMBER

5b. GRANT NUMBER

5c. PROGRAM ELEMENT NUMBER

6. AUTHOR(S)

Becker, David J, Major

5d. PROJECT NUMBER

5e. TASK NUMBER

5f. WORK UNIT NUMBER

7. PERFORMING ORGANIZATION NAME(S) AND ADDRESS(ES)

Air Force Institute of Technology
Graduate School of Engineering and Management (AFIT/EN)
2950 Hobson Way
Wright-Patterson AFB OH 45433-7765

8. PERFORMING ORGANIZATION REPORT NUMBER

AFIT-ENG-DS-18-S-006

9. SPONSORING/MONITORING AGENCY NAME(S) AND ADDRESS(ES)

Air Force Office of Scientific Research
Stacie E. Williams
875 N. Randolph St, Arlington, VA 22203
(703) 588-8213
stacie.williams.1@us.af.mil

10. SPONSOR/MONITOR'S ACRONYM(S)

AFOSR/RT

11. SPONSOR/MONITOR'S REPORT NUMBER(S)

12. DISTRIBUTION/AVAILABILITY STATEMENT

DISTRIBUTION STATEMENT A:
APPROVED FOR PUBLIC RELEASE; DISTRIBUTION UNLIMITED.

13. SUPPLEMENTARY NOTES

14. ABSTRACT

Space object detection is of great importance in the highly dependent yet competitive and congested space domain. Detection algorithms employed play a crucial role in fulfilling the detection component in the space situational awareness mission to detect, track, characterize and catalog unknown space objects. Many current space detection algorithms use a matched filter or a spatial correlator on long exposure data to make a detection decision at a single pixel point of a spatial image based on the assumption that the data follows a Gaussian distribution. This research focuses on improving current space object detection algorithms and developing new algorithms that provide a greater detection performance, specifically with dim and small objects which are inherently difficult to detect. With a greater detection rate, a great number of unknown objects will be detected, tracked and cataloged to deliver safer space operations. Three novel approaches to object detection using long and short exposure images obtained from ground-based telescopes are examined in this dissertation.

15. SUBJECT TERMS

Detection, Space Situational Awareness, Telescope, Optics, Space Object Detection

16. SECURITY CLASSIFICATION OF:			17. LIMITATION OF ABSTRACT	18. NUMBER OF PAGES	19a. NAME OF RESPONSIBLE PERSON
a. REPORT	b. ABSTRACT	c. THIS PAGE			Dr. Stephen C. Cain, AFIT/ENG
U	U	U	UU	127	19b. TELEPHONE NUMBER *(Include area code)* (937) 255-3636 x4716 stephen.cain@afit.edu